Samarium Hexaboride: The First True 3D Topological Insulator?

by

Steven G. Wolgast

A dissertation submitted in partial fulfillment
of the requirements for the degree of
Doctor of Philosophy
(Physics)
in The University of Michigan
2015

Doctoral Committee:

Professor Çağlıyan Kurdak, Chair
Emeritus Professor James W. Allen
Professor Roy Clarke
Assistant Professor Lu Li
Associate Professor Vanessa Sih
Assistant Professor Kai Sun
Associate Professor Zhaohui Zhong

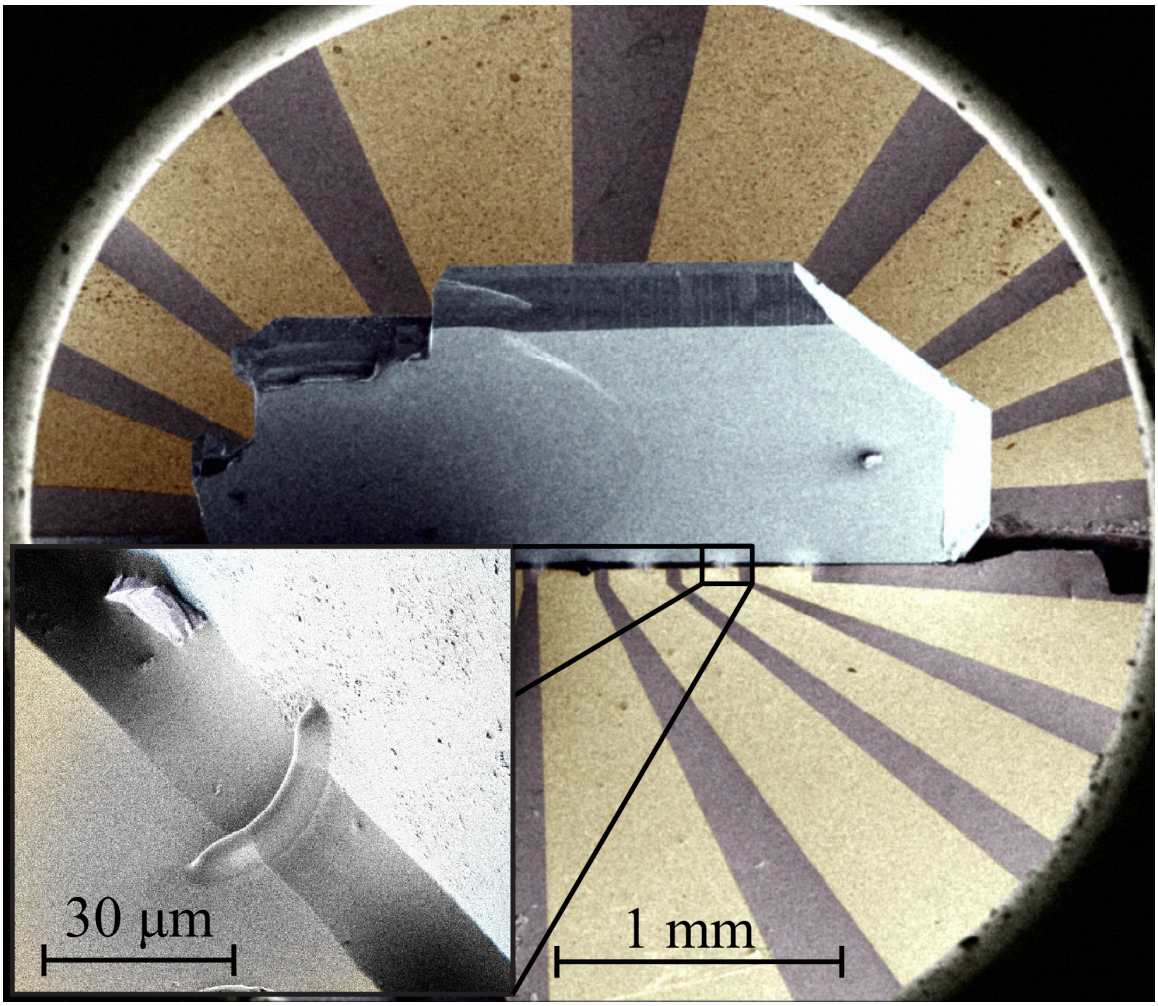

SmB_6 crystal sandwiched between two sets of gold contact pads and connected with ion-beam-deposited platinum contacts.

To my parents, whose loving sacrifice, generous support, and constant encouragement have made this dissertation possible.

ACKNOWLEDGEMENTS

Thanks to the people who made this dissertation possible, especially Yun Suk Eo, who contributed equally to the preparation and magnetoresistance study of the SmB_6 samples, including polishing, mask design, lithography, wirebonding, running the cryostats, performing resistance measurements and data analysis, and researching theory relevant to weak anti-localization and spin-glass systems; and Çağlıyan Kurdak, who conceived, guided, and supported the work contained herein. Thanks are also due to Zachary Fisk and Dae-Jeong Kim (University of California, Irvine) for supplying the SmB_6 crystals; Jim Allen and Kai Sun for their invaluable insights on the experimental and theoretical details of this system, as well as their advice on interaction with the larger scientific community; Kai Sun for performing the finite-element analysis simulations and band-closure calculations; Ilya Vugmeyster for polishing assistance; Roberto Merlin for furnishing polishing equipment; Teoman Öztürk and Juniar Lucien for their contributions to sample preparation; Kyunghoon Lee for his wirebonding assistance; Richard Field III for his proofreading expertise and photographic service; Lu Li, Gang Li, and the rest of the Li research group for their transport measurements at the National High Magnetic Field Laboratory; Gang Li and Fan Yu for their help with optical imaging; Fedor Balakirev and Marcelo Jaime for their patience and expertise on the pulsed magnet systems; Piers Coleman for his input on hybridization and band-closure physics; Jan Jaroszynski for helpful discussion of the magnetocaloric effect; Leonard Sander for his insight on crack formation; Jason Cooley for sample preparation advice; Emanuel Gull for discussions on numer-

ical techniques; Pilar Herrera-Fierro for polishing and microscopic imaging advice; Alexa Rakoski, Jim Allen, Chris Wolgast, and Amanda Wolgast for help proofreading the thesis; Benjamin Wolgast for his cooperation during the preparation of this thesis; and Amanda Wolgast for her unrelenting support and encouragement, and for making the time for the thesis work possible.

Funding for this project was provided by the National Science Foundation (NSF) grants #ECCS-1307744, #DMR-1006500, #DMR-1441965, and #DMR-0801253, and the Department of Energy (DOE) award #DE-SC0008110. The work done at the Electron Microbeam Analysis Laboratory (EMAL) on the Focused Ion Beam was supported in part by NSF grant #DMR-0320740. The work done at EMAL on the Philips XL30 FEG was supported in part by funds from an AFSOR MURI headed by Ron Gibala (DOD-G-F49620-93-1-0289, Center for Advanced Structural Metallic Materials) and from the College of Engineering and the Department of Materials Science and Engineering at the University of Michigan. Device fabrication was performed in part at the Lurie Nanofabrication Facility, a member of the National Nanotechnology Infrastructure Network, which is supported by the NSF. The high-field experiments were performed at the National High Magnetic Field Laboratory, which is supported by NSF Cooperative Agreement #DMR-084173 and #DMR-1157490, by the State of Florida, and by the DOE. Figure 1.1 was generated using POV-Ray™ v. 3.6.

TABLE OF CONTENTS

DEDICATION ii

ACKNOWLEDGEMENTS iii

LIST OF FIGURES vii

LIST OF TABLES x

LIST OF APPENDICES xi

LIST OF ABBREVIATIONS xii

ABSTRACT xiv

CHAPTER

I. Introduction: Samarium Hexaboride 1

1.1 Overview: Samarium Hexaboride 1
1.2 A History of Transport (and Related) Studies 3

II. Introduction: Topological Insulators 12

2.1 Introduction 12
2.2 Experimental Signatures of 3D Topological Insulators 14
2.3 Topological Enhancement Factor 17
2.4 Overview of Some Known Topological Insulators 18
2.5 Topological Kondo Insulators 20

III. Bulk versus Surface Transport Experiment 22

3.1 Introduction 22
3.2 Experiment Design 23
3.3 Sample Fabrication 26
3.3.1 Surface Preparation and Mounting 26

3.3.2 Ion-Beam-Induced Deposition 28
3.4 Experimental Methods and Data 34
3.5 Finite Element Analysis Simulations 34
3.6 Discussion of Experimental Results 38

IV. Magnetoresistance of SmB_6 40

4.1 Introduction 40
4.2 Hall Bars as a Poor Tool for Analyzing Surface Conduction . 41
4.3 Corbino Measurement Geometry 46
4.3.1 Macroscopic Transport Equations 47
4.3.2 Microscopic Transport Equations 49
4.3.3 Multiple Carrier Channels 50
4.3.4 $\vec{B}$-dependent n and μ 52
4.4 Magnetoresistance Below 3 K 53
4.4.1 Experimental Methods 54
4.4.2 Measurements of Magnetoresistance at Large Magnetic Fields 56
4.4.3 Hysteretic Magnetotransport at Small Magnetic Fields 61
4.4.4 Discussion 66
4.4.5 Summary and Outlook 76
4.5 Bandgap Closure at High Magnetic Fields 77
4.5.1 Introduction 77
4.5.2 Experimental Methods 78
4.5.3 Discussion 80
4.5.4 Summary and Outlook 86

V. SmB_6 Surface Morphology 87

5.1 Introduction 87
5.2 Scratch Experiment 89
5.3 Implications of Subsurface Cracks 92

VI. Summary and Outlook 95

6.1 Introduction 95
6.2 Summary of the Thesis Work 95
6.3 Summary of other work on SmB_6 98
6.4 Current Issues 99
6.5 Future Transport Studies 104

APPENDICES 107

BIBLIOGRAPHY 140

LIST OF FIGURES

Figure

1.1 SmB_6 unit cell. 2

2.1 Magnetic field dependence of the Topological Enhancement Factor for different scattering ranges. 18

3.1 Schematic diagram of experiment configuration. 24

3.2 Cross sections of bulk slabs for three measurement geometries. . . . 27

3.3 Diagram of sample assembly. 29

3.4 Diagram of typical IBID operation. 30

3.5 Orientation of ion beam and electron beam relative to the sample during IBID. 31

3.6 E-beam images of platinum contacts. 32

3.7 Raster patterns for IBID. 33

3.8 Four-terminal resistances plotted as a function of temperature. . . . 35

3.9 Simulated resistance curves from the FEA for each configuration. . . 37

4.1 SmB_6 sample configured in van der Pauw-like geometry. 41

4.2 Hall data from the Hall bar sample. 43

4.3 Comparison of SmB_6 conductivities with conventional 2D electron gas structures. 44

4.4 Corbino geometry diagram 48

4.5 Corbino disk images. 55

4.6 Magnetoresistance traces at several angles for the (011) and (001) surfaces. 57

4.7 Plot of the (011) surface carrier density and mobility obtained from angle-dependent fits. 59

4.8 Response of the resistivity of the Corbino disk samples to the magnetic field below 6 T at 0.3 K for different sweep rates. 62

4.9 Response of the resistivity of the Corbino disk samples to the magnetic field below 1 T at 80 mK for different sweep rates. 63

4.10 Magnitude of the dips (in conductivity) as a function of temperature at a magnetic field sweep rate of 0.167 mT/s. 63

4.11 Magnitude of the dips (in conductivity) as a function of the magnetic field sweep rate at 80 mK. 64

4.12 Resistivity of the Corbino disk samples at 0.3 K versus magnetic field perpendicular and parallel to the transport surface. 64

4.13 Resistivity versus temperature for the (011) and (001) surfaces. . . . 68

4.14 Fitted mobility alongside several mobility projections of the Kondo effect for various T_{K}. 70

4.15 Magnetoresistance at 4 K for several magnetic pulse amplitudes. . . 80

4.16 Magnetoresistance at 1.4 K for two 100 T magnet pulses. 81

4.17 Magnetoresistance across the crossover temperature range. 83

4.18 Plots of the Corbino disk two-terminal resistance versus temperature for select values of the magnetic field. 84

4.19 Calculated transport activation energy as a function of magnetic field. 85

5.1 Scratched Corbino disk measurements. 90

5.2 Ion-milled cross sections of scratches. 93

A.1 Cosine fits of angle-dependent magnetoresistance data at magnetic fields of 5, 12, and 25 T, respectively, for the (001) surface and the (011) surface. . . . 109

A.2 (001) surface carrier density and mobility obtained from angle-dependent fits of the data. . . . 109

B.1 Simulated magnetoresistance of the (011) surface due to Kondo scattering alone, based on the values obtained from the logarithmic temperature dependence. . . . 112

C.1 Schematic diagram of the circuit used to measure resistance during the high-field magnetic pulses. . . . 114

C.2 Schematic diagram of the effective circuit used to model the influence of the signal cable impedance. . . . 114

E.1 CS4-10V Sweeper Program user interface. . . . 125

E.2 Sweeper Program back panel 126

E.3 Sweeper Program flowchart 1 128

E.4 Sweeper Program flowchart 2 129

E.5 Initialization routines 130

E.6 Coercion warning for minimum range 131

E.7 Coercion warning for Limit Tolerance 131

E.8 Instrument setup routine 133

E.9 Main program loop (left side) 134

E.10 Case machine cases 135

E.11 Main program loop (right side) 137

E.12 Program-closing routine 138

E.13 Check Stop Button routine 139

LIST OF TABLES

Table

2.1 List of some known topological insulators. 13

3.1 List of contacts used for each measurement configuration. 34

4.1 List of reported surface transport parameters. 67

D.1 List of fitting parameters for $n(B)$. 119

LIST OF APPENDICES

Appendix

A. Analysis of the (001) Surface Conductivity 108

B. Kondo Scattering as the Origin of the Magnetoresistance 111

C. Pulsed-Field Measurement Details 113

D. Carrier Density Fitting Source Code 118

E. CS4-10V Magnet Sweeper Program 124

LIST OF ABBREVIATIONS

2D two-dimensional

2DEG two-dimensional electron gas

3D three-dimensional

AC alternating current

Al_2O_3 aluminum oxide

ARPES Angle-Resolved Photoemission Spectroscopy

BZ Brillouin zone

DC direct current

dHvA de Haas–van Alphen

FEA Finite Element Analysis

FIB Focused Ion Beam

HAXPES Hard X-ray Photoelectron Spectroscopy

HCl hydrochloric acid

HNO_3 nitric acid

IBID Ion Beam-Induced Deposition

MR magnetoresistance

NHMFL National High Magnetic Field Laboratory

NMR nuclear magnetic resonance

PES Photoemission Spectroscopy

RKKY Ruderman-Kittel-Kasuya-Yosida

RRR residual resistivity ratio

SARPES Spin-resolved ARPES

SdH Shubnikov–de Haas

SEM Scanning Electron Microscope

SiC silicon carbide

Sm_2O_3 samarium oxide

SmB_6 samarium hexaboride

STS Scanning Tunneling Spectroscopy

TEF Topological Enhancement Factor

TI topological insulator

TKI topological Kondo insulator

WAL weak anti-localization

WL weak localization

UHRPES Ultra-high Resolution Photoemission Spectroscopy

ABSTRACT

Samarium Hexaboride: The First True 3D Topological Insulator?

by

Steven G. Wolgast

Chair: Çağlıyan Kurdak

The recent theoretical prediction of a topologically protected surface state in the mixed-valent insulator SmB_6 has motivated a series of charge transport studies, which are presented here. It is first studied using a specialized configuration designed to distinguish bulk-dominated conduction from surface-dominated conduction. As the material is cooled below 4 K, it exhibits a crossover from thermally activated bulk transport to metallic surface conduction with a fully insulating bulk. The robustness and magnitude of the surface conductivity, as is manifest in the literature of SmB_6, is strong evidence for the topological insulator (TI) metallic surface states predicted for this material. This resolves a decades-old puzzle surrounding the low-temperature behavior of SmB_6. Next, the magnetotransport properties of the surface are investigated using a Corbino disk geometry, which can directly measure the conductivity of individual surfaces. Both (011) and (001) crystal surfaces show a strong negative magnetoresistance at all magnetic field angles, due primarily to changes in the carrier density. The low mobility value accounts for the failure so far to observe Shubnikov–de Haas oscillations below 95 T. Small variations in the mobility and temperature dependence suggest a suppression of Kondo scattering from native

oxide-layer magnetic moments. At low fields, a dynamical field-sweep-rate-dependent hysteretic behavior is observed. It persists at the slowest sweep rates, and cannot be explained by quantum interference corrections; it is more likely due to extrinsic effects such as the magnetocaloric effect or glassy ordering of the native oxide moments. Pulsed magnetic field measurements up to 60 T at temperatures throughout the crossover regime clearly distinguish the surface magnetoresistance from the bulk magnetoresistance. The bulk magnetoresistance is due to a reduction in the bulk gap with increasing magnetic field. Finally, small subsurface cracks formed in SmB_6 via systematic scratching or sanding results in a counter-intuitive increase in the electrical conduction due to the unique surface-conducting property of TIs, strengthening the building case for SmB_6's topological nature. This material is attractive as a TI because its bulk is fully insulating at a readily achieved 2 K, but it presents a large number of scientific mysteries and experimental challenges for future research.

CHAPTER I

Introduction: Samarium Hexaboride

1.1 Overview: Samarium Hexaboride

Samarium hexaboride (SmB_6) is a rare-earth material that serves as an archetype mixed-valent compound. Its crystal structure is simple cubic (space group $Pm3m$ (O_h^1)) with a lattice parameter of 4.133 Å (at 23 K) [1], in which an octahedral B cage sits at the center of the unit cell, while a Sm ion sits at the corner of the unit cell (Figure 1.1). It is typically manufactured via zone refining by means of sintering or arc melting. Historically, this has been accomplished most successfully in an Al flux, but there have been recent efforts to produce Al-free samples using floating-zone refining techniques. (Direct reactions of samarium oxide (Sm_2O_3) and B produced crystals of poor quality [2].) Flux-grown single crystal pieces are dark blue and tend to be oblong along the zone-growth direction, up to a few millimeters in length. The samples considered in the present study were produced in an Al flux, and often contain Al inclusions, particularly extended along the growth direction. The samples exhibit clear growth planes in the (001) and (011) directions. Single crystals of SmB_6 have a hardness on the order of 1300 kg/mm^2 [3], largely due to the mechanical rigidity of the B cages. SmB_6 does not readily cleave along any particular crystal plane.

SmB_6 is one member of a series of rare-earth hexaborides (*e. g.*, LaB_6, YbB_6, CeB_6, NbB_6, *etc.*), so many studies compare the mechanical properties and electronic

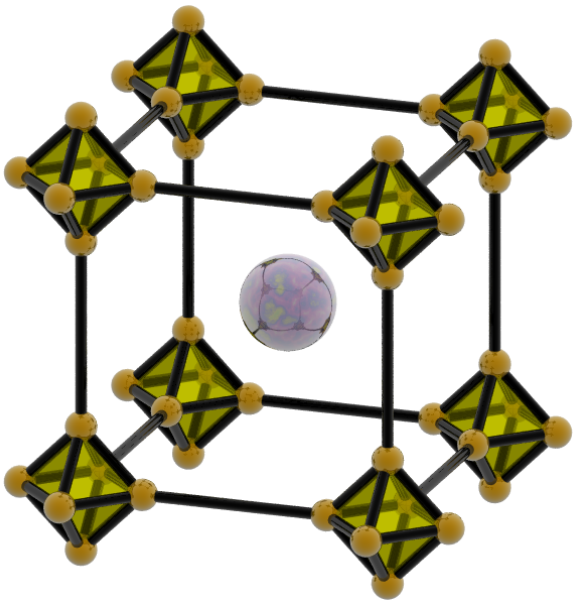

Figure 1.1: The SmB_6 unit cell, with octahedral B cages in the corners and a Sm ion in the center.

structures of these materials. However, only SmB_6 has a mixed-valence character [4–6], due to the value of the lowest $4f$ ionization energy lying above the bottom edge of its conduction band ($5d$). Indeed, these seem to be the basic necessary ingredients for a homogeneous mixed-valent system [7], which is characterized not by an average mixture of integer-valence ions in a crystalline or disordered configuration, but rather by a truly intermediate valence for each ion. This requires that some of the f electrons move to the conduction band, leaving the f states partially ionized (Sm^{3+}). The ground state might then be a mixture of $4f^5$ and $4f^6$ electron states that hybridize with the $5d$ conduction states. Other examples of mixed-valent systems which have been useful for comparisons to SmB_6 include $CePd_3$, TmSe, the α phase of Ce, and the "gold" phase of SmS [8]. EuB_6 also has a 2+ ionic configuration determined by Hund's rules, but it is not mixed-valent, since the lowest f ionization energy is more than 1 eV below the conduction band. However, the loosely bound $4f$ electron in Ce and $4f$ hole in Yb have energies close to the $5d$ conduction states, so compounds of these rare-earth elements can, by this criterion, be mixed-valent.

1.2 A History of Transport (and Related) Studies

SmB_6 has a rich history of rigorous study and scientific debate, due primarily to its behavior as a mixed-valent material and its unusual transport characteristics. One of the biggest debates revolved around the fundamental nature of the zero-temperature ground state: Is the material a metal or an insulator? This question was first addressed by transport studies in the early 1970's, but theoretical models to explain the data were very slow to arrive due to the complications arising from strong correlation effects.

The first systematic transport study of SmB_6 was conducted in 1969 by Menth, Buehler, and Geballe [2]. They reported a transition from metallic behavior at room temperature to semiconducting behavior at cryogenic temperatures. This is supported in their observation of an exponential increase in resistivity as the temperature is lowered, which is consistent with a model of thermally activated transport. Such a behavior has a temperature dependence of

$$\rho = \rho_0 e^{\frac{\Delta}{k_B T}}, \tag{1.1}$$

where ρ is the resistivity, Δ is the transport bandgap, k_B is the Boltzmann constant, and T is the temperature. This behavior in SmB_6 allowed the researchers to posit the existence of a bulk electron gap with energy 2.3 meV at low temperatures [2].

The second key measurement in their work was the magnetic susceptibility of SmB_6, which shows no evidence for magnetic ordering down to 0.35 K. This makes SmB_6 unique among the rare-earth hexaborides, and suggests that the Sm ions are divalent with zero net magnetic moment. Menth *et al.* incorporated these experimental ideas together in the following way. As the temperature is raised from absolute zero, some of the Sm^{2+} ions are thermally ionized from their $4f^6$ environment to Sm^{3+}. There is a corresponding increase in both the carrier density and the magnetic

susceptibility, leading to an eventual crossover to metallic behavior at higher temperatures. In this case, one would expect to see a gradual shift in valence from Sm^{2+} to Sm^{3+} as the temperature is raised.

The third key observation was that the very-low-temperature data for the resistivity (<3 K) and magnetic susceptibility (<10 K) did not agree with the semiconductor model. Instead, the researchers observed a plateau in the resistivity and inverse magnetic susceptibility at the lowest temperatures. At the time, these plateaus were dismissed as resulting from conductive in-gap states arising from rare-earth impurities in the crystal; the data is even omitted from the published graphs, being mentioned only in the text. Subsequent studies also observed the plateau [9–11]. However, a surprise came a year later from Mössbauer spectroscopy [4, 5], which indicated that the Sm valence was relatively flat over a large temperature range, in contrast to the expectation from Menth *et al.*'s model of shifting valence. The general consensus among researchers in the field over the next decade was that the plateau was a metallic feature. (Nickerson *et al.* proposed a narrow in-gap band based on their Hall resistivity data [9], but Kasuya points out that their 3-band model is erroneous due to the omission of the anomalous Hall effect and the width of the $5d$ band [12].) Of course, the resistivity rise itself must be explained. The possibility that the plateau was a manifestation of a metallic mixed-valent ground state was suggested by some [13]; in such a picture, intense f–d scattering could result in an increase in the resistivity, in analogy with the Kondo effect. Indeed, the mechanism responsible for the resistivity rise and plateau became a primary focus for subsequent researchers, and is the main experimental motivation for the current work.

Theoretical models capable of explaining the experimental data in SmB_6 and other mixed-valent materials were difficult to produce because there was no good way to treat strong-correlation effects from the f electrons. The earliest attempts [7, 14, 15] posit a model in which an itinerant d band overlaps with the smallest f

ionization energy with a tiny dispersion. Specifically for rare-earth compounds, if the $5d$ band and $4f$ states hybridize with an interaction strength of Δ, one would expect a dramatic peak in the density of states at the energy of the $4f$ states with a width of Δ, and the Fermi energy $E_{\rm F}$ would reside in this peak. Since some of the electrons in the $4f$ states move to partially fill the $5d$ band, this scenario naturally leads to the mixed-valent behavior of the material indicated by Mössbauer spectroscopy [4–6]. Indeed, this was the prevailing explanation for the pressure-induced transition in SmS from the insulating "black" phase to the metallic "gold" phase. In the black phase, the $4f$ ionization energies are below the $5d$ band, and $E_{\rm F}$ lies between them at 0 K. As pressure is applied, the $4f$ ionization energy shifts up into the conduction band, resulting in partial filling of the $5d$ states and metallic behavior from the material. In the mid-1970s, the prevailing notion was that the band structure of SmB_6 was analogous to the gold phase of SmS.

In 1979, a study of the resistivity and the Hall effect was performed by Allen, Batlogg, and Wachter, in which the metallic interpretation of the plateau was challenged [16]. These authors measured the resistivity of single-crystal samples with a residual resistivity ratio (RRR) of 10^4, larger than previously seen and large enough to suggest to them the possibility that the resistivity rise could be signaling a gap. One motivation for the gap scenario was their realization that the resistivity rise observed at low temperatures in their samples was simply too large for scattering, with a number of carriers equal to that implied by the valence. Specifically, the resistivity exceeded, by roughly a factor of 10^4, the so-called "unitarity limit" [17], given by having a scatterer in every unit cell, scattering with the maximum possible phase shift of $\pi/2$ per channel. However, previously published Hall effect data [9] showed a complex low-T behavior quite inconsistent with the freezing-out of carriers expected for a gap. Noticing that these earlier Hall effect data were for samples with a very small RRR, Allen *et al.* measured the Hall effect for their samples and found a much different

result, that the large 10^4 resistivity rise was accompanied by a similar 10^4 increase in the magnitude of the (negative) Hall coefficient $R_{\rm H}$, which saturated only at low T when the resistivity also saturated. This was interpreted as clear evidence for a gap intrinsic to the material. The plateau in resistivity and $R_{\rm H}$ was then ascribed to extrinsic impurity states in the gap, and previous studies [12] showing a systematic correlation between larger RRR and more nearly perfect sample stoichiometry for $Sm_{1-x}V_xB_6$ (V = vacancy) were cited as evidence supporting this interpretation. The Sm vacancy data were also cited as evidence against a model [18] of hopping conduction in Fermi energy states that are Anderson-localized by disorder, on the grounds that the low-T conductivity increases rather than decreases with increased numbers of vacancies, *i. e.*, more disorder.

Allen *et al.*'s Hall data reveals that the resistivity rise is dominated by changes in the carrier density, rather than the changes in the mobility expected for an increase in scattering due to a Kondo-like mechanism in a metallic system. Further, the carrier densities obtained were consistent with small-gap semiconductor behavior at low T, but bad metallic behavior at higher T where $k_{\rm B}T$ is an order of magnitude larger than the bandgap. These facts taken together provide unambiguous evidence for an intrinsic gap. This conclusion was corroborated by optical data [19], which shows a clear bandgap of around 4 meV at 4 K, and by point-contact spectroscopy [20, 21], which reveals a similar bandgap.

From a theory perspective, the picture of band hybridization can be consistent with a gapped (semiconducting) band structure; if the $4f$ states are degenerate with the right symmetries, then wavefunction interactions should open a small hybridization gap at $E_{\rm F}$ of a few meV, resulting in a mixed-valent insulator. Anderson argued [22] that the $5d$ band could only hybridize with one of the degenerate $4f$ states, leaving $E_{\rm F}$ ungapped by the remaining $4f$ states. However, Mott replied [23] that the strong correlations among the degenerate $4f$ states would allow a small hybridization

gap of order Δ to form. In 1979 [24] and in a later paper in 1981 [25], Martin and Allen showed how to make the hybridization-gap picture realistic for SmB_6. They constructed the low-lying $4f$ fermion excitations from electron removal transitions between the lowest-lying f^6 multiplet ($^7F_0$) and the lowest-lying f^5 multiplet ($^6H_{5/2}$). In cubic symmetry at the Γ point in the Brillouin zone (BZ), the 5/2 state is crystal-field split into a doublet and a quartet. Taking the doublet to have the lowest energy (*i. e.*, to be nearest E_F), they showed that it would have the correct symmetry to hybridize with the conduction band at all places in the BZ where parity is not a good quantum number. Taken together with the effect of the deeper-lying B p band repelling the f excitation at the X point (where parity is a good quantum number), this leads to a fully gapped band structure across the entire BZ. Because the number of conduction electrons is equal to the f^5 fraction, E_F must lie in this gap. (In 1992, a similar bandgap formation mechanism was introduced by G. Aeppli and Z. Fisk [26] for mixed-valence systems near enough to integer valence to be in the Kondo regime. In some such systems, hybridization between the conduction band and the renormalized $4f$ excitations associated with the Kondo resonance can result in a narrow bandgap at E_F. Such materials, called *Kondo insulators*, can be metallic at high temperatures and then open a small "Kondo gap" at low temperatures. In fact, there is a smooth progression between this Kondo gap situation and that of the mixed-valence gap situation, and the term Kondo insulator is often applied to all such materials. Indeed, there is evidence that the gap in SmB_6 is temperature-dependent [27–29].)

Of course, as discussed already, the experimental evidence for a tiny bandgap leaves the resistivity plateau as something of a mystery. Allen *et al.* [16] had suggested that in the gap scenario, the plateau might be due to Sm vacancies or similar defects causing E_F to lie in an impurity band inside the gap. Band tails that stretch into the gap could be another such possibility. However, Allen *et al.* [16] also noted

that even in the impurity-band scenario, the minimum theoretical conductivity, based on the Mott impurity-band criterion [30] is still 15 times larger than what is experimentally observed, so this explanation was still not really satisfactory. Other, more exotic explanations arose during the time, notably Kasuya *et al.*'s idea [31] that the conductivity arises from the phase slippage of a Wigner lattice. A perfect lattice should have an infinite conductivity at 0 K, but disorder would pin the lattice to the observed finite conductivities.

In 1995, a paper was published by J. C. Cooley *et al.* [32], which described their pressure-dependent transport study. As the pressure is increased, the rise in resistivity is reduced, along with the value of the plateau. Analysis of this decrease, based on a model of thermally activated carriers, showed that the bandgap shrinks smoothly under pressure until a critical pressure around 50 kbar, where it suddenly collapses—evidence against a simple hybridization-gap model, for which the gap would close continuously. Meanwhile, R_{H}, including the plateau, shrinks under pressure. The carrier densities extracted from these measurements below 4 K change by $\sim$4 orders of magnitude with pressure before the gap collapses at 50 kbar. Meanwhile, the absolute value of the ambient-pressure resistivity exceeds the unitarity scattering limit by a factor of 80, assuming the ambient-pressure extracted carrier density. Cooley *et al.* took this as evidence against an impurity band, and together with the absence of a metal–insulator transition, suggested that the plateau is due to intrinsic in-gap states, present even in pristine SmB_6. Nonetheless, they acknowledged that these intrinsic states would then have to have the property of exhibiting "superunitarity" scattering.

An important realization was made the following year by these same researchers, in collaboration with others, when they observed that chemical etching of the samples between 10 – 30% could dramatically alter the RRR of the samples [33]. This led them to hypothesize that the resistivity plateau was an extrinsic surface effect due to a "dirty metal" on the surface. Indeed, the T dependence of the resistivity was easily

fit using a parallel-resistance model with one constant resistance (corresponding to the surface channel) and one activated-transport resistance (corresponding to a semiconducting bulk channel). Their report stressed in rather brusque terms that many earlier sets of data would need to be repeated on samples with better stoichiometry and on chemically etched surfaces. However, etching did not completely remove the plateau, and they concluded that "the surface crud is not a discrete layer but rather is continuously changing spatially." This suggests that in order to measure the cleanest, most pristine samples and to maximize the RRR, one would have to completely etch away the entire sample! Despite the self-inconsistency in their report, these researchers did make an important connection between the plateau and SmB_6 surface effects, which introduces a new mystery: How can a layer of "crud" survive etching and all other kinds of surface treatment in all experiments to date?

This puzzle persisted for nearly 15 more years without a satisfactory explanation. In one notable transport study [34] from 2001, Flachbart *et al.* summarized their findings by maintaining that the plateau is intrinsic to the bulk, evading the violation of the unitarity scattering limit likely through strong many-particle interactions, but with an additional contribution from surface states arising from a shift in Sm valence from the mixed bulk value towards Sm^{3+} on the surface. The overall picture is then a low-T hybridization gap ($\sim$11 meV) in which resides a thermally activated bulk band $\sim$3 meV below the conduction band edge. Below this band, the authors posited an additional narrow-band bulk contribution from Mott impurity conduction [30] in samples with more imperfections, *e. g.*, the presence of multiple B isotopes. On top of this, there is demonstrably a contribution to the conduction from metallic surface states at low temperatures.

The picture of a hybridization gap with a donor-like in-gap state just below the conduction band was also supported by spectroscopy done during this time period. Gorshunov *et al.* [35] pointed out that a number of earlier works report gaps that

fall into two ranges, 3 – 5 meV and 10 – 15 meV. They combined this evidence with their own electrical spectroscopy measurements, presenting a unified picture with a bandgap of 19 meV and a narrow in-gap state 3 meV below the conduction band, the latter of which determines the activation energy of direct current (DC) transport measurements in the 3 – 15 K range. In that work, they interpreted the plateau as hopping among the localized in-gap states.

Meanwhile, advances in Angle-Resolved Photoemission Spectroscopy (ARPES) permitted a more detailed study of the band structure of SmB_6. For example, a study in 2000 by Denlinger *et al.* [36] shows a detailed picture of the $5d$ band dispersing across the localized $4f$ states. This study also gives a more detailed picture regarding the presence of the $4f^6 \rightarrow 4f^5$ multiplet transition, and shows a broad $5d$ band all the way up to E_F, suggesting strong scattering with the f states. Unfortunately, the energy resolution available to these researchers (see also Mo *et al.* [37]) was not sufficient to discern the details of the tiny gap, particularly the nature of the low-T conductivity. Ultra-high Resolution Photoemission Spectroscopy (UHRPES) provided the necessary resolution, but largely without the k dependence of ARPES. Such studies [38, 39] could observe an in-gap state around 3 meV below the conduction band, but its origin still eluded a consistent explanation.

SmB_6 has a rich, complex behavior, as attested by the huge experimental effort expended on it, as well as strong theoretical debates over some of its most fundamental properties. It had taken 10 years to experimentally establish a community consensus regarding the *existence* of a bandgap, let alone the mechanism responsible for its formation. Even more notably, after 40 years of work, one of the earliest-known features still eluded understanding. The resistivity plateau below 3 K, which was attributed to a plethora of mechanisms including doping or vacancy impurity conduction, metallic bands, band-tail conduction, Mott impurity conduction, Wigner-lattice phase slippage, surface "crud," isotope impurities, and hopping mechanisms, could still not

be explained in a holistic manner with other features of the electronic structure. In Chapter II, the exciting new field of topological insulators is discussed, which provides a way to resolve this long-standing puzzle.

CHAPTER II

Introduction: Topological Insulators

2.1 Introduction

One of the most exciting developments in condensed matter in the last decade has been the topological theory of band insulators. Born out of a theoretical treatment of quantum Hall systems, this new theory predicts the existence of insulators with non-trivial band topology, known as topological insulators (TIs). Although the details of the band topology and the ingredients necessary to obtain a non-trivial topology are interesting in their own right, the most striking feature of TIs is the existence of a topologically protected edge or surface state for 2D and 3D TIs, respectively. The edge (surface) state is robust against perturbations because it arises fundamentally from the bulk band topology, rather than from the detailed edge (surface) chemistry of the TI. This edge (surface) state is manifest as half a Dirac fermion; *i. e.*, its k-space representation resembles a Dirac-like conical dispersion, much like graphene, but it has no spin (Kramers) degeneracy except at the high-symmetry points of k space (Kramers doublets). Correspondingly, the edge (surface) state is spin–momentum locked, usually due to a strong spin–orbit coupling mechanism. Thus, the edge (surface) currents in TIs are naturally spin-polarized with respect to the direction of current flow. This has all sorts of remarkable applications, particularly for the field of spintronics, which relies on spin-polarized currents for device operation. 3D TIs

Type	Material	Bulk Transport
2D	CdTe/HgTe/CdTe	insulating
3D	$Bi_{1-x}Sb_x$	weakly insulating
3D	Sb	metallic
3D	Bi_2Se_3	metallic
3D	Bi_2Te_3	metallic
3D	Sb_2Te_3	metallic
3D	Bi_2Te_2Se	moderately insulating
3D	$Bi_{2-x}Sb_xTe_{3-y}Se_y$	reasonably insulating
3D	SmB_6	fully insulating

Table 2.1: List of some known topological insulators, taken from Reference [52].

hold the additional promise of realizing Majorana fermions [40, 41], which have applications to quantum computing.

Quite remarkably, TI theory preceded experimental efforts, whereas theories typically follow experimental efforts in an attempt to explain the phenomena observed. In contrast, the first topology-based theory for time-reversal-invariant 2D TIs [42–44] was published in 2005, but the experimental realization of a 2D TI [45] in HgTe was not achieved until 2007. Similarly, the extension of the theory to 3D systems was done in 2006 [46–48], but the first 3D TI observed by ARPES, $Bi_{1-x}Sb_x$, was confirmed in 2008 [49], followed by the observation of the spin-polarized surface in 2009 [50, 51]. Since then, a short list of 2D and 3D TIs has been developed (See Table 2.1 for a representative list from Ando's review [52]). Unfortunately, most of the known 3D TIs are not strictly insulating, as they tend to be semi-metallic and/or suffer from bulk impurity conduction. Strategies to evade these problems have included gating or doping to move E_{F} into the bandgap, improved crystal quality to reduce impurities, and growth of ultra-thin films to minimize the contribution from the bulk conductivity. Nevertheless, bulk conductivity still remains a problem for all transport applications.

2.2 Experimental Signatures of 3D Topological Insulators

From an experimental perspective, perhaps the most obvious and convincing evidence for a non-trivial band topology is the observation of the Dirac-like surface states in ARPES measurements. For example, the first experimental confirmation of the topological surface state was observed in ARPES measurements of $Bi_{0.9}Sb_{0.1}$ [49]. In this study, an odd number (5) of 2D surface bands cross the Fermi energy in the BZ cut from the Γ point to the M point, and the Kramers degeneracy is clearly seen at the M point. Although the surface bands look quite different from the conical Dirac dispersion, the odd number of states and the Dirac point seen at M are sufficient indicators for the topological state.

ARPES can also be used to probe the spin structure of the surface bands when used with a spin-sensitive detector such as a Mott spin detector. Indeed, Spin-resolved ARPES (SARPES) was first performed on $Bi_{1-x}Sb_x$ ($x = 0.09$ [53] and $x = 0.12$ – 0.13 [54]) to confirm the spin–momentum locking characteristic of topological surface states. In this type of study, the SARPES spectra for each spin direction differ from each other slightly, permitting the identification of a surface band with a particular spin orientation. These measurements directly demonstrated the helical spin structure of the surface dispersion.

Transport measurements are also a powerful tool for elucidating the nature of topological surface states, and may be necessary in TI candidate materials for which ARPES does not work as well (*e. g.*, failure of the material to cleave, or small bandgaps). There are several types of experiments that can be done in this spirit and a number of experimental signatures that should be present.

- **Resistivity versus temperature** – From a theoretical perspective, a material must be a bulk insulator in order to have a well-defined band topology. Partially filled (metallic) bands do not have a well-defined Chern number and are, by

definition, not topological *insulators*. If the system in question is truly gapped, it will exhibit its insulating behavior as a diverging resistivity as the temperature is lowered. The Hall coefficient should behave in a similar manner.

- **Surface transport** – For a material to be a TI, it must exhibit metallic surface states. These can be distinguished from the bulk by using geometry-dependent experiments (*e. g.*, varying slab thickness) and angle-dependent magnetoresistance (MR) measurements. They may also be indicated by the presence of Shubnikov–de Haas (SdH) oscillations, which depend on the magnetic field perpendicular to the 2D state.

- **Shubnikov–de Haas oscillations** – Because the topological surface states are 2D, they should exhibit quantum oscillations when a magnetic field is applied. The maxima and minima of the oscillations can be used to elucidate the Berry phase of the surface, which should be π if the surface electrons are Dirac fermions. This is a critical assessment for determining the topology of a material for which spectroscopic techniques are not capable of resolving the topological features.

- **Weak anti-localization** – Normally, an electron interferes constructively with itself over a closed path and over the corresponding time-reversed path, leading to an enhancement in the localization of the electron, known as weak localization (WL). However, because of the accumulated Berry phase of π for the Dirac surface electron, the interference for the TI surface electron is destructive, which leads instead to weak anti-localization (WAL). Thus, any TI surface should exhibit WAL, which can be detected by resistivity measurements as the magnetic field is swept through 0.

The first transport study to give evidence for a 3D TI was again on $Bi_{1-x}Sb_x$ ($x = 0.06$ – 0.09) [50]. These researchers demonstrated a rise in resistivity as the tem-

perature is lowered, especially for $x = 0.09$, corresponding to an insulator. However, the resistivity rise is suppressed below 40 K, indicating the presence of some other conductance channel such as impurity conduction. These researchers also observed SdH oscillations, indicating the presence of the topological 2D transport channels. Correspondingly, they also observed de Haas–van Alphen (dHvA) oscillations in the magnetization of $Bi_{0.91}Sb_{0.09}$. There are two distinct oscillation channels they observed. For one, the amplitude changes with field angle θ as $\sin^{-1}(\theta)$, indicating that it originates from a 2D Fermi surface which corresponds also to the SdH oscillations. For the other channel, the amplitude is finite at all angles, indicating that it originates from a 3D (bulk) Fermi surface. WAL has also been observed [55] on Bi_2Se_3 surfaces as early as 2010.

There are two direct transport-related consequences of the spin–momentum locking on the surface states. One is the suppression of backscattering, since a fully-backwards scattering event must also be a spin-flip event. From a Boltzmann-transport-based perspective, this leads to a 4-fold enhancement in the carrier mobility. Although this cannot be directly probed via resistivity measurements (since one cannot arbitrarily alter the spin structure of a real material), the suppression itself can be seen in Scanning Tunneling Spectroscopy (STS) when examining the quasiparticle interference pattern obtained from Fourier analysis. In fact, the first evidence for the spin helicity in $Bi_{0.92}Sb_{0.08}$ was the suppression of backscattering verified in STS measurements [51] by the absence of the peaks corresponding to backscattering in the quasiparticle interference pattern.

The second direct consequence of spin–momentum locking is the generation of spin current via charge current. This effect is exciting from a device-engineering perspective, since the surface states can be used as a spin injector for spintronic applications. Spin currents have very recently been detected via transport methods in Bi_2Se_3 thin films [56] using metal ferromagnetic tunnel barriers fabricated on the

sample surface. The voltage on the (virtually) floating ferromagnets should depend on the relative orientation of the ferromagnets' magnetization with respect to the average spin orientation of the current. Thus, the researchers were able to confirm the spin–momentum-locking origin of the spin signal by changing the current direction and the ferromagnets' magnetization. Although other effects, *e. g.*, Rashba splitting, can also produce a spin-polarized current, the TI spin-polarization can be distinguished from these by its magnitude and sign [57].

2.3 Topological Enhancement Factor

An external magnetic field can reduce the suppression of backscattering, leading to a decrease in the mobility and to a positive MR [58]. This is due essentially to a skewing of the spin–momentum locking, which can change the scattering rates (momentum relaxation time) determined using a Boltzmann transport model. Specifically, one can define a Topological Enhancement Factor (TEF) as the ratio of the momentum relaxation time including spin effects (τ_{TI}) to the relaxation time excluding them (τ):

$$\mathrm{TEF} \equiv \frac{\tau_{\mathrm{TI}}}{\tau},$$

$$\frac{1}{\tau} = \int W(\mathbf{k},\mathbf{k}')(1-\cos\theta)\mathrm{d}^2\mathbf{k},$$

$$\frac{1}{\tau_{\mathrm{TI}}} = \int W(\mathbf{k},\mathbf{k}')S(\mathbf{s},\mathbf{s}')(1-\cos\theta)\mathrm{d}^2\mathbf{k},$$

where θ is the angle between $\mathbf{k}$ and $\mathbf{k}'$, $W(\mathbf{k},\mathbf{k}')$ is the scattering rate between these two wavevectors, and $S(\mathbf{s},\mathbf{s}')$ is the scattering rate between the two corresponding momentum-locked spins $\mathbf{s}$ and $\mathbf{s}'$. Since the spin contribution is always a value between 0 and 1, the enhanced conductivity will always be greater than or equal to that of the identical system without a spin structure. For a system in which the momentum relaxation time is dominated by a short-range disorder potential, the TEF is 4 at zero

field, and approaches 1 at (very) large out-of-plane fields. For unscreened long-range disorder, the TEF is 2 at zero field, again approaching 1 at (very) large out-of-plane fields. The screened case takes an intermediate value between that of the unscreened case and the short-range scattering case; as screening is turned on, the TEF changes smoothly from that of the unscreened case to that of the fully-screened case (where short-range scattering dominates). These cases are plotted in Figure 2.1. The field scale is determined by $B_{\mathrm{TI}} = \frac{\hbar v_{\mathrm{F}} k_{\mathrm{F}}}{g\mu_{\mathrm{B}}}$, where v_{F} is the Fermi velocity, g is the Landé g-factor, and μ_{B} is the Bohr magneton. In a real system such as Bi_2Se_3 with $v_{\mathrm{F}} = 5 \times 10^5$ ms^{-1} and $k_{\mathrm{F}} \approx 1$ nm^{-1} [59, 60], $B_{\mathrm{TI}} \approx 2840$ T. Thus, in the comparatively small range that is experimentally accessible, the small correction to the TEF is approximately quadratic, leading to a small positive quadratic MR. Although the effect is small for known TIs, it should make a larger contribution to low-carrier-density TIs.

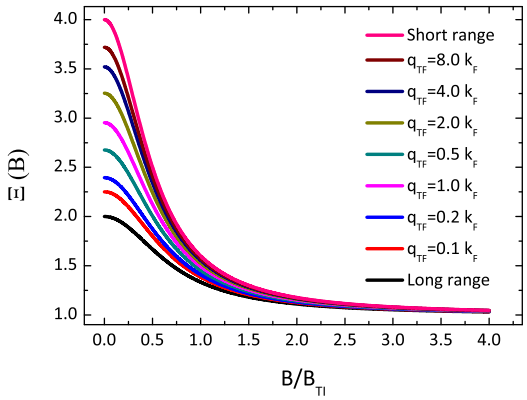

Figure 2.1: Magnetic field dependence of the Topological Enhancement Factor for different scattering ranges.

2.4 Overview of Some Known Topological Insulators

Although $Bi_{1-x}Sb_x$ was the first experimentally-confirmed 3D TI, it proved to be a poor candidate for studying the topological surface states because it also harbors

two pairs of trivial surface band-crossings at E_F that are native to Bi, and which exhibit Rashba splitting. Fu and Kane had also suggested that Bi_2Te_3 might be a TI [61], but the parity calculations necessary to show this were done by Zhang *et al.* [62], who confirmed (theoretically) that the chalcogenides Bi_2Te_3, Bi_2Se_3, and Sb_2Te_3 (but not Sb_2Se_3) should all be TIs. These atomically-layered van der Waals compounds all exhibit a single surface-state Dirac cone at E_F, which greatly simplifies the study of the surface states. These materials also possess the advantage of cleaving easily between quantum layers, and are relatively easy to grow as single crystals.

Bi_2Se_3 was verified to be a TI in 2009 via ARPES by Xia *et al.* [59]. Bi_2Te_3's TI nature was confirmed via ARPES (also in 2009) by Chen *et al.* [63] and Hsieh *et al.* [64]. The k-resolved spectrum of Bi_2Se_3 is especially nice because it exhibits a clean, circular Dirac cone, and the Dirac point lies within the bandgap of the material. In contrast, Bi_2Te_3's spectrum has considerable hexagonal warping due to the spin–orbit coupling, and its Dirac point lies below the top of the valence band, making it difficult to access via transport. Bi_2Se_3 also has a comparatively large bandgap of 0.3 eV, which makes the in-gap surface states accessible at room temperature without activated bulk transport (Bi_2Te_3's bandgap is about 0.17 eV). Unfortunately, both of these materials tend to be degenerately doped by crystalline defects, resulting in a bulk conduction that tends to swamp the surface transport. For example, in transport measurements in a Bi_2Te_3 slab with thickness $\sim$100 µm [65], the surface conduction accounts for an estimated $\sim$0.3% of the total conductance, with the highest bulk conductivity around 10 $m\Omega \cdot cm$.

A more promising TI material was the ternary compound Bi_2Te_2Se, which was first reported in a 2010 ARPES study [66]. Although the bulk of this material has a metallic n-type behavior, a shift of the stoichiometry towards Se-rich samples [67] can result in bulk resistivities beyond 1 $\Omega \cdot cm$; the surface state conduction was about 6% of the total conduction in a 260 µm-thick sample. In fact, further exploration of

this type of compound resulted in the most bulk-insulating 3D TI material known before the present work, the quaternary $Bi_{2-x}Sb_xTe_{3-y}Se_y$ [68, 69]. Specifically, in $Bi_{1.5}Sb_{0.5}Te_{1.7}Se_{1.3}$, for which the bulk resistivity is as large as $\sim$10 $\Omega \cdot$ cm, it has been possible to achieve surface-dominated transport, once the sample thickness has been reduced below $\sim$10 µm. Yet, despite these advances, the bulk conductivity still remains a significant part of the total transport, and a great deal of effort has gone towards the search for fully-insulating TIs for which the surface transport is not polluted by bulk transport channels.

2.5 Topological Kondo Insulators

In 2010, the topological theory of band insulators was extended by Dzero *et al.* to strongly correlated electron systems [70]. Although the strong correlation effects make theoretical treatment of the full electronic structure difficult, the band topology can be deduced from a few simple symmetry and parity arguments one can make regarding the hybridization of f and conduction electrons. These theorists accomplish this by demonstrating that a model Kondo insulator Hamiltonian is adiabatically connected to the tight-binding model, of which the topology is determined by the non-interacting band structure. In contrast to conventional TIs, the topology in these systems arises directly from the spin–orbit coupling associated with the hybridization between conduction and f electrons, making these systems a distinct class of TIs known as topological Kondo insulator (TKI)s. In the simple cubic case discussed in the letter, the nature of the topology is determined by the parity property of the f electrons at the eight high-symmetry points of the BZ, which is itself determined by the relative energy difference between the f level and the conduction band edge. Specifically, the spectrum contains regions which correspond to a strong TI system (the product of all eight parity factors is -1) and regions which correspond to a weak TI system (the product of the four parity factors that correspond to a coplanar

subset of the eight high-symmetry points is -1)[1]; while the former is protected against disorder, the latter is not.

Dzero *et al.*'s paper also contains a brief mention of two candidate TKIs. It speculates that CeNiSn is a weak TKI, while SmB_6 lies near the border between a weak TKI and a strong TKI, based on the valence value of the rare-earth ion in each material. The prediction regarding SmB_6 was further supported by Takimoto's spectrum calculations using an effective quasiparticle Hamiltonian, which can be obtained through Gutzweiler projection or a slave boson approach from a first-principles Hamiltonian [71]. Specifically, SmB_6 was calculated to be a strong TKI, and the in-gap states are identified as the topological surface states. This prediction and the promise of experimentally realizing a new class of TIs are the primary motivations behind the present work.

[1]Basically, the weak TI can be thought of as a stack of 2D TIs. Since there are three equivalent directions (x, y, z) in which the stacking may occur, there are correspondingly three weak topological indices.

CHAPTER III

Bulk versus Surface Transport Experiment

3.1 Introduction

With the prediction [70, 71] that SmB_6 might be a strongly-correlated TI, a new interpretation of the low-temperature resistivity plateau presents itself—that of a topologically protected surface state. Evidence had already been presented [33, 34] that linked the plateau, at least in part, to the surface. The possibility of a topological surface state could account for most of the observations regarding the plateau. First, since it is not a bulk transport mechanism, it evades the necessity for a theory of superunitarity scattering. Second, the topological protection of such a state explains how a surface interpretation of the plateau can be robust against surface treatments such as polishing or etching. Thus, the topological theory provides a nice, if unexpected, way to finally understand what is happening below 3 K in SmB_6.

In order to establish the validity of this hypothesis, it was first necessary to establish unambiguously whether the residual plateau was actually a bulk effect or a surface effect. This chapter describes the experiment that made this determination, the results of which have been published elsewhere [72]. It starts with the conceptual design of the experiment in Section 3.2. In Section 3.3, the fabrication of the experiment sample is described. The results of the experiment are covered in Section 3.4, and Finite Element Analysis (FEA) simulations of the experiment are presented in

Section 3.5. Finally, Section 3.6 contains a discussion of the experimental outcome, its relation to the FEA simulations, and its implications for both historical and future work on SmB_6.

3.2 Experiment Design

To understand the design of the experiment, consider the simple case of a material with an isotropic electrical conductivity. The macroscopic current density $\vec{j}$ can be expressed in terms of the local electric field $\vec{E}$, stated by Ohm's Law:

$$\vec{j} = \sigma \vec{E}, \tag{3.1}$$

where σ is the isotropic conductivity of the material. Suppose an arbitrarily shaped sample of the material has two voltage readout contacts at positions A and B. Because $\nabla \times \vec{E} = 0$ for steady-state conduction, the path integral of $\vec{j}$ from one contact to the other is uniquely given by

$$\int_{\mathrm{A}}^{\mathrm{B}} \vec{j} \cdot \mathrm{d}\vec{s} = \sigma V_{\mathrm{B-A}}, \tag{3.2}$$

where $V_{\mathrm{B-A}}$ is the voltage difference measured at the contacts and does not depend on the path chosen.

Now suppose that an additional two contacts at positions C and D supply a current $I_{\mathrm{C,D}}$ to the sample. If we divide Equation 3.2 by $I_{\mathrm{C,D}}$, we get

$$\int_{\mathrm{A}}^{\mathrm{B}} \frac{\vec{j}}{I_{\mathrm{C,D}}} \cdot \mathrm{d}\vec{s} = \sigma R_{\mathrm{C,D;A,B}}, \tag{3.3}$$

where $R_{\mathrm{C,D;A,B}} \equiv \frac{V_{\mathrm{B-A}}}{I_{\mathrm{C,D}}}$. The integral on the left has units of inverse length, and depends only on the shape of the sample and the location of the four contacts. Thus, for a given sample geometry, we may define this as the geometrical factor $g_{\mathrm{C,D;A,B}}$.

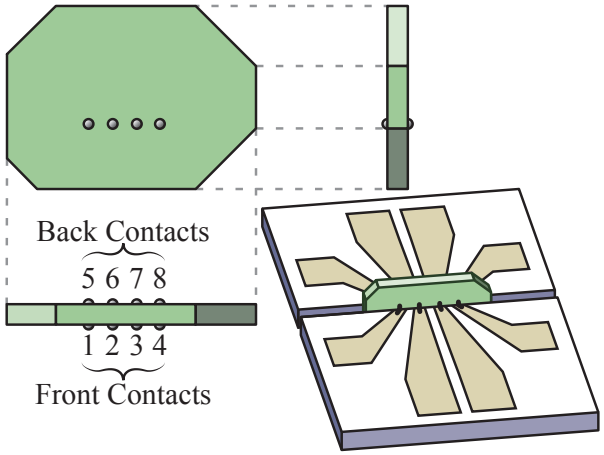

Figure 3.1: Schematic diagram of experiment configuration.

Since σ is isotropic, we may rewrite the expression as

$$R_{\mathrm{C,D;A,B}}(T) = \rho(T) g_{\mathrm{C,D;A,B}}, \tag{3.4}$$

where $\rho(T)$ is the isotropic resistivity of the material. The T dependence of $\rho(T)$ and $R_{\mathrm{C,D;A,B}}(T)$ are explicit here to emphasize the experimental usefulness of this expression; *i. e.*, $\rho(T)$ can be obtained simply by measuring $R_{\mathrm{C,D;A,B}}(T)$ if the geometrical factor is known. In the case for anisotropic σ, the geometrical factor can also have a subtle T dependence if the relative directional components of σ do not change uniformly with temperature, such as during a crystallographic phase transition. The T dependence of $g_{\mathrm{C,D;A,B}}$ can be even stronger if there are multiple transport mechanisms simultaneously present in the material that differ both in T dependence and in the directional dependence of their respective σs. The extreme case for this is expected in bulk three-dimensional (3D) TIs, where one channel has a bulk σ with insulating behavior at low T, and the other channel is a two-dimensional (2D) surface conductor with metallic behavior at low T.

If the geometrical factor has a strong T dependence, a single measurement geometry cannot distinguish between changes due to $\rho(T)$ and changes due to $g_{\mathrm{C,D;A,B}}(T)$.

Our goal, then, is to devise a scheme on a single sample with at least two contact geometries which respectively maximize and minimize the geometry's contribution to $R_{\mathrm{C,D;A,B}}(T)$. Such a scheme is diagrammed in Figure 3.1. A very thin crystal has a row of electrical contacts placed near each other in the center of both the front-side face and the back-side face. We use three measurement (geometry) configurations, listed below:

1. **Lateral**—Current is passed between contacts 1 and 4 on the front face. The voltage is measured using contacts 2 and 3 on the front face. This scheme minimizes the effect of $g_{\mathrm{C,D;A,B}}(T)$ by providing approximately the same current path to both the bulk transport and the surface transport. It is also similar to most previous measurements of single-crystal SmB_6.

2. **Hybrid**—Current is passed between contacts 1 and 4 on the front face. The voltage is measured using contacts 6 and 7 on the back face. This scheme has a much larger dependence on $g_{\mathrm{C,D;A,B}}(T)$. Because the sample is thin, the bulk transport geometry is similar to that of the Lateral scheme, and $R_{\mathrm{C,D;A,B}}(T)$ will mimic that of the Lateral scheme. However, the surface transport will give a very different result because, without bulk conduction, the voltage contacts (6 and 7) are electrically isolated from the majority of current flow, yielding a substantially smaller $R_{\mathrm{C,D;A,B}}$ than the Lateral scheme.

3. **Vertical**—Current is passed between contact 2 on the front face and the corresponding contact 6 on the back face. The voltage is measured using a different pair of front-side and back-side contacts, 4 and 8. This scheme maximizes the effect of $g_{\mathrm{C,D;A,B}}(T)$. If the current is a bulk current, the vast majority of it will pass directly through the bulk straight from 2 to 6. The voltage contacts (4 and 8), which are far from the current contacts compared to the current path, will only measure a tiny voltage. Conversely, if the current is a surface current, all

of it must flow around the long edges of the sample. The voltage contacts will then be quite close to the current contacts compared to the total current path, and will yield a very high value for $R_{\mathrm{C,D;A,B}}$.

FEA simulations[1] of each of these configurations are presented in Figure 3.2. Because each of the three configurations has such a different dependence on $g_{\mathrm{C,D;A,B}}(T)$, any shift in the current geometry should be immediately distinguishable. If $g_{\mathrm{C,D;A,B}}$ is T independent, all the measurement configurations will yield resistances that scale uniformly with each other and with $\rho(T)$. However, a scenario in which there is a crossover from bulk to surface conduction as T is lowered will yield resistances that behave quite differently from each other within the crossover temperature range.

3.3 Sample Fabrication

Perhaps the biggest challenge to the reinterpretation of the pre-TI SmB_6 literature within the context of surface conduction is the historical assumption that the residual is a bulk conduction, and that the geometrical dimensions of the crystals are therefore not important. Most of the studies [2, 9, 16, 32–34, 73] do not report the sample dimensions or surface treatments on the samples. The information presented here is therefore included for completeness, as well as to highlight some of the unique approaches to assembling this experiment.

3.3.1 Surface Preparation and Mounting

The SmB_6 crystals used were grown via the Al-flux-growth method. The most promising as-grown SmB_6 crystal we received from the crystal grower was nearly 400 µm thicker than desired, so we mechanically polished one side of it to a total thickness of 150 µm using silicon carbide (SiC) abrasive pads ranging from P1200

[1] The simulations themselves are discussed in Section 3.5

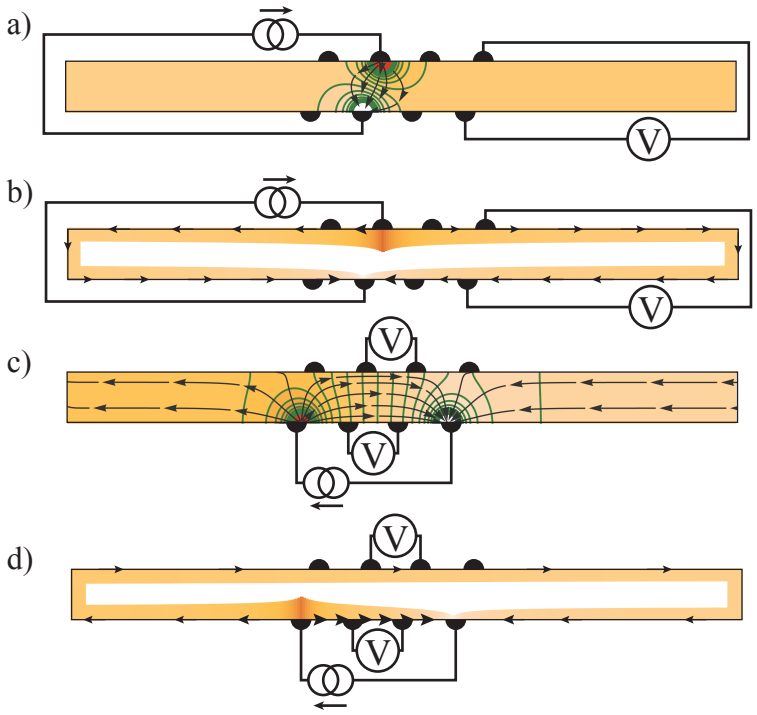

Figure 3.2: Cross sections of bulk slabs for three measurement geometries. The Vertical configuration is depicted for a bulk conductor and a surface conductor in (a) and (b), respectively. The Hybrid and Lateral configurations are shown together for a bulk conductor and a surface conductor in (c) and (d), respectively. Current is depicted by the black arrows, and the potential is depicted in shades of orange from light to dark. For the bulk cases ((a) and (c)), equipotential lines are shown in green. For the surface cases ((b) and (d)), the potential is also denoted by the thickness of the orange border.

(15 µm) to P2400 (6.5 µm) grit sizes.[2] Scanning Electron Microscope (SEM) images of the polished surface reveal pocks $1-2$ µm wide and scratches $\sim$0.25 µm deep (Figure 3.6 (g – k)). SEM images of the as-grown side are free from these polishing defects, showing a smooth surface with diffusely scattered debris <1 µm in size (Figure 3.6 (b – e)). The final sample was $2750 \times 1750 \times 210$ µm in size.

Contact pads for wire soldering were produced by lithographically patterning eight parallel 200 µm contacts spaced 50 µm apart onto a Si/SiO_2 wafer piece. Au was deposited via physical vapor deposition and liftoff. The resulting piece was then cleaved perpendicularly to the contacts, overlapping them by a small margin. Thus, each of the contacts extended all the way to the edge of the cleave and provided a relatively straight edge to butt against the flat SmB_6 crystal. Because the cleave did not always occur 90° to the surface, the lower corner of the substrate along the cleave edge was polished down by hand using the P1200-grit paper. Two of these contact pieces were prepared, one for each side of the SmB_6 crystal.

The SmB_6 crystal was bathed in dilute nitric acid (HNO_3) and hydrochloric acid (HCl) (1:1:50 HNO_3:HCl:H_2O) for several minutes. A small amount of bubbling occurred initially, indicating the etching of residual Al remaining on the surface from the flux growth.

The SmB_6 sample and the contact pieces were mounted to a substrate Si wafer piece using Torr Seal® vacuum epoxy, as shown in Figure 3.3. After the epoxy cured, the Au contacts on both sides of the SmB_6 crystal were nearly flush against the crystal surface, with a gap ranging from $3-20$ µm.

3.3.2 Ion-Beam-Induced Deposition

Typical procedures for attaching contacts to crystals for transport measurements include soldering (either by hand or using prefabricated solder balls), wirebonding,

[2]P grit sizes are specified by the Federation of European Producers of Abrasives. P1200 = American National Standards Institute (ANSI) 600 and P2400 = ANSI 800.

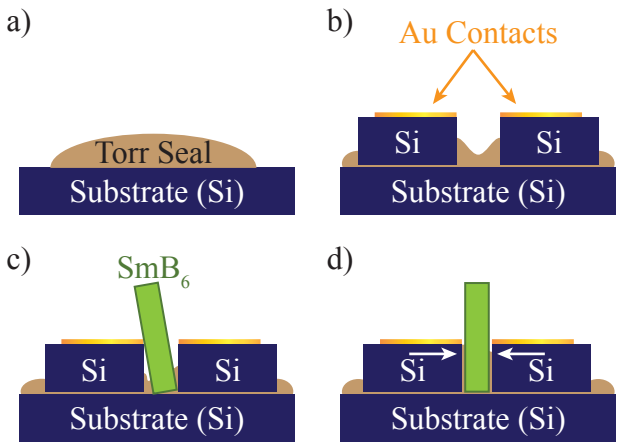

Figure 3.3: Diagram of sample assembly. (a) Torr Seal® vacuum epoxy is placed on a substrate. (b) Si wafer pieces with gold contacts are situated on the Torr Seal® with a gap between them. (c) The SmB_6 piece is placed upright in the gap. (d) The Si pieces are pushed together, holding the SmB_6 slab upright. The entire assembly is held in place by the Torr Seal®.

and painting with conductive epoxy, all of which have roughly 100 µm precision. Due to the small size of the crystals, a way was needed to make contacts much smaller than this, on the order of a few microns. On flat surfaces, lithographic procedures are sufficient for doing physical vapor deposition of contacts, but this doesn't work for the 90° junctions in the sample design. The solution was the unconventional use of Ion Beam-Induced Deposition (IBID) using a Focused Ion Beam (FIB). In this procedure, while the FIB is incident on a sample, a gas of metal carbonyls or metal-halogen complexes is injected near the focus spot. The ion beam breaks down the metal compound and deposits the metal atoms on the surface of the sample (Figure 3.4). Because the scanning of the FIB is under computer control, the resulting metal deposition can be patterned at a variable rate. In the electron beam version of this process, arbitrary nanoscale 3D structures are possible [74]. However, the deposition rates using IBID are much higher than for an electron beam, allowing the production of several 5 µm or 10 µm contacts in a few hours. Because the technique is capable of producing 3D structures, it is well-suited for shaping a contact across

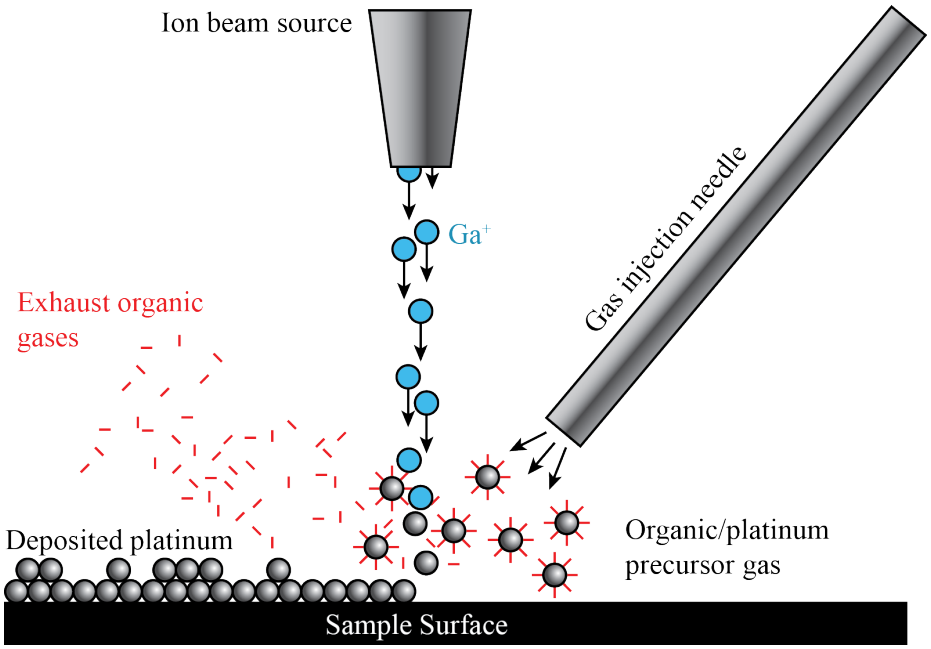

Figure 3.4: Diagram of typical IBID operation. A gas of metal carbonyls or metal-halogen complexes is injected through a needle near the ion beam focus spot. The ions break down the gas at the focus spot, and the free metal atoms stick to the substrate surface. The remaining gaseous organic products are removed by the ambient vacuum.

the 90° junction.

An FEI Nova Nanolab Dualbeam Focused Ion Beam Workstation and SEM were used to perform sample and contact imaging and Pt contact deposition. The electron beam and the ion beam were mounted at 52° with respect to each other; the sample was on a stage with three translational and two rotational degrees of manipulation. Figure 3.5 illustrates the sample and beam geometry during deposition.

Both circular and rectangular raster patterns were tested for making the contacts (Figure 3.7). SEM images of the resulting contacts are shown in Figure 3.6. The circular contacts were programmed to make 10 µm circles 5 µm tall, but typically grew as roughly spherical lumps (only one was deposited on the final sample, shown in Figure 3.6 (j)). In contrast, the rectangular contacts, programmed to make $5 - 10 \times 20 - 40$ µm rectangles 10 µm tall, resulted in lamella-shaped contacts that were

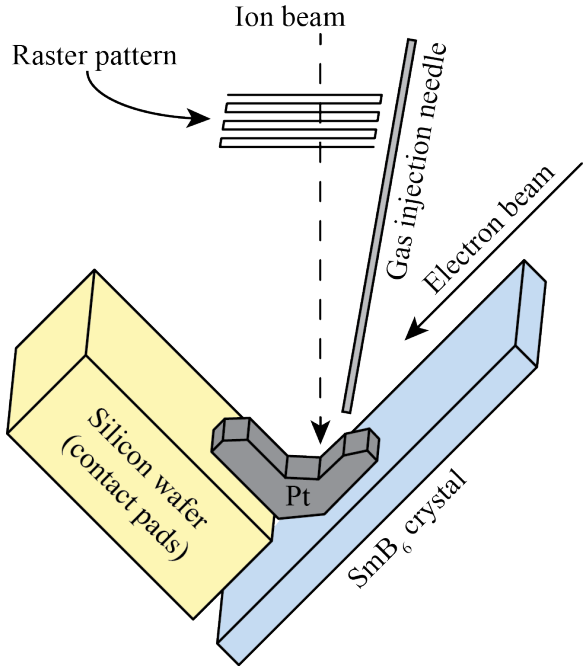

Figure 3.5: Orientation of ion beam and electron beam relative to the sample during IBID. The ion beam follows the raster pattern to deposit the platinum contact across the gap. The electron beam is used for viewing before and after the deposition.

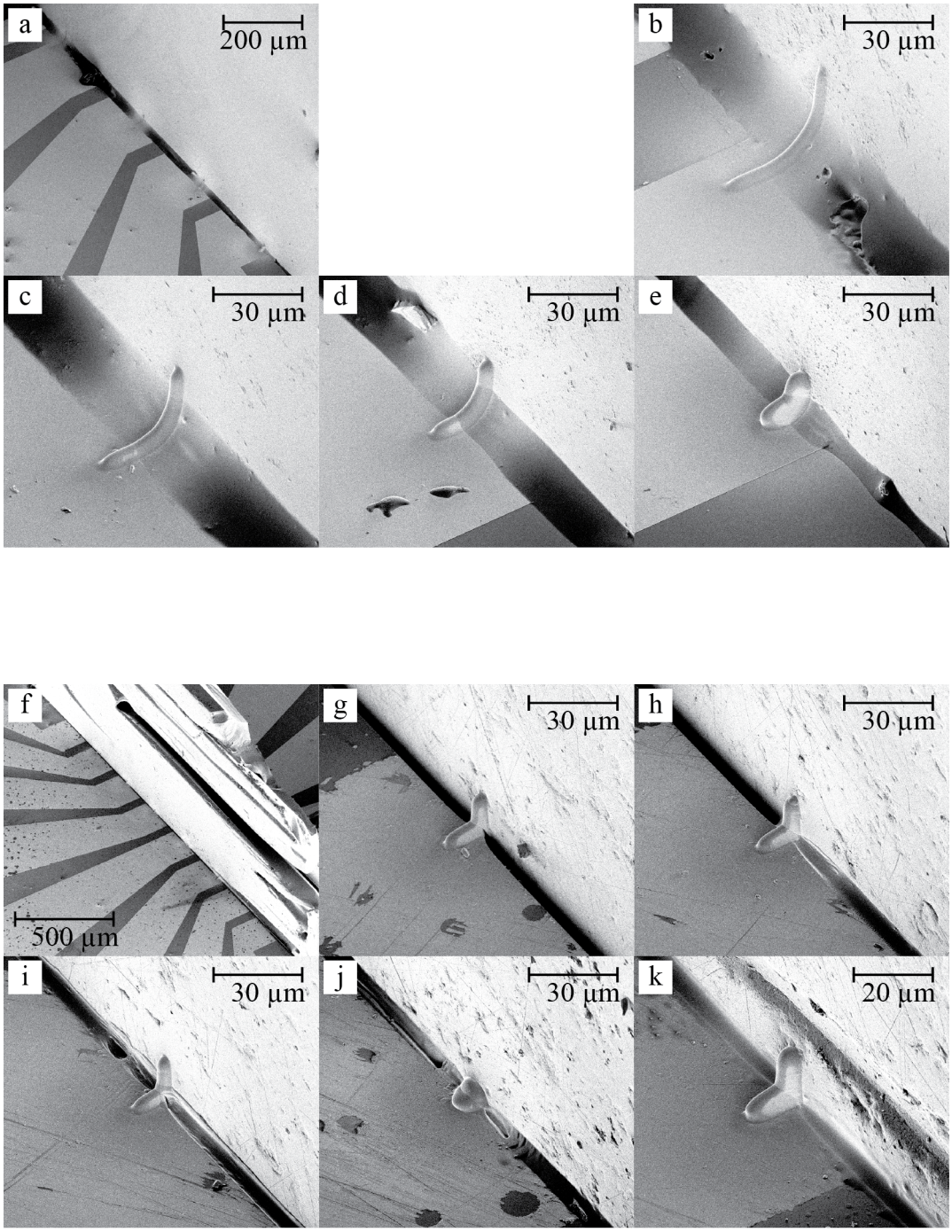

Figure 3.6: E-beam images of platinum contacts. (a) Interface between SmB_6 and contact pads, with four contacts visible, shown zoomed in (b – e). (f) Interface between SmB_6 and other contact pads, with five contacts visible, shown zoomed in (g – k).

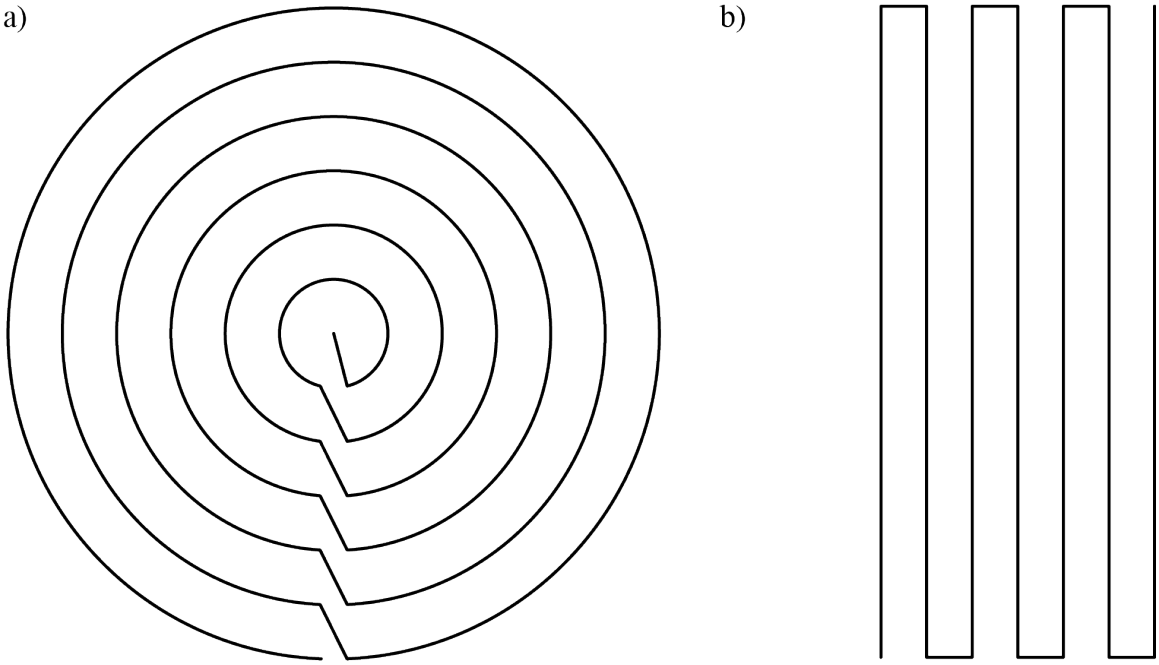

Figure 3.7: Raster patterns for IBID. (a) Pattern used for creating circular contacts. (b) Pattern used for creating rectangular contacts.

securely attached to both target pieces with a gentle L-bend at the 90° interface. What is particularly remarkable is that these L-shaped contacts spanned a gap at the interface that, in places, exceeded 10 µm without any special consideration beyond the programmed length of the contact. In some of the gaps between the contact pads and the SmB_6 in Figure 3.6 (b – e), the Torr Seal® wet the gap, providing an insulating bridge across the gap for the Pt contact. During the experiment, the smooth contacts shown in Figure 3.6 (b – e) behaved well with a linear response over the current range used and a two-terminal resistance below 1 kΩ. In contrast, the bent contacts shown in Figure 3.6 (g – k) suffered from high resistances or simply failed at cryogenic temperatures. Figure 3.6 also shows that a thin layer of Pt accumulated in halos around the deposition sites. This may have altered the quantitative resistances observed during the experiment, but does not alter the basic qualitative reasoning used to interpret the result.

Configuration	Current		Voltage	
Lateral	(b)	(d)	(c)	(e)*
Hybrid	(b)	(d)	(k)	(i)
Vertical	(i)	(c)	(k)	(b)

*This contact broke and was replaced by hand with a gallium blob ∼200 µm to the right of the original contact.

Table 3.1: List of contacts used for each measurement configuration. Each entry indicates the corresponding panel in Figure 3.6.

3.4 Experimental Methods and Data

The sample was mounted on a cryogenic insert and cooled in a variable-temperature cryogenic system. The four-terminal resistance was measured for each of the configurations discussed in Section 3.2 by passing an AC current of 50 µA at 17.759 Hz across two terminals and measuring the corresponding AC voltage across two different terminals using a Stanford Research Systems SR830 lock-in amplifier. Because the contacts on the side shown in Figure 3.6 (a) had low resistances, these were preferred for passing current. The contacts used for each configuration are summarized in Table 3.1, with each entry corresponding to a panel in Figure 3.6. The resistances obtained from each configuration are plotted on a log scale in Figure 3.8, and on a linear scale in the figure's inset. Interpretation of these results will be discussed in Section 3.6.

3.5 Finite Element Analysis Simulations

To better conceptualize the outcome of the transport experiment, Kai Sun performed FEA simulations of the crystal's electric potential for both the bulk residual scenario and the surface residual scenario. The single crystal in the experiment was modeled as a rectangular slab, subdivided into a $275 \times 175 \times 21$ grid of finite elements, maintaining the approximate aspect ratios of the real sample, with each grid

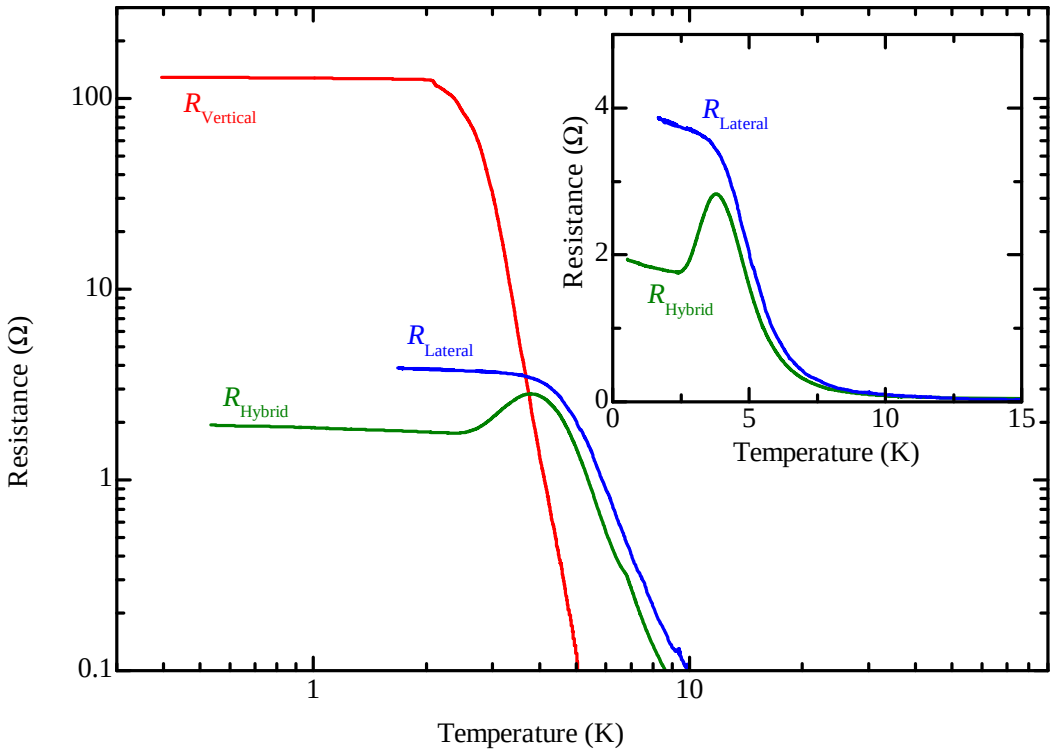

Figure 3.8: Four-terminal resistances plotted as a function of temperature. R_{Lateral}, R_{Hybrid}, and R_{Vertical} are shown in blue, green, and red, respectively. INSET: R_{Lateral} and R_{Hybrid} plotted with a linear scale.

element corresponding to a $10 \times 10 \times 10$ µm cube. Neumann boundary conditions were established using a flux of zero current everywhere along the surface of the slab except at the elements corresponding to the locations of the current contacts on the real sample, where a constant current (corresponding to a constant potential) could be tuned to match that of the experiment.

To simulate the experimentally observed behavior of the resistance for the bulk residual scenario, a two-channel bulk conductivity was used, one of which was a thermally activated transport channel with energy gap Δ and, in the $T \to \infty$ limit, resistivity σ_{a}. The other channel was a constant conductivity (of unknown physical origin) σ_0 corresponding to the plateau region of the resistance curve, giving, together with the first channel, the following:

$$\sigma(T) = \sigma_{\mathrm{a}} e^{-\frac{\Delta}{k_{\mathrm{B}}T}} + \sigma_0 \tag{3.5}$$

Meanwhile, for the surface residual scenario, the two channels were separated into two geometrically distinct rules. The thermally activated transport was used for all elements interacting with each of its neighbors, but the constant conductivity σ_0 was replaced by σ_{s} and restricted to occurring between surface elements. It is important to note that σ_{s} has a different unit dimension (Ω) than σ_0 ($\Omega \cdot \mathrm{cm}$) because it is a 2D conductivity rather than a 3D conductivity. In a thin sample, these are usually related by the thickness t of the slab ($\sigma_0 = t\sigma_{\mathrm{s}}$), but t is non-universal, varying from sample to sample.

For each of the two cases, the parameters Δ, σ_{a}, and σ_0 (or σ_{s}) were tuned to reproduce the Arrhenius curve (Lateral configuration) from the experiment. Cross sections of the slab showing current arcs and equipotentials are shown in Figure 3.2 for both the bulk-dominated conduction and surface-dominated conduction for each set of contact configurations. Simulated values for $R(T)$ from each measurement

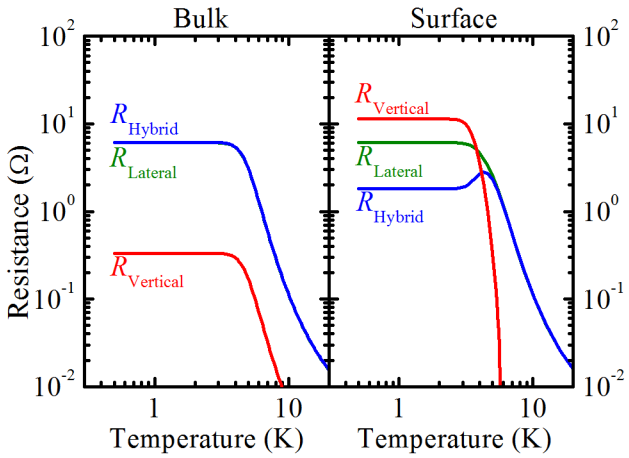

Figure 3.9: Simulated resistance curves from the FEA for each configuration. LEFT: simulated resistances for the bulk-residual scenario on a log-log plot. R_{Hybrid} and R_{Lateral} lie nearly on top of each other. RIGHT: simulated resistances for the surface-residual scenario on a log-log plot.

configuration are plotted in Figure 3.9 for both the bulk residual scenario and the surface residual scenario.

A few observations can be made from the simulations. Perhaps the most dramatic distinction is how each of the resistances in the bulk-residual scenario scales directly with each other with a fixed proportionality factor, reflecting the T dependence of $\rho(T)$ and the lack of T dependence in $g_{\text{C,D;A,B}}$ in each curve; meanwhile, in the surface-residual scenario, the resistances scale with each other at low and high temperatures, but they behave dramatically differently at an intermediate temperature regime ($\sim$3 – 5 K), the *crossover temperature*, reflecting the diverse changes in $g_{\text{C,D;A,B}}$ for each configuration as the conduction crosses over from bulk-dominated conduction to surface-dominated conduction. A second key observation is that R_{Lateral} and R_{Hybrid} are nearly identical when the bulk is the dominant conduction channel, but take very different values in the case of surface-dominated conduction, with a distinct peak in R_{Hybrid} around 4 K, the crossover temperature. A third important observation is that while R_{Vertical} follows $\rho(T)$ in the bulk-residual case, it changes by several orders of magnitude within the crossover temperature range in the surface-

residual case; this cannot be attributed to an intrinsic mechanism, but rather reflects the dramatic change in $g_{\mathrm{C,D;A,B}}$ for this configuration. A final observation is that in both of the simulated cases, R_{Lateral} has the same qualitative behavior, showing that the two cases can be indistinguishable when using this conventional measurement configuration alone.

3.6 Discussion of Experimental Results

The measurements of the real sample, shown in Figure 3.8, behave remarkably like the surface-residual case of the simulations, with a distinct peak in R_{Hybrid} at 3.8 K, demonstrating conclusively that SmB_6 becomes a surface conductor below this temperature. In particular, R_{Lateral} and R_{Hybrid} scale with each other on each side of the crossover regime, suggesting that the current path remains fixed at these temperatures, but they diverge near the crossover temperature, indicating a change in the current path. R_{Vertical} increases dramatically as the temperature drops below the crossover, even more than predicted in the simulation. This discrepancy is attributed to geometrical differences between the simulated slab surface and the real sample surface. These features cannot be explained by bulk conduction in any cubic system, even with the most extreme anisotropic conductivity.

This experiment proves unambiguously that as the temperature is reduced, the system turns from a 3D bulk conductor into a 2D surface conductor with an insulating bulk. It resolves the long-standing puzzles surrounding SmB_6 at low temperatures, which are caused by treating the low-T conductivity as a bulk conductivity. In fact, the RRR, which has historically been used to assess the quality of SmB_6 crystals, is now expected to be non-universal, depending on the bulk stoichiometry, the surface quality, and the sample thickness, which are all independent parameters. The implication, then, is that such historical experiments must be reinterpreted or even redone with this result in mind. For example, in the etching work done by Kebede *et al.* [33],

the thickness of the bulk was changed by etching. Even if the final surface has identical conditions to the initial surface (which should give the same total resistance), the apparent 3D resistivity changes because the thickness of the sample has changed.

In many cases, reinterpretation of the low-T conductivity is tenuous at best; not only is it necessary to know the sample thickness (which is often not reported) to obtain the correct 2D resistivity, but surface-dominated conduction implies all surfaces, including the sides and any unseen internal surfaces, can contribute to the conduction. This makes a determination of $g_{\mathrm{C,D;A,B}}$ impossible without detailed knowledge of the crystal's precise geometry and morphological quality. Even with this knowledge, surface conditions can also vary across a single sample, depending on preparation methods and exposure to ambient laboratory conditions. Any systematic approach to understanding the behavior of the surface conductivity must first address these difficulties.

CHAPTER IV

Magnetoresistance of SmB_6

4.1 Introduction

Since the surface state(s) experimentally demonstrated in Chapter III were virtually unstudied as independent 2D states, the first step in understanding these states is to perform magnetotransport measurements of the surface. A Hall bar structure is typically used to characterize the magnetotransport of both 2D and 3D conductive states. However, 3D TIs pose particular difficulties for this conventional geometry. Section 4.2 describes the first naïve attempts to perform magnetotransport measurements using a Hall bar structure, and also gives a discussion of the problems this geometry presents. This data has been published elsewhere [72]. Section 4.3 describes an alternative measurement configuration using a Corbino disk, which evades many of the difficulties presented by the Hall bar geometry. Section 4.4 covers the magnetotransport measurements performed below 3 K, including the negative MR that was observed at high fields, as well as the low-field hysteresis behavior of the surface. The data and discussion from this section have been published elsewhere [75]. Finally, Section 4.5 describes MR measurements at extreme magnetic fields across the crossover temperature range; the temperature dependence reveals closure of the hybridization gap as the field is increased.

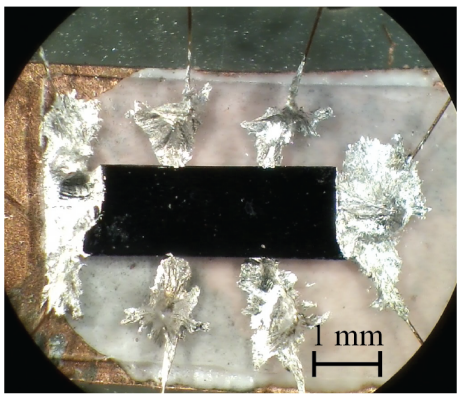

Figure 4.1: SmB_6 sample configured in van der Pauw-like geometry.

4.2 Hall Bars as a Poor Tool for Analyzing Surface Conduction

The first attempt at surface transport characterization was performed on a sample with a van der Pauw-like geometry [76]. The sample was 3.47 mm × 1.32 mm × 170 µm, and the two large faces were polished with P4000 grit paper. The sample was mounted to a glass substrate with Varian Torr Seal®, and indium contacts were placed along the edge (Figure 4.1). Two leads extended along the short edges to function as current leads, while four additional leads were placed along the long edges, two on each side, for voltage contacts. In this configuration, the geometry resembles that of two parallel Hall bars (the polished top and bottom surfaces of the crystal).

This geometry was used to naïvely determine the conductivity of the sample using two voltage leads on the same edge via lock-in techniques at 26.6 Hz in a ^{3}He cryostat. Below the crossover temperature, the sample had a remarkably low sheet resistance ρ_{xx} of 9.1 Ω. This geometry was also configured for Hall measurements using opposing leads on opposite edges, and the magnetic field was swept perpendicularly to the flat surfaces of the sample. The Hall measurements were pathological, with a barely detectable slope and a large temperature-dependent feature near 0 field (Figure 4.2 (a)). As the temperature is lowered, the Hall coefficient R_{H} rises in a manner

consistent with insulators, but it suddenly drops by about two orders of magnitude at the crossover temperature and plateaus at lower temperatures (Figure 4.2 (b)). Such a result would be difficult to interpret in the context of bulk conduction, but is completely expected in the surface-conduction scenario. This behavior is reminiscent of some prior Hall measurements of SmB_6 [16, 32], in which the Hall coefficient peaks at the crossover temperature, and drops and plateaus at a lower value at lower temperatures. In other measurements [9], the Hall coefficient dramatically changes sign at the crossover temperature. Of course, the quantitative details of the crossover and the plateau are expected to depend heavily upon the surface quality and preparation. For our sample, R_{H} above the crossover temperature is about a factor of 10 smaller than that reported by Cooley *et al.* [32], and at the lowest temperatures is less than $4 \times 10^{-4}\ \Omega/\mathrm{T}$.

The small-field peak is strong in our Hall measurements, but 10 times weaker in our measurements of ρ_{xx}. In fact, measuring ρ_{xx} using the contacts on the opposite edge of the sample changes the direction of the peak. Meanwhile, the value of ρ_{xx} measured on the opposite edge is only 43% of the first edge's value. The apparent symmetry of the sample in Figure 4.1 makes this discrepancy a mystery. From this, it is clear that the current does not flow uniformly along the long axis of the sample on the polished faces, as would be expected from the apparent geometry alone. Speculative ideas that could explain this discrepancy include variations in the conductivity along the sides or corners of the sample, hidden cracks or Al flux buried inside the sample with electrical access to the surface, or variations in carrier density across the surfaces that depend on the details of the surface morphology. In any case, it is clear that the geometry of the current is not really known, making a systematic study of transport parameters such as carrier density and mobility using this type of measurement unreliable, at best.

Nevertheless, it is instructive to compare the conductivity of SmB_6 to those of

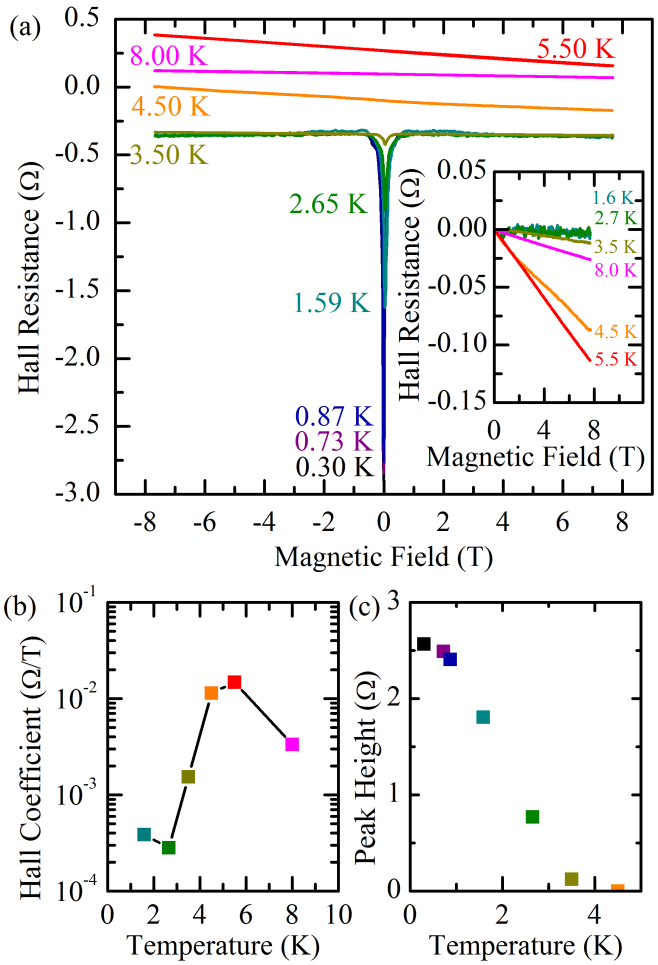

Figure 4.2: Hall data from the Hall bar sample. (a) Uncorrected values of ρ_{xy} plotted as a function of the magnetic field for various temperatures. INSET: Corrected values of ρ_{xy} for select temperatures. (b) R_{H} obtained from the (a) inset, plotted versus temperature. (c) Height of the anomalous peak of ρ_{xy} at 0 field, plotted versus temperature.

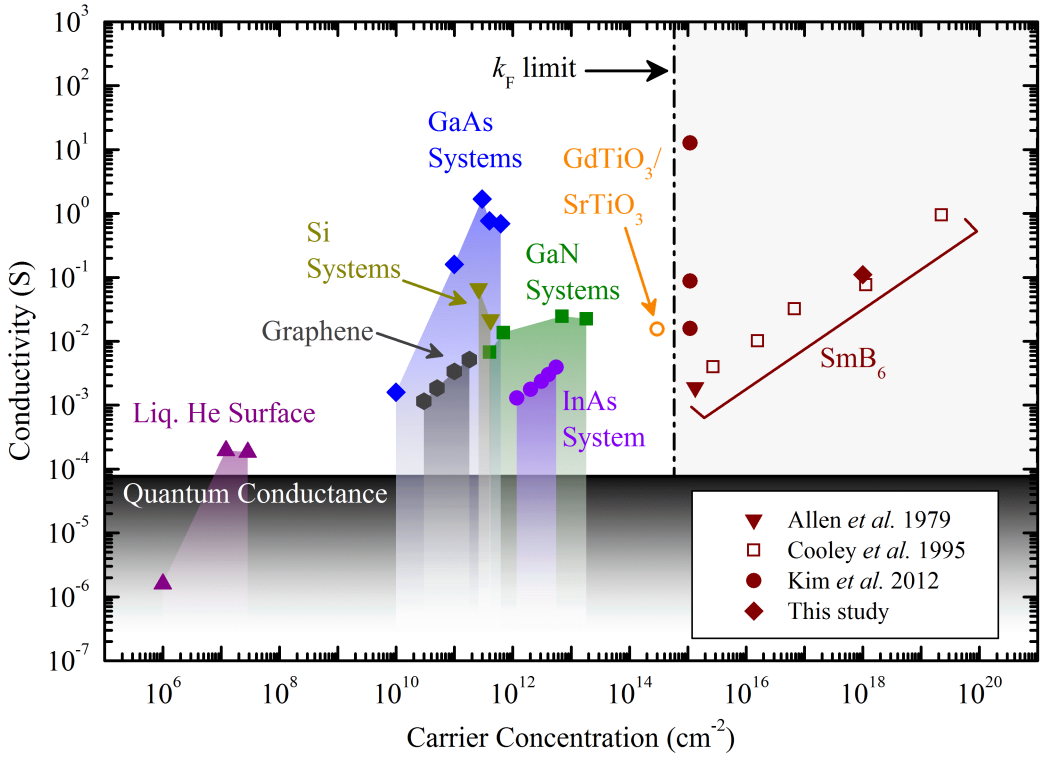

Figure 4.3: Comparison of SmB_6 conductivities with conventional 2D electron gas structures.

other 2D electron systems. Figure 4.3 plots several early measurements of the SmB_6 surface [16, 32, 72, 77] alongside some of the record conductivities for these systems as a function of carrier density. These systems include GaAs/AlGaAs [78–80], GaN/AlGaN [81–83], and InAs [84] heterostructures; graphene [85]; Si surfaces [86, 87]; the $GdTiO_3/SrTiO_3$ interface [88]; and the surface of liquid He [89, 90]. (Historic measurements [16, 32] of SmB_6, originally interpreted in the context of 3D conduction, have been re-evaluated here based on estimates of the crystal size via private communication [91].) The quantum conductance is included for comparison. The k_F limit, *i. e.*, the upper limit on the carrier concentration imposed by the BZ and corresponding to one carrier per unit cell, is also shown.

First, the range of conductivities reported both from historic measurements and current data is competitive with the best 2D electron systems, despite being taken

after exposure to various surface conditions including ambient air and polishing materials. This is in stark contrast to conventional systems, in which the 2D layer is protected by a cap layer or measured *in situ* in ultra-high vacuum. Second, all the various estimates of the SmB_6 carrier density are higher than is physically possible for a 2D electron system. The resolution of this discrepancy is not obvious, but perhaps the most likely explanation is that the conduction is not limited to the visible slab surfaces. Rather, additional surfaces may lie beneath the exterior surfaces, contributing to the conduction and giving the impression of a higher carrier density. This possibility is discussed further in Chapter V, and it has particular implications for the interpretation of the pressure study data by Cooley *et al.* [32]. Cooley says the following of this experiment:

> One caveat to keep in mind is that in the bridgeman [*sic*] cell brittle samples always fracture, so when I depressurized and took them out, all you get is small chunks. In addition, the capacitance of the measurement circuit changed as pressure was increased [*sic*] and I always assumed it was due to cracking of the sample. So there may be some extra surfaces from the cracking which are jammed tightly together, but one must be careful to point out that is speculative [91].

Although only a few studies on the material involved high-pressure cells, the complication posed by unknown or unaccounted surfaces is a general one that makes the (re)interpretation of many transport measurements difficult at best. The present effort to mitigate this problem involves a transport geometry that is sensitive only to a single surface—the Corbino disk.

4.3 Corbino Measurement Geometry

Although a Hall bar structure is typically used to characterize magnetotransport of both 2D and 3D conductive states, 3D TIs pose particular difficulties for this conventional geometry. All surfaces of the Hall bar contribute to the total conduction, including any edges or corners that are not perpendicular to the magnetic field, and may vary in surface condition due to preparation procedures such as polishing. For example, this can lead to an effective "edge channel" that would short the quantum Hall insulator state of the surfaces perpendicular to the field. Another complication arises if the surface states exhibit ambipolar conduction, as is indicated in calculations by Lu *et al.* [92]. The value of R_{H} is sensitive to charge sign, and in a multi-channel scenario with both electron and hole conduction, the contributions of one channel to R_{H} can compensate the other. In Section 4.2, the Hall bar measurements on SmB_6 [72] indicated carrier densities that were unphysically large for a 2D system, as shown in Figure 4.3, perhaps because any or all of these complications reduced the measured value of R_{H}. Unfortunately, these complications also now make a large volume of detailed low-temperature transport work in SmB_6 (which assumed the low-temperature resistivity plateau to be a bulk effect) very difficult to interpret, especially since details about crystal size and geometry are usually not reported.

These particular difficulties can be avoided by fabricating Corbino disks on single surfaces of SmB_6. This geometry is not sensitive to the sign of the charge(s), and it is sensitive only to the surface on which it is fabricated. The longitudinal conductivity σ_{xx} of the surface can be directly obtained from the two-terminal resistance and the geometry of the disk. There is a geometrical diminution of σ_{xx} under a perpendicular magnetic field because the current begins to circulate, lengthening the path over which an average charge carrier must travel through the system. This spiraling current was first described by Boltzmann in 1886 [93], but the idea was treated specifically for disks by Corbino in 1911 [94], who performed measurements of the circulating current

in bismuth disks. The diminution of σ_{xx} was derived four years later by Adams [95], who calculated the circular current due to the magnetic field as though it were an effective circular electric field or electromotive force. This permits a calculation of the power dissipation by both the radially- and circularly-directed currents. The conductivity of a single-carrier system is then given by

$$\sigma_{xx}(B) = \frac{ne\mu}{1+\mu^2 B_\perp^2}, \tag{4.1}$$

where n is the carrier density of the surface, μ is the carrier mobility, and $B_\perp$ is the perpendicular component of the magnetic field. For this work, the dependence on the magnetic field allows us to obtain values for μ and n. A modern derivation of these transport equations follows, including the treatment of multiple superimposed carrier channels and B dependence of μ and n.

4.3.1 Macroscopic Transport Equations

Let us consider a 2D disk of inner radius a and outer radius b, with total current I flowing from a to b, as shown in Figure 4.4. The total current density $\vec{\jmath}$ is related to the electric field $\vec{E}$ by the conductivity tensor $\boldsymbol{\sigma}$ via Ohm's Law: $\vec{\jmath} = \boldsymbol{\sigma}\vec{E}$. Because the scenario has radial symmetry, and because $\vec{E} = E_r\hat{r}$, we can write $\vec{\jmath}$ as:

$$\vec{\jmath} = \sigma_{xx}E_r\hat{r} + \sigma_{xy}E_r\hat{\phi} \tag{4.2}$$

$$j_r = \frac{I}{2\pi r} = \sigma_{xx}E_r \Rightarrow E_r = \frac{I}{2\pi r\sigma_{xx}}$$

$$V = \int_a^b \vec{E}\cdot \mathrm{d}\vec{r} = \int_a^b \frac{I}{2\pi r\sigma_{xx}}\mathrm{d}r = \frac{I}{2\pi\sigma_{xx}}\ln\frac{b}{a}$$

$$R \equiv \frac{V}{I} = \frac{\ln {}^{b}\!/_{a}}{2\pi\sigma_{xx}} \tag{4.3}$$

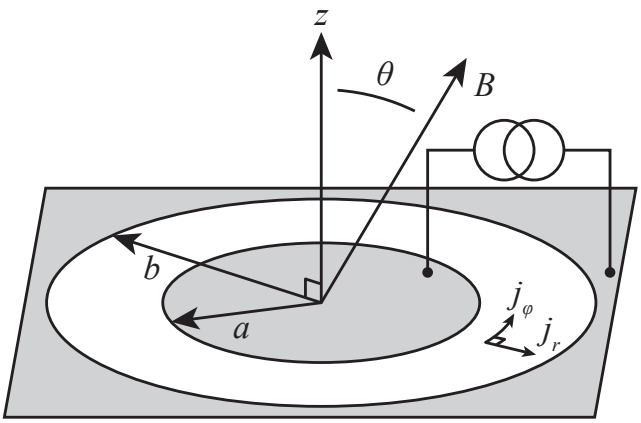

Figure 4.4: Corbino geometry diagram. The shaded areas represent the perfectly conducting current source and drain. The annulus between them is the active region under study.

We can check that this gives the correct expression for power. Microscopically, power is given by the rate of work done by the electric field on the charges $\vec{E} \cdot \vec{\jmath}$, so integrating this over the whole disk gives

$$P = \iint \vec{E} \cdot \vec{\jmath} r \mathrm{d}r\mathrm{d}\phi = 2\pi \int_a^b E_r^2 \sigma_{xx} r \mathrm{d}r = \frac{I^2}{2\pi\sigma_{xx}} \ln \frac{b}{a} = I^2 R.$$

Thus, regardless of the microscopic details, we can use R or P as a direct measure of σ_{xx}. However, none of these quantities depend directly on σ_{xy}; *i. e.*, this measurement geometry is not sensitive to the circular current j_ϕ *at all*. This is a sensible result because the electric field has no circular component, and the magnetic field can do no work on the system. However, this does not preclude the influence of the magnetic field and the circular current on σ_{xx}, as we will see.

4.3.2 Microscopic Transport Equations

Macroscopic quantities express the boundary conditions of the system in terms of experimental variables such as I, R, P, and V. These relationships do not depend on the microscopic details of the system, but are connected to them via the microscopic quantities $\vec{E}$, $\vec{j}$, and $\boldsymbol{\sigma}$. Let us now examine a single-carrier charge current in the Drude model by introducing a drag force $\frac{-\vec{v}m}{\tau}$ on single carriers, where $\vec{v}$ is the average drift velocity of an average carrier, m is the effective carrier mass, and τ is the average scattering time for the carriers. In a steady-state current, average acceleration of the carrier is 0, so we have (for positive charges):

$$\frac{\vec{a}}{m} = \vec{F} = e(\vec{E} + \vec{v} \times \vec{B}) - \frac{\vec{v}m}{\tau} = 0$$

so

$$\mu(\vec{E} + \vec{v} \times \vec{B}) = \vec{v}$$

where $\mu \equiv \frac{e\tau}{m}$. Inserting $\vec{E} = E_r\hat{r}$ and $\vec{B} = B_z\hat{z}$, we have from the two vector components:

$$\mu(E_r + v_\phi B_z) = v_r$$

$$-v_r \mu B_z = v_\phi$$

(Note that even if $B \neq B_z\hat{z}$, only the z component matters here because $v_z = 0$ and F_z does not affect the motion in the r–ϕ plane.) Solving for v_r, we get

$$v_r(1 + \mu^2 B_z^2) = \mu E_r \Rightarrow v_r = \frac{\mu}{1 + \mu^2 B_z^2} E_r \text{ and } v_\phi = \frac{-B_z \mu^2}{1 + \mu^2 B_z^2} E_r$$

The microscopic current is now

$$\vec{j} \equiv ne\vec{v} = \begin{pmatrix} 1 \\ -\mu B_z \end{pmatrix} \frac{ne\mu}{1+\mu^2 B_z^2} E_r \tag{4.4}$$

Thus, from Equation 4.2,

$$\sigma_{xx} = \frac{ne\mu}{1+\mu^2 B_z^2}$$

$$\sigma_{xy} = \frac{-ne\mu^2 B_z}{1+\mu^2 B_z^2}$$

If we assume that n and μ do not change with respect to B, then the total resistance from Equation 4.3 becomes

$$R = \frac{\ln {}^{b}\!/_{a}}{2\pi ne\mu}(1+\mu^2 B_z^2),$$

μ can be determined by the quadratic out-of-plane magnetic-field dependence, and n can be determined by the zero-field ($\vec{B} = 0$) value of R.

4.3.3 Multiple Carrier Channels

Now let us consider the scenario with multiple carrier channels with density n_i, scattering time τ_i, effective mass m_i, and mobility $\mu_i \equiv \frac{e\tau_i}{m_i}$. Each channel has microscopic current $\vec{j}_i = n_i e\vec{v}_i$, where $\vec{v}_i$ is the drift velocity for each carrier type.

If the carrier channels do not interact microscopically, then the force analysis from Section 4.3.2 can be applied to each channel individually. Specifically, $\vec{E}$ and $\vec{B}$ can be treated as external variables, $\vec{B}$ being determined by the experimenter, and $\vec{E} = E_r(r)$ being measured via V, as shown in Section 4.3.1. In any case, we wish to relate individual carrier characteristics to the measured quantity σ_{xx}, which is still related to $\vec{E}$ and the total current density $\vec{j} = \sum_i \vec{j}_i$ by Ohm's law $\vec{j} = \boldsymbol{\sigma}\vec{E}$. From

Equation 4.4, we have:

$$\vec{j_i} = n_i e \vec{v_i} = \begin{pmatrix} 1 \\ -\mu_i B_z \end{pmatrix} \frac{n_i e \mu_i}{1 + \mu_i^2 B_z^2} E_r$$

$$\vec{j} = \sum_i \begin{pmatrix} 1 \\ -\mu_i B_z \end{pmatrix} \frac{n_i e \mu_i}{1 + \mu_i^2 B_z^2} E_r$$

Thus,

$$\sigma_{xx} = \sum_i \frac{n_i e \mu_i}{1 + \mu_i^2 B_z^2},$$

$$\sigma_{xy} = \sum_i \frac{-n_i e \mu_i^2 B_z}{1 + \mu_i^2 B_z^2},$$

and the total resistance becomes

$$R = \frac{\ln {}^b\!/_a}{2\pi} \left(\sum_i \frac{n_i e \mu_i}{1 + \mu_i^2 B_z^2} \right)^{-1}. \tag{4.5}$$

This result is nice, in that σ_{xx} is just the sum of "individual" carrier densities, as though we were simply connecting two conducting circuits in parallel. Unfortunately, this result is far less tractable than the single-carrier result, since the resistance no longer has a simple quadratic form. However, if the mobilities of all the carriers are identical, then the result would again become quadratic as

$$R = \frac{\ln {}^b\!/_a}{2\pi (\sum_i n_i) e \mu} (1 + \mu^2 B_z^2).$$

If we change the charge sign of a carrier, $j_{i,r}$ remains the same, but $j_{i,\phi}$ will reverse sign. Because R depends only on σ_{xx}, it is not sensitive to the charge sign. However, an experiment that can measure the circular current, such as a magnetic torque measurement, would reveal the change in the circular current direction. In the case of ambipolar conduction (both positive and negative charge carriers present),

the radial components of each charge current will add, while the circular components will partially or completely cancel.

4.3.4 $\vec{B}$-dependent n and μ

Suppose we now wish to consider the possibility that in some intrinsic way, the carrier density and mobility of each carrier type depends on the magnetic field.

Let us first consider $n(\vec{B})$. Because $n(\vec{B})$ is a scalar quantity that does not depend on the dynamics of individual charges, the relevant change is that $\vec{j_i} = n_i e\vec{v_i} \rightarrow \vec{j_i}(\vec{B}) = n_i(\vec{B})e\vec{v_i}$. This change is easily incorporated into Equation 4.5 as:

$$R = \frac{\ln {}^{b}\!/_{a}}{2\pi}\left(\sum_i \frac{n_i(\vec{B})e\mu_i}{1+\mu_i^2 B_z^2}\right)^{-1}.$$

The relevant physical mechanisms for a changing carrier density can generally arise from two places. If the change is due to the magnetic field's influence on a 3D bulk material, the carrier density will be independent of the field direction, and depend only on $\|\vec{B}\|$. If the change is due to the direct influence of the field on the 2D states in question, the carrier density will depend on B_z.

Let us now consider $\mu(\vec{B})$. In this derivation, we have assumed that the scattering time τ_i (and thus the mobility μ_i) is isotropic along the r and ϕ directions. If this is the case, then replacing $\mu_i \rightarrow \mu_i(\vec{B})$ leads quite simply to

$$R = \frac{\ln {}^{b}\!/_{a}}{2\pi}\left(\sum_i \frac{n_i e\mu_i(\vec{B})}{1+\mu_i^2(\vec{B}) B_z^2}\right)^{-1}.$$

Like the carrier density, the scattering times can also generally vary with two types of mechanisms: 3D $\|\vec{B}\|$-dependent scattering and 2D B_z-dependent scattering.

Suppose we have a single-carrier system with field-angle-independent carrier density $n(\vec{B}) = n(\|\vec{B}\|)$. Let θ represent the angle between $\vec{B}$ and $\hat{z}$ such that $B_z = \|\vec{B}\|\cos\theta$, as shown in Figure 4.4. Taking the ratio of R obtained at any arbitrary

angle $\theta = \theta_0$ and $\theta = 90^\circ$ gives us

$$\frac{R_{\theta=\theta_0}}{R_{\theta=90^\circ}} = 1 + \mu^2(\vec{B})\|\vec{B}\|^2 \cos^2\theta_0$$

from which we can determine $\mu(\vec{B})$. If the mobility is independent of θ_0, the ratio will have a $\cos^2\theta_0$ dependence at constant field magnitude. If the mobility depends on B_z, the ratio will depend on higher powers of $\cos\theta_0$. Notice that in both cases, the ratio does not depend on $n(\|\vec{B}\|)$, allowing us to obtain $\mu(\vec{B})$. Furthermore, once $\mu(\vec{B})$ is known, the angle- and field-dependence of $n(\vec{B})$ can also be obtained from $R(\vec{B})$.

The situation is more complicated if $n(\vec{B})$ depends on θ. It is reasonable to suggest that $n(\vec{B})$ can be expressed as an even polynomial in powers of $\cos\theta_0$. The simplest case is that of a constant term and a $\cos^2\theta_0$ term, such that

$$R = \frac{\ln {}^{b}\!/_{a}}{2\pi} \frac{1 + \mu^2(\vec{B})\|\vec{B}\|^2 \cos^2\theta_0}{(n_0 + n_2\cos^2\theta_0)e\mu(\vec{B})}.$$

Even for $\vec{B}$-independent μ, this expression is becoming intractable, with dependencies on $\vec{B}$ and θ_0 that are difficult to separate. Unfortunately, this problem is compounded when the scenario with multiple carrier types is considered.

4.4 Magnetoresistance Below 3 K

With the advantages of the Corbino disk geometry discussed above, it is a natural choice for magnetotransport studies of SmB_6. The initial motivation for the transport study was to observe SdH oscillations characteristic of 2D electron systems. To this end, Corbino disks were fabricated on single-crystal SmB_6 pieces, and their resistances were measured in magnetic fields up to 45 T. Both (001) and (011) crystal surfaces were measured. In both cases, SdH oscillations were not observed, but angle-

dependent negative MR was observed. There were also low-field hysteretic features that bear resemblance to WAL, but unlike WAL, depend on the field sweep rate. The experimental setup and results are presented in this section, and various mechanisms for the observed phenomena are discussed, most notably the Kondo effect.

4.4.1 Experimental Methods

The single-crystal SmB_6 samples used for this study were grown by the Al-flux method. Typical pieces had $1-2$ mm $\times$ $600-1000$ µm surfaces and were thinned in the (001) or (011) crystallographic direction to $300-500$ µm thicknesses by manual polishing with coarse SiC grit or by automated lapping using Al_2O_3 slurry. The surface of interest on each piece was polished with SiC abrasive pads (grit size P4000) or 0.3 µm slurry. The Corbino disks were lithographically patterned with an inner diameter of 300 µm and an outer diameter of 500 µm. The surfaces were ashed with oxygen plasma, and 50/1500 Å Ti/Au contacts were evaporated onto the surface, followed by lift-off of the active region. Wires were attached to the contacts using Au or Al wirebonding, and the contacts were reinforced with silver paint for better adhesion where needed. For most of the samples, two wires for each source and drain were bonded so that the resistance of the wires could be neglected when performing four-terminal measurements. The completed devices are shown in Figure 4.5. Contact resistances were Ohmic both at 300 K and at 4 K.

The samples were characterized by alternating current (AC) resistance measurements at high magnetic fields using standard lock-in techniques in multiple magnet systems at the National High Magnetic Field Laboratory (NHMFL). Angle-dependent resistance measurements were performed in the NHMFL 35 T system using constant currents of 2 µA and 5 µA for the (011) and (001) surfaces, respectively. Measurements at lower fields were taken in a ^{3}He cryostat with an 8 T superconducting magnet and a ^{3}He/^{4}He dilution refrigerator with a 14 T superconducting magnet,

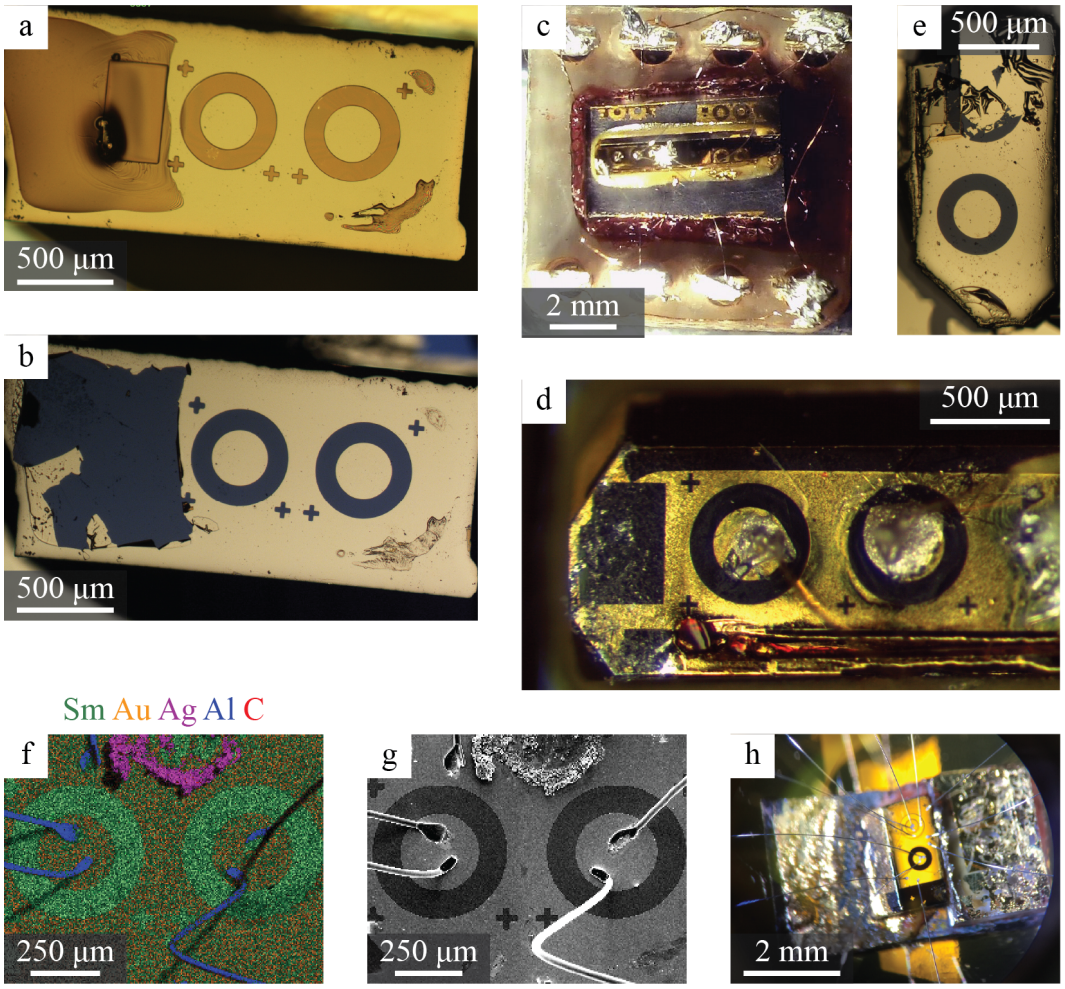

Figure 4.5: Corbino disk images. (a) Patterning two disks on a (001) surface. The darker regions have a layer of photoresist. (b) Sample shown in (a) after metallization and lift-off. The dark blue regions are exposed SmB_6 regions, while the gold region is the Ti/Au layer. (c) A long SmB_6 crystal with two disks patterned on the (011) surface. The crystal is glued to a Si wafer piece (gray), which is attached to the mount header with photoresist (red). (d) A close-up of the sample shown in (c), showing the disks' details. Silver-colored blobs are silver paint used to reinforce the wirebonds. (e) Another metalized disk fabricated on a (001) surface. (f) EDX composite image of the disks shown in (a) and (b), showing the relative concentrations of Sm (green), Au (orange), Ag (magenta), Al (blue), and C (red). (g) SEM image of the region shown in (f). (h) Two disks fabricated on a floating-zone-growth crystal (glued to a Si substrate) and wirebonded. The upper disk has an additional (failed) Au gate.

both of which were run using a bipolar magnetic power supply for which the current polarity switching occurs at $B \neq 0$ T. These resistance measurements were also taken using standard lock-in techniques, and in some cases, a pre-amplifier and a bridge circuit were also used to achieve clearer signals. The time constant that determines the low-pass filter bandwidth of the lock-in amplifier was set short enough ($\tau = 1$ sec) so that even at the fastest magnetic field sweep rates (32 mT/sec), the associated time delay was not significant. The excitation current ($I = 10^{-7}$ – 10^{-6} A) was sufficiently small that the measured resistance did not depend on the current or frequency.

4.4.2 Measurements of Magnetoresistance at Large Magnetic Fields

Figures 4.6 (a) and (b) show MR traces obtained at 0.3 K for multiple field angles, measured with respect to the surface normal, in the NHMFL 35 T system for the (011) and (001) surfaces of SmB_6, respectively. The most apparent feature for both surfaces is the strong negative MR at all measured angles. The traces show no signs of SdH oscillations for either surface up to 45 T, which is perhaps surprising in light of the observation of dHvA oscillations at lower field values [96].

One of the most striking features of the traces is their angle dependence, which is primarily a result of the perpendicular field dependence of σ_{xx} arising from the Corbino disk geometry and included in the denominator of Equation 4.1. Taking the ratio of traces for in-plane magnetic field and magnetic field with arbitrary angle θ with respect to the surface normal eliminates n and gives

$$\frac{\sigma(B_{\parallel})}{\sigma(B)} = 1 + \mu^2 B^2 \cos^2(\theta), \tag{4.6}$$

from which we can directly obtain μ. The ratio associated with each surface is plotted for different magnetic fields as a function of angle in Figure 4.6 (c) and (d), and for each angle as a function of magnetic field in Figure 4.6 (e) and (f). Both sets of

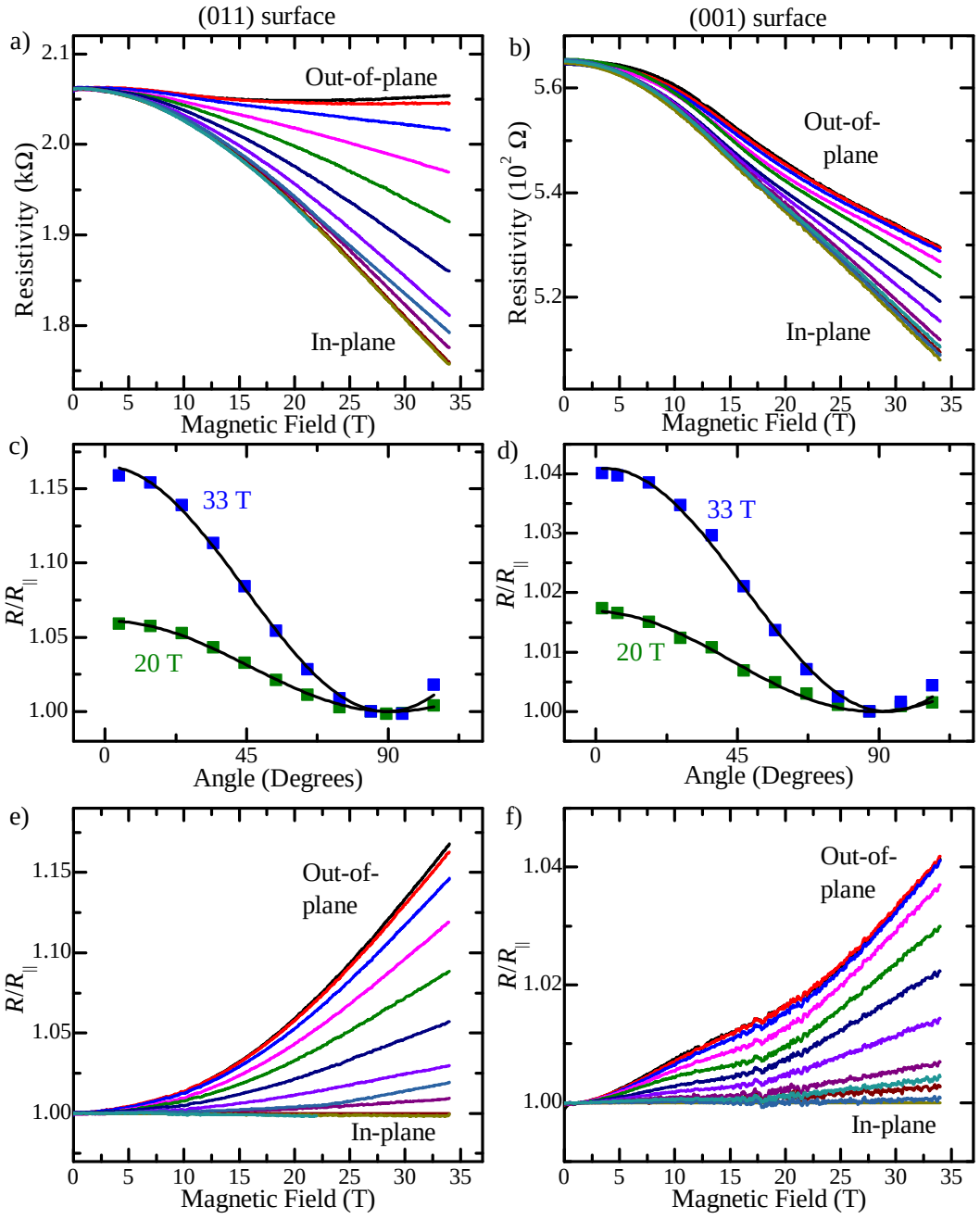

Figure 4.6: Magnetoresistance traces at several angles for (a) the (011) surface and (b) the (001) surface. Angle dependence of the ratio (points) of the resistance with out-of-plane field (R) to the resistance with in-plane field ($R_{||}$) for (c) the (011) surface and (d) the (001) surface at representative magnetic fields, along with $\cos^2\theta$ fits (lines). The ratio $R/R_{||}$ is plotted versus magnetic field for (e) the (011) and (f) the (001) surfaces.

ratios exhibit an apparent $\cos^2\theta$ dependence, which is the expectation for a surface conduction in the Corbino disk geometry (Equation 4.6), and the (011) ratios also approximately exhibit the expected B^2 dependence. Simple quadratic fits of the (011) field-dependent curves in Figure 4.6 (e) yield a carrier mobility of 123 $\mathrm{cm}^2/(\mathrm{V}\cdot\mathrm{s})$ and a carrier density of 2.5×10^{13} cm^{-2}. Both of these values are much lower than previously reported values for Hall bar transport measurements [72, 77], which may suffer from the problems discussed earlier. However, they are both more consistent with values from ARPES measurements [29, 97, 98] and other Corbino disk experiments [99], and the carrier density value is physically plausible with respect to the k_F boundary. Such a low mobility suggests that SdH oscillations will not be detectable below $\sim 1/\mu =$ 81 T, which explains why they are not observed. Meanwhile, the (001) ratios do not exhibit a simple B^2 dependence, most likely due to the presence of multiple carrier channels which may have different MRs. A two-carrier formulation (such as that in Section 4.3.3), in which the channels have similar conductivities but very different carrier mobilities, will yield a total $\sigma(B_\parallel)/\sigma(B)$ with a shape similar to the data ratios in Figure 4.6 (f), but it will not quite fit the data without additional MR-related contributions to each channel. However, the data does not sufficiently constrain the parameters of such a multiple-carrier fit with MR. Thus, in the analysis that follows, the focus will be limited to the (011) surface, except where noted.

The MR, which is not explicitly included in Equations 4.1 or 4.6, is due to B dependence of n, μ, or both. A more detailed analysis allows us to investigate the relative contributions of $n(B)$ and $\mu(B)$ to the MR. The coupling between the orbital motion of 2D surface electrons and the external magnetic field is expected to show a $\cos^2\theta$ dependence similar to that of Equations 4.1 and 4.6, and would not affect $\sigma(B_\parallel)$. Meanwhile, other mechanisms (*e. g.*, contributions from the Zeeman splitting) are expected to be independent (or weakly dependent) on θ. Because most of the θ dependence in the data comes from the Corbino disk geometry, and because

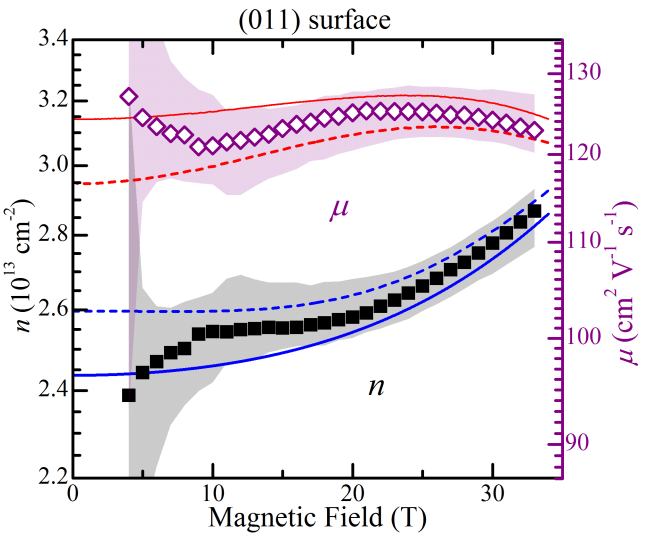

Figure 4.7: Plot of the (011) surface carrier density (filled squares) and mobility (open diamonds) obtained from angle-dependent fits of the data. Shaded areas represent uncertainty in the parameters of the angle-dependent fits. These are plotted together with best-fit curves for polynomial $n(B)$ (blue) and corresponding $\mu(B)$ (red) using the $\theta = 25°$ and $\theta = 85°$ data (solid lines), and using the $\theta = 5°$ and $\theta = 85°$ data (dotted lines). The vertical log scale allows direct comparison of the relative magnitudes of changes in n and μ.

$\sigma(B_\parallel)$ exhibits large MR, we proceed with the assumption that $n(B)$ and $\mu(B)$ are independent of the field angle θ.[1] The carrier densities and mobilities obtained from $\cos^2\theta$ fits at constant B (*e. g.*, Figure 4.6 (c) and (d)) are plotted as a function of magnetic field (symbols in Figure 4.7). The quality of the fits[2] at large B supports the assumption that $n(B)$ and $\mu(B)$ are independent of θ, and $n(B)$ and $\mu(B)$ can be obtained with good precision. However, the fits (and the analytical form of Equations 4.1 and 4.6, solved for $n(B)$ and $\mu(B)$) are divergently sensitive to noise near $B = 0$, so this method does not work well at low field values, which is evident in the uncertainty of the values in Figure 4.7.

[1] A small θ-dependent contribution is expected to arise from the weakening of TI backscattering suppression due to the magnetic field's influence on the helical spin dispersion (see Section 2.3) [58]. For SmB_6, $B_{TI} \approx 4.5$ kT, based on the values for v_F and k_F reported by Li *et al.* [96] and a generic g-factor of 2. For the field values measured here, $B/B_{TI} \leq 0.01$ (see Figure 2.1); this effect is therefore negligible. A smaller g-factor would reduce the effect even further.

[2] See Appendix A.

To overcome this, we assume that $n(B)$ can be approximated using an even polynomial in B. By treating the polynomial coefficients as fitting parameters, a best fit for $n(B)$ and $\mu(B)$ can be determined, constrained by two $\sigma(B)$ traces at different (arbitrary) θ. Details for the fitting procedure can be found in Appendix D. Solid (dotted) lines in Figure 4.7 show the best fit for a 6^{th}-order polynomial $n(B)$ using the $\theta = 85°$ trace and the $\theta = 25°$ ($\theta = 5°$) trace, along with the corresponding $\mu(B)$. Fits at other angles change the relative magnitude of $n(B)$ and $\mu(B)$ by <10%, suggesting some small angle dependence of $n(B)$ and $\mu(B)$ that is not sufficiently expressed in a two-parameter model, but the qualitative dependence on B remains the same. Both the θ-dependent fits and the B-dependent fits suggest that changes in carrier density are primarily responsible for the MR of the (011) surface; *i. e.*, the MR is a result of large changes in the carrier density accompanied by small changes in the carrier mobility.

For the (001) surface, a naïve application[3] of single-carrier $\cos^2\theta$ fits above ∼25 T yields a constant mobility of 61 $\text{cm}^2/(\text{V}\cdot\text{s})$ and an increasing carrier density around 2×10^{14} cm^{-2}. If such fits are believed, this suggests that the (001) surface's MR is also dominated by changes in carrier density. However, below ∼25 T, the fit residuals start becoming much larger. Meanwhile, a polynomial best fit of $n(B)$ fails to reproduce the B dependence of the data, giving credence to the notion that the analysis is complicated by the presence of multiple carrier channels with different MRs[4] or another unknown θ-dependent effect.

[3] See Appendix A.

[4] Multiple channels giving rise to visible MR features at distinguishable magnetic field values is an indication that the channels likely have carrier densities and mobilities that differ by orders of magnitude, but have resistivities of the same order. In fact, this is a reasonable expectation in a system that exhibits both large and small Fermi pockets, as has been observed on the (001) surface of SmB_6 both by ARPES and dHvA measurements. The large pocket, which is centered about the X point and has a large carrier density, may suffer from short-range disorder scattering and have a comparatively small mobility, as discussed later. Meanwhile, the small pocket, which is centered around the Γ point and has a smaller carrier density, may be dominated by long-range impurity scattering, which allows a much higher mobility.

4.4.3 Hysteretic Magnetotransport at Small Magnetic Fields

We now focus specifically on low magnetic fields, for which the response of the resistivity shows slow dynamical hysteretic behaviors. Specifically, the resistivity is dependent on the history of the magnetic field and its sweep rate. For this study, the magnetic field is swept slowly and continuously from $-B_{\max}$ to $+B_{\max}$, where $B_{\max}$ indicates the range of interest. The resistivity is measured while sweeping, and data is taken for sweeps in both directions at several sweep rates ($\mathrm{d}B/\mathrm{d}t$). Figure 4.8 shows typical resistivity traces of one of the Corbino disk samples at different sweep rates. This dynamical hysteretic behavior was observed in most of the samples. Using the arrows in the figure as a guide, the resistivity does not show any strong features while sweeping the magnetic field from -6 T ($-B_{\max}$) to 0 T. However, as the sweep continues from 0 to $+6$ T ($+B_{\max}$), a noticeable dip occurs. The resistivity first decreases to some minimum value. Then, the resistivity starts to return to its former path as the magnetic field continues to increase. When the sweep direction is reversed and the field is swept from $+6$ T ($+B_{\max}$) to 0 T, this dip does not appear. However, as the field continues from 0 to -6 T ($-B_{\max}$), the strong dip appears again. The two strong dips appear symmetrically for each polarity of the magnetic field. When the magnetic field sweep rate is increased, the magnitude of these dips becomes larger. Typically, these dips appear at magnetic fields smaller than ± 5 T. Hysteresis has also been reported by other researchers [100] at similar magnetic fields, but there are significant qualitative differences between those results and those of this study.

An additional hysteretic feature is observed in all of the samples studied at lower magnetic field ranges (within $\pm$ 1 T). These features, shown in Figure 4.9, were systematically studied on two samples as described above at lower temperatures (down to 60 mK) and extremely slow magnetic field sweep rates (down to 0.2 mT/s). The features have two symmetric dips similar to those in Figure 4.8. The hysteretic features are smaller, and the positions of the minima appear at a lower field range, but

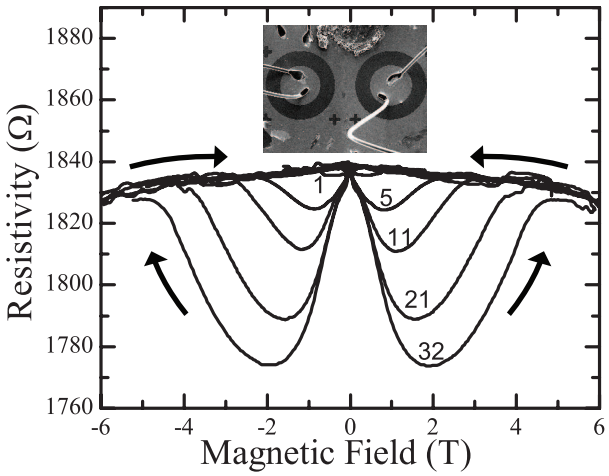

Figure 4.8: Response of the resistivity of the Corbino disk samples to the magnetic field below 6 T at 0.3 K for different sweep rates. The numbers shown next to each curve are the magnetic field sweep-rate magnitude in units of mT/s. INSET: Image of a Corbino disk sample prepared on a polished SmB_6 surface.

the qualitative magnetic field response remains the same. Previously, WAL has been reported [100, 101] within this range. However, the sweep-rate-dependent dynamic dips that are observed in Figure 4.9 are not caused by WAL. For the WAL case, the magnetic field only breaks the phase of the electrons traveling in a closed loop by scattering off static impurities, and this phase does not depend on $\mathrm{d}B/\mathrm{d}t$. If one were to hold the magnetic field sweep rate constant, the data do show some similarities to WAL. As shown in Figure 4.10, when the magnitude of the dips (ΔR) are converted to the change in conductivity ($\Delta\sigma$), the sizes are on the order of typical WAL peak magnitudes ($\sim 0.1e^2/h$). The value of $\Delta\sigma$ increases as the temperature is lowered, as is expected for WAL. However, WAL's response to the magnetic field must be static. Although the magnitude of the dips decreases at slower sweep rates, there is no sign of the dip magnitude saturating (becoming non-dynamic). The magnitude of the dips as a function of magnetic field sweep rate for both samples is shown in Figure 4.11. Even at the slowest measurements ($\mathrm{d}B/\mathrm{d}t = 5 \times 10^{-5}$ T/s), which takes more than 5 hours to change B by 1 T, the magnitude of the dips continues to shrink. In

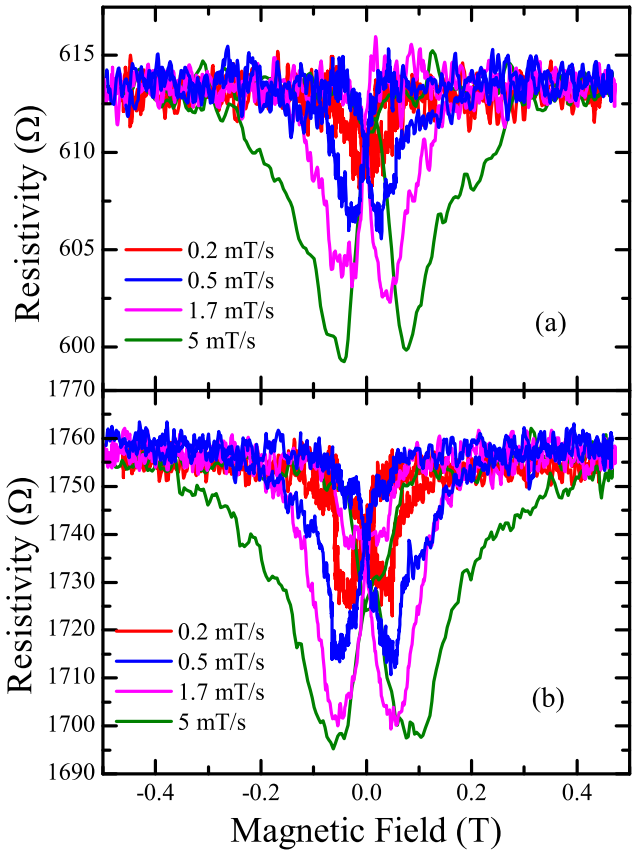

Figure 4.9: Response of the resistivity of the Corbino disk samples to the magnetic field below 1 T at 80 mK for different sweep rates. (a) (001) sample (b) (011) sample.

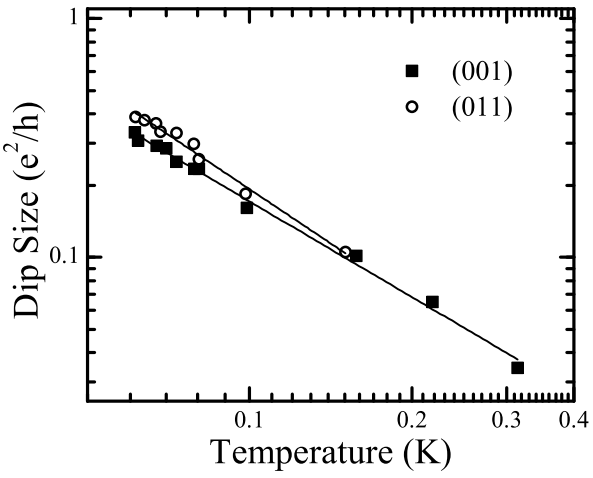

Figure 4.10: Magnitude of the dips (in conductivity) as a function of temperature at a magnetic field sweep rate of 0.167 mT/s.

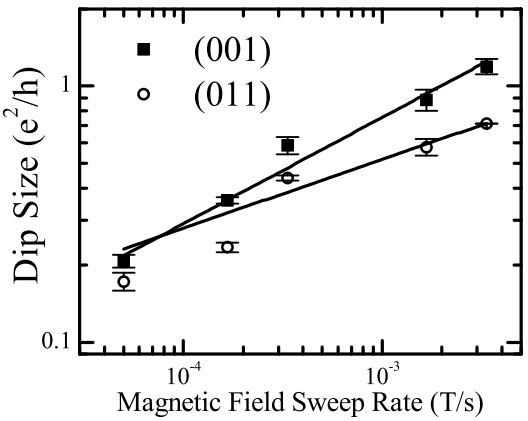

Figure 4.11: Magnitude of the dips (in conductivity) as a function of the magnetic field sweep rate at 80 mK.

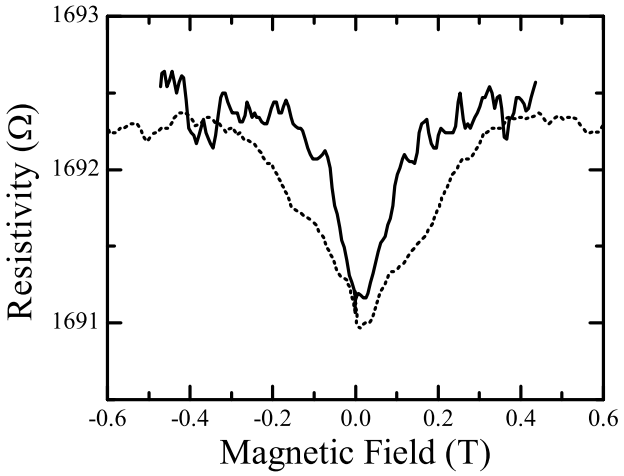

Figure 4.12: Resistivity of the Corbino disk samples at 0.3 K versus magnetic field perpendicular (solid curve) and parallel (dotted curve) to the transport surface. The minimal points are shifted to $B = 0$ T for direct comparison.

addition to these considerations, angle-dependent magnetic field measurements also indicate that this feature is not WAL. WAL is a function of the perpendicular magnetic field component [102]. As shown in Figure 4.12, however, the dips also appear in parallel (in-plane) magnetic fields, and they widen very slowly compared to what is expected from typical WAL as the field is rotated from the perpendicular to the parallel direction [102].

Since the hysteretic features are not due to WAL, we must assume that if WAL exists, it is buried under the hysteretic dips. For this to happen, since the WAL features are static, they must be smaller than the smallest hysteretic dip size that was observed ($\sim 0.2e^2/h$ in Figure 4.11). An estimation of the expected magnitude of WAL is calculated to be [102, 103]

$$\delta\sigma = \frac{\alpha}{2\pi}\frac{e^2}{h}\ln\frac{\tau_\phi}{\tau_p},$$

where τ_ϕ is the phase coherence time, τ_p is the momentum relaxation time, and α is the number of (identical) conduction channels. At the low temperature range measured (1 K – 60 mK), τ_ϕ can be theoretically estimated [104, 105], ranging on the order of 0.1 – 1.0 ns. Calculating τ_p requires the unknown effective mass, m^*, in addition to the mobility extracted from the high-field measurements ($\tau_p = m^*\mu/e$). If we use the effective mass from dHvA and ARPES measurements [29, 96–98, 106–110], where the effective mass is an order of magnitude smaller than the electron mass ($m^* \sim 0.1m_e$), the WAL feature magnitude must be larger than the dip sizes of the hysteretic peaks ($\delta\sigma \sim 0.7 - 0.89 \times$ number of conduction channels), which is inconsistent with the measurements. For the dip size to be on the order of $0.1e^2/h$ or smaller, the effective mass must be much larger than the electron mass ($m^* \gg m_e$). In the following section, a more plausible scenario is discussed, which can also explain the absence of WAL as partly due to the presence of magnetic impurities.

4.4.4 Discussion

4.4.4.1 Negative Magnetoresistance

Possible physical origins of the negative MR will now be discussed. Past measurements at 4 K [73] have also observed strong negative MR. These researchers, assuming they were measuring fully bulk properties, attributed the negative MR to closure of the bulk gap Δ and an increase in n_{bulk}. Indeed, 4 K is very near the reported [72, 77] crossover temperature between surface-dominated and bulk-dominated conduction for similar flux-grown crystals. However, these data are taken a full order of magnitude below the crossover temperature in a regime where the bulk is electrically dead,[5] and the conduction measured is purely due to the surface states (For a more complete discussion of this, refer to Section 4.5). In this regime, the carrier density of the bulk bands is not related to the surface conduction, and a change in activated bulk transport with gap reduction is unable to explain the negative MR observed. It is, however, possible that a change in the bulk structure could have some effect on the surface states at the Fermi level (especially a change in the Dirac point relative to E_{F}), causing a change in the surface state carrier density. Because the fits of the data indicate that $n(B)$ is the dominant source of the negative MR, it seems reasonable to attribute the negative MR to such a bulk-driven (θ-independent) picture. However, our collaborator's dHvA measurements [96] suggest that the carrier density does not change significantly up to 45 T for any θ. This disagreement, along with the large variations among reported [29, 96–98] values for n, μ, and k_{F} (see Table 4.1), remains to be resolved. Of course, it is difficult to compare values from the transport studies and the ARPES studies, since the ARPES is performed in high vacuum, while the transport samples are exposed to ambient air. Nevertheless, there does seem to be some consistency among the ARPES-obtained X-pocket n (multiplied by a factor of

[5] Pollution from bulk conduction at even 0.01% does not arise in an activated transport model until the bandgap is only 13% of its zero-field value, which happens at inaccessibly large magnetic fields.

Report	Crystal Surface	n (10^{13} cm^{-2})	k_F (nm^{-1})	μ (cm$^2 \cdot$ V$^{-1} \cdot$ s^{-1})	Reference
dHvA α	0 0 1	0.0716*	0.30	1100	[96]
dHvA β	0 1 1	0.705*	0.941	840	[96]
dHvA γ	0 0 1	0.928*	1.08	360	[96]
ARPES X	0 0 1	11.2†	(4.11, 3.44)	13	[29]
ARPES X	0 0 1	9.14†	(4.1, 2.8)	-	[108]
ARPES X	0 0 1	16.4†	(5.56, 3.7)	-	[97]
ARPES X	0 0 1	9.57†	(- , 2.9)	-	[98]
ARPES X	0 0 1	8.69†	(3.9, 2.8)	-	[107]
ARPES Γ	0 0 1	0.645†	0.9	-	[108]
ARPES Γ	0 0 1	1.15†	1.2	-	[97]
ARPES Γ	0 0 1	0.645†	0.9	-	[98]
Corbino disk	0 0 1	20.	-	133	[99]
Corbino disk	0 0 1	19.‡	-	61‡	[75]
Corbino disk	0 1 1	2.44	-	125	[75]

*Estimated from the oscillation frequency for a single pocket, using the Onsager relation $f = \frac{\hbar}{2\pi e} A(E_F)$.
†Estimated from k_F for a single pocket using $n = \frac{k_x k_y}{4\pi}$.
‡These values are suspect, as discussed in Section 4.4.2.

Table 4.1: List of reported surface transport parameters.

2, since there are two X pockets in the BZ) and Corbino-disk-obtained n for the (001) surface.

4.4.4.2 Kondo Scattering

If the B dependence of n is taken as a given, weaker features of the MR that are apparent in $\mu(B)$ can be investigated. Motivated by the observation of magnetic hysteresis at low fields (discussed in Section 4.4.3) [75], magnetic-impurity scattering can be assessed as a likely contribution to the negative MR. The Corbino disks' resistances were measured as a function of temperature with $B = 0$ (Figure 4.13). On both surfaces, as the temperature is reduced, a logarithmic increase of the resistance is observed, the coefficient of which is far from the quantum conductance e^2/h. This, taken together with the low-field increase in $\mu(B)$, suggests a TI surface Kondo scat-

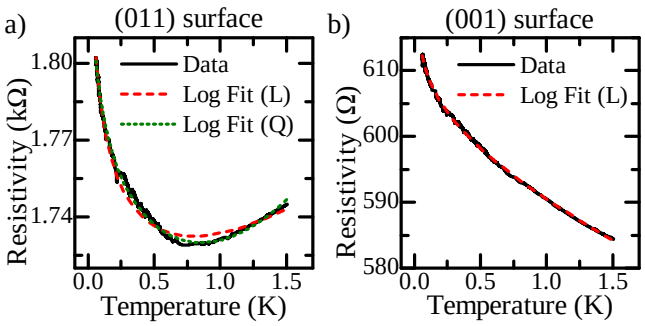

Figure 4.13: Resistivity versus temperature for (a) the (011) surface and (b) the (001) surface. The solid black line is data, the long-dashed red lines are logarithmic fits on a linear temperature background, and the short-dashed green line is a logarithmic fit on a quadratic temperature background.

tering mechanism [111, 112]. There are likely significant magnetic impurities on the SmB_6 surface, based on recent X-ray magnetic circular dichroism and X-ray absorption spectra which show that Sm^{3+} with a net magnetic moment is dominant on the surface [113]. In addition, Hard X-ray Photoelectron Spectroscopy (HAXPES) shows a weak oxygen signal from a polished and then etched SmB_6 sample [114]. These results imply that Sm_2O_3 is formed when the surface of SmB_6 is exposed to air at ambient conditions [114]. The native Sm_2O_3 formed on the SmB_6 surface is expected to be disordered. Therefore, Kondo scattering from disordered Sm^{3+} moments is assessed as a possible mechanism to explain both the temperature dependence and the low-field enhancement of $\mu(B)$.

The logarithmic T dependence of the electron scattering rate observed can be fit using the following formula [112], developed for a 3D TI system with dilute magnetic impurities:

$$\frac{1}{\bar{\tau}} \propto 3 + J\rho \ln \frac{T}{T_K}, \tag{4.7}$$

where J is the coupling constant, ρ is the density of states at E_F, T is the temperature, and T_K is the Kondo temperature calculated using the renormalization group approach. Here, $\bar{\tau}$ represents the scattering-angle-averaged scattering time, since the

spin–momentum locking of the TI surface states causes τ to depend on the scattering angle. For the SmB_6 surface, J might represent the coupling due to hybridization between the magnetic moments of the surface states and the paramagnetic Sm_2O_3 f states. The Kondo scattering produces negative MR according to the formula [111, 112],[6]

$$\frac{1}{\mu} = \frac{1}{\mu_{\mathrm{d}}} + \frac{1}{\mu_{\mathrm{M}}} \left(3 + J\rho \ln \frac{T}{T_{\mathrm{K}}}\right) \cos^2 \left(\frac{\pi}{2} M(B)\right), \tag{4.8}$$

where μ_{M} is the coefficient of the contribution from Kondo scattering, μ_{d} is the mobility from disorder scattering alone, and $M(B)$, for which the relationship to B can be exactly calculated at low temperatures [111], is the normalized magnetization of the impurities. Motivated by the experimental signatures of Kondo scattering, we now apply this theory to SmB_6, even though the surface magnetic moments from the Sm_2O_3 might not be in the dilute limit. At zero magnetic field (B, $M = 0$), the logarithmic fits shown in Figure 4.13, which include a linear background resistance of unknown origin, provide a way to experimentally determine μ_{d} and μ_{M}. The dependence on magnetic field (B, $M \neq 0$), which arises from the suppression of spin-flip scattering due to Zeeman splitting, can then be predicted as a function of T and T_{K}. Using the values from the logarithmic fits and for the value of $n(B = 0)$, computed values for $\mu(B)$ for several different Kondo temperatures are plotted alongside the fit of the experimental $\mu(B)$ for comparison, in Figure 4.14. The low-field increase in $\mu(B)$ fits quite well with Kondo scattering for $T_{\mathrm{K}} = 40$ K; however, this is only an estimate, since other effects such as short-range scattering (discussed below) can also influence $\mu(B)$. Note that if one were to ignore the evidence for B-dependent n and instead attribute the MR solely to changes in $\mu(B)$, such a naïve fit would yield a much larger negative MR than can be explained by Kondo scattering alone

[6] The reader is cautioned that this formulation may be quantitatively different from the 2D Kondo scattering description appropriate for surface magnetic impurities. However, the qualitative behavior will be the same, which is sufficient here because we take the magnitudes of μ, μ_{d}, and μ_{M} as fitting parameters in the subsequent analysis.

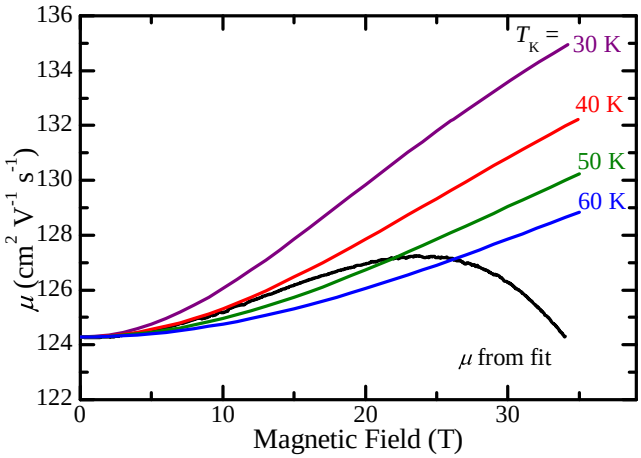

Figure 4.14: Fitted mobility alongside several mobility projections of the Kondo effect for various T_{K}.

(refer to Appendix B for an example calculation). The theoretical prediction and the experimental curve agree only by combining the Kondo effect together with the B dependence of the carrier density.

We now consider a qualitative picture in which an oxide layer with dense magnetic impurities can still lead to Kondo scattering behavior. Such a Kondo lattice is formed by conduction carriers from the SmB_6 surface interacting with a disordered dense array of localized moments from the Sm_2O_3. If we first consider an ordered Kondo lattice, as the temperature is lowered from high temperatures, the resistivity rises logarithmically as the magnetic ordering becomes quenched by Kondo cloud formation, where the spin scattering between the localized f electron and the d conduction electron inside the cloud increases. As the temperature is lowered further, the resistivity drops, since the effect of coherence between the lattice sites (Bloch's theorem) dominates, and the magnetic moment becomes quenched [115]. However, if the Kondo lattice system is disordered, a remnant magnetic moment is expected to exist in the system, and this downturn due to coherence can be averted. This remnant magnetic moment is expected to produce effective Kondo scattering, and the logarithmic increase of resistivity can still remain. Indeed, there are examples

of heavy fermion systems that show suppression of the downturn when even a small doping amount is introduced (*i. e.*, small disorder) [116, 117].

The downturn of $\mu(B)$ at higher magnetic fields is not a feature of Kondo scattering, but is qualitatively consistent with short-range disorder-scattering mechanisms. It has long been known [118] that in the high-carrier-density limit (in which the SmB_6 surface states live), the mobility is partially determined by short-range disorder-scattering mechanisms (*e. g.*, surface-roughness scattering) and scales inversely with the carrier density; *i. e.*, $\mu \propto n^{-\alpha}$, where α is determined by the particular scattering mechanism(s). This behavior has been observed in several semiconductor heterostructures [119]. In SmB_6, as $n(B)$ increases with increasing B, the short-range scattering time (and thus μ) decreases with B. Typical values for α between $\frac{1}{2}$ and 2 are consistent with the data. However, a precise determination of α from the data is problematic, because $n(B)$ only varies by 15% over the fields measured, and the dynamic range for determining a power-law relation is too small. This further complicates the determination of T_K, since the contribution to the mobility from the short-range scattering can compensate the contribution from the Kondo effect. (For example, for $\alpha = \frac{1}{2}$, a T_K of 30 K would give a better fit in Figure 4.14.) Nevertheless, this effect, together with the Kondo scattering, gives a picture that is qualitatively consistent with the $\mu(B)$ extracted from the fits, where the low-field negative MR is due mostly to Kondo scattering, and the high-field negative MR is due mainly to an enhancement in $n(B)$, which then causes a much weaker diminution of $\mu(B)$ via an increase in short-range scattering.

4.4.4.3 Weak Anti-localization

One likely reason that WAL is absent or too small to detect in these measurements is the existence of magnetic (Kondo) impurity scattering, a scenario which is consistent with the results for the temperature dependence and magnetic-field depen-

dence of the resistivity. Magnetic-impurity scattering plays a role in the quantum correction of conductivity, since it alters the dephasing of electrons. Here, there are two possible effects that can reduce the magnitude of the hysteretic dips. For non-TI two-dimensional electron gases (2DEGs), it is well-known that introducing a small number of magnetic impurities can even switch the signs of the dips of the quantum correction to conductivity [120]. For a topological insulator surface, there is an additional effect that results in a smaller feature size. By introducing magnetic impurities, the energy bandgap at the Dirac point opens, and this bandgap opening induces a crossover from WAL to WL [121]. These considerations, which are entirely expected in a system with magnetic impurities, fall outside the scope of the usual Hikami-Larkin-Nagoaka formulation [102] used to analyze WL and WAL.

Also, the magnetic field range appropriate for a quantum correction to conductivity on the SmB_6 surface might not occupy the typical range for such corrections. Ordinarily for disordered thin metals and other known TI surfaces [122, 123], the magnetic field range of interest for WAL or WL is 0.1 – 1 T. Theoretically, this range can be estimated by the characteristic field $B_\phi = (h/e)/8\pi l_\phi^2$ without magnetic impurity scattering. Since even a small amount of magnetic impurities can lower the phase coherence length by orders of magnitude [124, 125], the characteristic field can be much larger than 1 T. In future studies, a wider range of magnetic fields may need to be considered for WAL and WL.

4.4.4.4 Origin of the Dynamical Magnetotransport Feature

Let us now address the physical origin of the hysteretic features seen at low field values. Because SmB_6 exhibits no magnetic ordering at low temperatures, a magnetic hysteresis is likely to be extrinsic to the material, arising from the surface oxide (which may vary significantly across the samples) or some other material used to mount the samples in the cryosystems, and which is proximal to the samples. All the samples

measured exhibited the very-low-field ($\sim$0.05 T) peaks in multiple cryostats, but only some exhibited the higher-field (0.5 – 2 T) peaks.

The following extrinsic mechanisms can be ruled out:

- **Joule heating** – This mechanism can be detected by changing the current through the sample by an order of magnitude; no such change in the hysteretic behavior was observed during the experiments. Furthermore, the Joule heating power of the sample is orders of magnitude smaller than the cooling power of the cryogenic system.

- **Inductive heating** – Induced eddy currents depend on the magnetic field sweep rate, but are independent of the sweep direction. Since inductive heating is constant over the course of a fixed-rate sweep, the resistivity change of the sample due to inductive heating can only be monotonic and non-reproducible over several sweep cycles. However, the data have two non-monotonic dips which are reproducible at a constant sweep rate and temperature. Also, the magnitude of inductive heating at 0.3 K is orders of magnitude smaller than the cooling power of the cryostat. Additionally, the temperature fluctuations recorded by the thermometer are not large enough to indicate a global temperature change in the system.

- **Power supply switching** – If a unipolar power supply is used for the superconducting magnet, it can cause a dip in resistivity when it switches circuits at zero magnetic field. For this reason, a bipolar magnetic power supply, for which the switching event ($B \neq 0$ T) was identified, was used, and the dips were confirmed to be independent of this event.

One possible extrinsic source of the hysteretic behavior could be the magnetocaloric effect. In this scenario, the increase in magnetic field coerces the magnetic moments in a magnetic material to align with the field, which reduces the magnetic

entropy of the system. This process is adiabatic in the cryostat, leading to an increase in temperature. When the magnetic field is then reduced toward zero, the magnetic entropy can increase, leading to a decrease in the sample temperature. Such variations in the sample temperature would change the resistance according to Figure 4.13. Indeed, for most of the samples, the decrease in resistance as the field is increased would be consistent with a temporary increase in temperature. As the magnetization becomes saturated at higher fields, this warming effect would gradually disappear, allowing the cryosystem to cool the sample over a timescale of several seconds, consistent with the data, and allowing the resistance to return to its original value. If the source of the magnetization is located very near the sample, it may be sufficiently thermally isolated from the thermometer and the cooling power of the system to influence the sample temperature without influencing the thermometer.

The magnetic material that would be responsible for this effect is entirely unclear. SmB_6 itself does not exhibit magnetic ordering at low temperatures. The electronic leads to the samples include a number of possible superconducting materials, but these typically exhibit the inverse magnetocaloric effect, which has the wrong sign to explain the data, and they typically have critical temperatures well within or below the temperature ranges in which this effect is observed. There are also occasionally spasmodic, non-reproducible spikes in the data and an offset in the resistance that depends on sweep direction to fields as high as 8 T, well above the critical field for most superconductors. However, it is not likely that the magnetocaloric effect is responsible for these sporadic features.

Another possibility is that this hysteretic magnetotransport behavior with long time scales is related to the disordered Kondo lattice system formed by disordered Sm_2O_3 on the SmB_6 surface. In addition to the picture introduced in Section 4.4.4.2, the disordered Kondo lattice may also be a glassy system [126, 127]. Previously-studied disordered-Kondo-lattice models that are glassy assume that Ruderman-

Kittel-Kasuya-Yosida (RKKY) interaction strengths are randomly distributed. Here, there is the possibility that random superexchange interactions due to the varying angle of the Sm–O–Sm bonds may play a role similar to that of random RKKY interactions. The measured resistivity response to the low magnetic field may be a manifestation of the magnetization property of a glassy system. In a spin-glass system, the relaxation time of the magnetization can be extremely long [128]. Therefore, when an external magnetic field is applied, the magnetization depends on the magnetic field sweep rate, even when the sweep rate is very slow. In addition, the total magnetization of a spin-glass system exhibits a hysteresis loop, so the area of the hysteresis loop depends on the magnetic field sweep rate. Theoretically, the hysteresis area becomes larger at faster sweep rates and at lower temperatures [129]. In a scenario where the resistivity decreases when the magnetization decreases, the magnetic field history, sweeping direction, sweep rate, and temperature dependence of the data are all consistent with the magnetization of the glassy features explained above.

This glassy-magnetic-ordering scenario, along with the absence of WAL, is inconsistent with previous reports [100, 101]. Both of these previous studies reported observing WAL, and Nakajima *et al.* [100] additionally reported on sweep-rate-independent hysteresis as evidence of chiral edge channels from ferromagnetic domains. One possible explanation for this difference is that the surface magnetic ordering of our samples is quite different from that of the samples in those experiments, due to variations in the disorder of the native oxide after different sample preparation procedures, such as polishing and lithography. According to the disordered-Kondo-lattice model, the magnetic phase can change between spin glass and ferromagnetic ordering, depending on the degree of disorder [127]. Further systematic studies of surface preparation are needed to reconcile these differing findings. In addition, transport measurements performed in high vacuum on cleaved surfaces, on which there is presumably no oxide layer, would also be extremely powerful for the full characterization

of the surface states.

4.4.5 Summary and Outlook

Transport measurements of individual crystallographic surfaces of SmB_6 using Corbino disk structures have been performed. Both (001) and (011) surfaces display strong negative MR. The (011) surface exhibits a carrier density and mobility at values which are significantly lower than previously reported from transport methods, but which are more consistent with ARPES data. For both (001) and (011) surfaces, the temperature dependence suggests Kondo scattering from magnetic surface impurities. Fits of the angular dependence of the data suggest that the negative MR is primarily due to an increase in carrier density, especially at high fields, but with some additional contribution from the suppression of Kondo scattering.

All of the samples revealed a dip of resistivity which depended on the magnetic field sweep rate. Although these features become smaller in magnitude at slower sweep rates, the magnitude is still clearly visible at the slowest measurements. These features are most likely due to an extrinsic magnetic effect such as the magnetocaloric effect or magnetic-impurity scattering due to the presence of the naturally formed Sm_2O_3 layer, which might exhibit a glassy magnetic ordering. In either case, the behavior of the dip is inconsistent with WAL, and to the extent permitted by the dip at the slowest sweep rates, WAL is not observed. This lack of WAL could also be attributed to the effect of the magnetic surface impurities.

A TI with no bulk contribution can potentially be an ideal building block for realizing Majorana fermions and spintronics devices [40, 41, 130]. If the Sm_2O_3 is the leading magnetic impurity on the surface, the impurities, in principle, can be avoided using oxygen-free fabrication conditions. In this case, the surface of SmB_6 may be a strong candidate for this building block. Growing a heterostructure or a cap layer on top of the SmB_6 surface may be a possible solution for preventing the native Sm_2O_3

formation on the SmB_6 surface.

4.5 Bandgap Closure at High Magnetic Fields

4.5.1 Introduction

In the previous section, the focus has been on measurements below the crossover temperature. We now turn our attention to the behavior of the MR across the crossover temperature. The transport in this regime has both surface and bulk contributions, the latter of which is determined by activated transport across the bulk gap. The opening of this bandgap has been the subject of numerous studies [29, 32, 73] as researchers seek to understand the mechanism responsible for gap formation due to strong correlation interactions.

As mentioned in Chapter I, two distinct experimental values of the bandgap have been reported. Spectroscopic measurements, especially Photoemission Spectroscopy (PES), report an (optical) bandgap that opens around 40 K and widens to between 14 and 25 meV at temperatures below 10 K. One ARPES study [29] reports a detailed temperature evolution in which the conduction band shifts down across the Fermi energy as the temperature is raised above 50 K. Meanwhile, transport measurements [2, 16, 34, 72] yield a tiny bandgap between 2 and 4 meV at temperatures between 5 and 20 K. Possible explanations for the difference between these values include an indirect-bandgap scenario or the presence of in-gap states pinning the Fermi energy a few meV below the conduction band [34]. Although ARPES has revealed the presence of in-gap states, the energy resolution in these experiments is not sufficient to discern the nature of these states within such a tiny gap. If they are surface states however, they cannot account for the pinning of the Fermi level in bulk crystals or provide carriers for the thermally activated bulk transport.

One regime that is inaccessible to ARPES studies is that of high magnetic fields.

Understanding how the bandgap evolves with magnetic field can give insight to the mechanism driving the gap formation in the first place. The historical benchmark transport study of SmB_6 by Cooley *et al.* [73] observed strong negative MR at 4 K in a pulsed field up to 60 T. In an explosive-flux measurement in the same study up to 142 T, the resistance reaches 1.5% of its zero-field value around 86 T, after which the sample shows strong quadratic positive MR. These researchers, unaware of the onset of surface-dominated conduction at this temperature, attributed the negative MR and its minimum to the closure of the bulk bandgap around 86 T. More recently, a systematic temperature-dependent MR study [131] also reached a similar conclusion. Unfortunately, this study does not provide much detail or explanation on the MR below 5 K, which we now know to be dominated by surface conduction.

Motivated by this knowledge and a desire to separate the bulk MR behavior from the surface MR behavior observed [75], we conducted temperature-dependent transport measurements up to 60 T from 1.4 K to 4.0 K. The temperature dependence provides a quantitative measure of the transport bandgap's dependence on the magnetic field, while clearly distinguishing it from the behavior of the surface states. According to these measurements, the strong negative MR observed by Cooley *et al.* is indeed due to the closure of the bulk transport bandgap, and is distinct from the smaller negative MR displayed by the surface states at even lower temperatures ($<$2 K), as reported by older [132] and more recent studies [75, 100, 101].

4.5.2 Experimental Methods

For this experiment, resistance measurements were performed on a Corbino disk fabricated as described in Section 4.4.1 using the aluminum oxide (Al_2O_3) slurry and wedge wirebonding. The Corbino disk's resistance was measured in one of the NHMFL's 65 T short pulse magnets using a standard resistance bridge for R versus T and high-frequency AC lock-in techniques for R versus B. The short duration of

the magnetic pulse requires lock-in oscillator frequencies in the range of 200 kHz (the data acquisition rate is about 100 times faster), which leads to a significant amount of capacitance in the measured signal. Some degree of capacitance is tolerable, since the phase information is captured by the lock-in; however, this is the limiting constraint for the maximum oscillator frequency. A detailed transmission line analysis used for converting the measured signal to the actual sample resistance is included in Appendix C.

The sample was immersed in liquid ^{4}He at various pressures to obtain stable temperatures between approximately 1.5 and 4 K. At each temperature, a series of magnetic field pulses with incrementally larger maximum fields (and thus larger $\mathrm{d}B/\mathrm{d}t$) was used to obtain traces of resistance versus field, and to verify that $\mathrm{d}B/\mathrm{d}t$ effects (such as heating and inductive pickup) were not significant, as can be seen in Figure 4.15. The timing and duration of each pulse is approximately the same, so the peak field value is proportional to $\mathrm{d}B/\mathrm{d}t$ for each shot. In Figure 4.15, each shot shows a decrease in the resistance as the field increases, while the resistance increases as the field decreases. This is in contrast to heating effects, which depend only on the amplitude of $\mathrm{d}B/\mathrm{d}t$, not its direction. However, the hysteresis in the traces can be attributed to heating. Because the pulse is not symmetric in time, $\mathrm{d}B/\mathrm{d}t$ is largest at the onset of the pulse; thus, the strongest heating occurs during the beginning of the sweep up, resulting in a small reduction in the resistance during this time. This reduction is proportional to $\mathrm{d}B/\mathrm{d}t$ for each pulse, becoming successively larger as the peak field is increased. In contrast, the down-sweep after the peak field value is characterized by a small $\mathrm{d}B/\mathrm{d}t$ (less heating) and longer duration (more time for the system to cool the sample surface). In Figure 4.15, the down-traces for all the pulses overlap, which indicates that the heating is not a significant factor during the down-sweeps. The down-traces obtained from the 60 T pulses are shown in Figure 4.17 (a).

Additional data was taken using pulses up to 95 T at 1.4 K in the NHMFL's

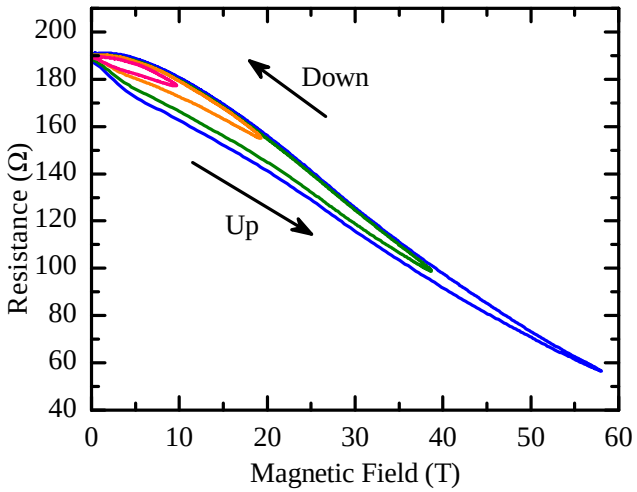

Figure 4.15: Magnetoresistance at 4 K for several magnetic pulse amplitudes.

100 T pulsed magnet using the same cryo-insert (Figure 4.16); this trace faithfully reproduces the 60 T trace at 1.54 K. The time profile of the magnetic field in this magnet is much more symmetric. It consists of a (relatively) slow ramping of the outer magnet up to fields around 40 T, at which point a charged capacitor bank is discharged across a magnet insert similar to the 65 T magnet, achieving total fields up to 100 T. After the inner magnet has discharged the bank, the outer magnet is ramped back down. In the data shown in Figure 4.16, the heating effects are not as significant, presumably due to the flat R-versus-T profile at 1.4 K; however, mechanical noise introduced by the strong $\mathrm{d}B/\mathrm{d}t$ when the magnet insert fires at 40 T is especially apparent in the up-trace. For analysis, the down-trace is again superior. This data, together with the 60 T trace at 3.96 K, is plotted as normalized magnetoresistance with Cooley *et al.*'s data in Figure 4.17 (b).

4.5.3 Discussion

A few features of the data are immediately apparent. As the temperature is reduced, the zero-field value increases, then plateaus, as has been observed in virtually every DC resistance measurement of SmB_6. The trace taken at 3.96 K is a reasonably

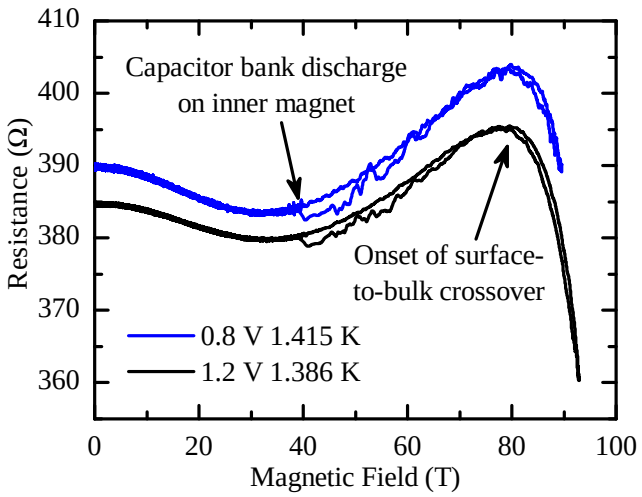

Figure 4.16: Magnetoresistance at 1.4 K for two 100 T magnet pulses. The two traces were taken using different excitation voltages, and at slightly different temperatures. The onset of the bulk conduction can be seen at 80 T. The capacitor bank discharge occurs around 40 T.

faithful reproduction of the data taken by Cooley *et al.* at 4 K using the NHMFL 65 T pulsed magnet (Figure 4.17 (b)) [73]. At lower temperatures, the "shoulder" associated with the crossover shifts to higher field values. At 1.54 K (Figure 4.17 (a)), no shoulder is discernible up to 60 T. In fact, at 1.39 K (Figure 4.17 (b)), the shoulder does not begin to appear until about 90 T. The traces taken at 2.51 K and below (Figure 4.17 (a)) all lie together at low fields, and branch away from the lowest temperature trace at sequentially higher fields as the temperature is reduced. This indicates that the surface state is largely independent of temperature at this scale, and that its behavior is mostly independent of the bulk transport behavior over these temperatures. This picture is not so clear from prior MR reports [73, 131, 132], especially since those MR traces are plotted in a normalized fashion. The data reported here around 1.5 K differ slightly across multiple samples and from previous data taken at the same temperatures [75, 132], perhaps due to the Corbino disk geometry and variations in surface quality. Still, in all the reports considered here, the surface state MR is very small (up to 15%) compared to the 4 K bulk MR. Finally,

the author notes that the 1.39 K trace up to 95 T does not show any signs of SdH oscillations, though this is not surprising, considering the surface mobilities reported for similar samples [75, 99].

The data in Figure 4.17 (a) is replotted as resistance versus temperature in Figure 4.18 by taking slices of the data at selected magnetic fields. This format visualizes the evolution of the resistance rise and plateau with the magnetic field strength. The crossover shoulder moves to lower temperatures as the magnetic field is increased.

The temperature dependence can be used to estimate the size of the bulk transport gap at various magnetic fields. The total resistance is modeled as the parallel combination of the surface resistance and an activated bulk resistance:

$$R(B,T) = \left(\frac{1}{R_s(B)} + \frac{1}{R_0(B)} e^{\frac{\Delta(B)}{k_B T}} \right)^{-1}$$

where $R_s(B)$ is the surface resistance taken from the trace at 1.54 K, and $R_0(B)$ and $\Delta(B)$ (the bandgap) are fitting parameters. The contribution from the surface resistance is subtracted off, and the remaining bulk contribution

$$R_b(B,T) = \left(\frac{1}{R(B,T)} - \frac{1}{R_s(B)} \right)^{-1}$$

is plotted as an Arrhenius plot. Linear fits of this plot for each magnetic field value, weighted by the relative contribution of the bulk portion to the total resistance $\frac{\partial \ln(R_b)}{\partial R}$, provide an activation energy with uncertainty estimated by the (weighted) fit residuals. Figure 4.19 shows the best-fit activation energy versus magnetic field, with the uncertainty of $\Delta(B)$ indicated by the gray error bars. The inset depicts an example fit at 29 T, plotted with the raw resistance and the calculated bulk resistance with error bars. The bandgap closes with the magnetic field to about 50% of its zero-field value at 58 T. Although there is not temperature-dependent data at higher fields, the onset of the crossover shoulder around 90 T at 1.39 K suggests that the closure con-

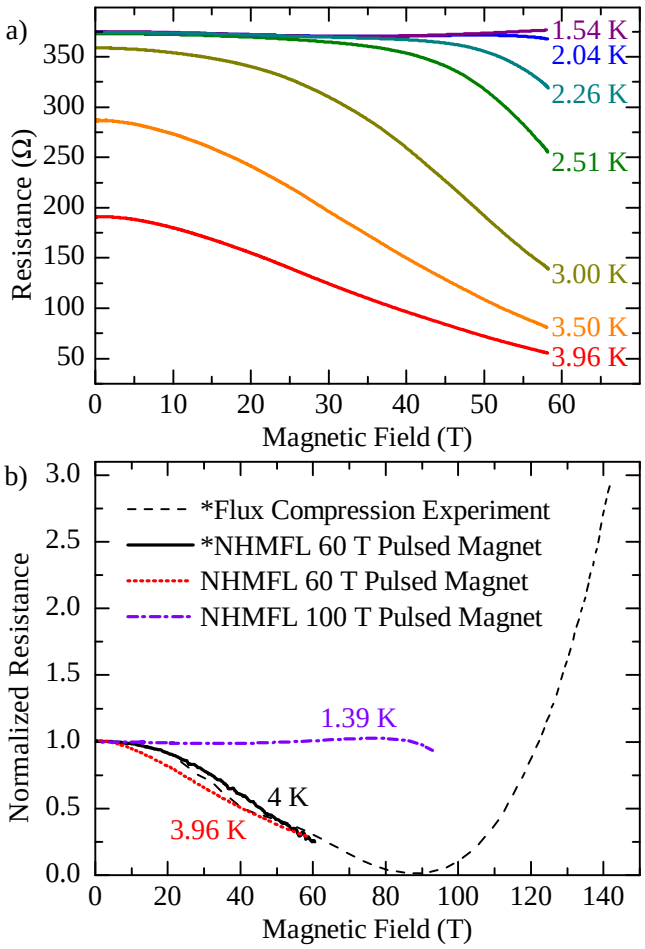

Figure 4.17: Magnetoresistance across the crossover temperature range. (a) Traces of the Corbino disk two-terminal resistance as a function of magnetic field at various temperatures between 1.54 and 3.96 K. (b) Traces of the Corbino disk two-terminal normalized resistance at 1.39 K and 3.96 K, plotted together with Cooley *et al.*'s data. Cooley *et al.*'s data is denoted by asterisks in the legend.

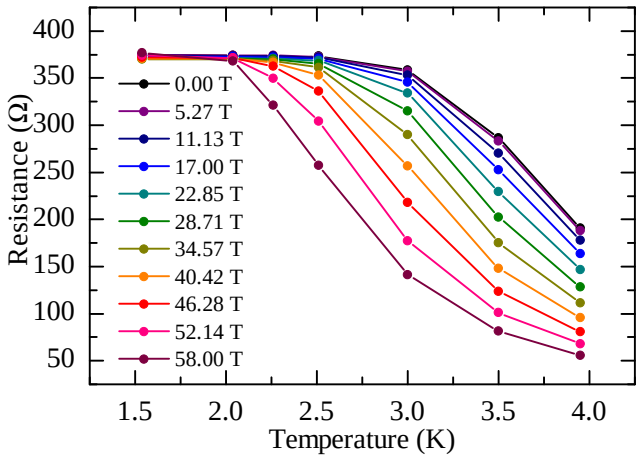

Figure 4.18: Plots of the Corbino disk two-terminal resistance versus temperature for select values of the magnetic field.

tinues to be approximately linear, reaching roughly 10 K at 93 T. Extrapolating the value of the gap closure is speculative at best, but such a linear trend suggests that the gap closes around 120 T. This data has some qualitative agreement with prior reports [133] of field-induced gap closure. In any case, the finite resistance of the 93 T trace at 1.39 K alone is sufficient to reveal that the minimum at 86 T of Cooley *et al.*'s 4 K flux compression data does not correspond to a fully closed gap. The present measurements at this temperature are not at large enough fields to observe the positive MR in Cooley *et al.*'s data above 86 T.

The gap seems to close in a nonlinear fashion, in qualitative agreement with Cooley *et al.*'s data. Arguments for this qualitative behavior have been speculated elsewhere [73, 131], but no descriptive models have been suggested. The identification by ARPES [29] of the X point of the conduction band as the band edge responsible for the small transport bandgap in this temperature range implies that the conduction band edge is driven toward the Fermi energy (or vice versa) under the influence of the magnetic field. Two mechanisms may be involved—Zeeman splitting of the Sm^{3+} state and a second-order Zeeman shift of the Sm^{2+} state. Alongside the activation energy plotted in Figure 4.19, the simulated behavior of the extracted activation

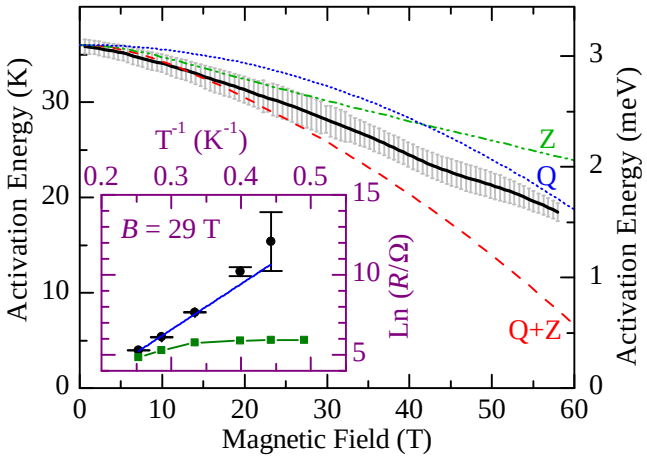

Figure 4.19: Calculated transport activation energy as a function of magnetic field. Error bars correspond to fit residuals. Theoretical fits are also plotted for the Zeeman second-order shift, Zeeman splitting, and shift + splitting (blue dotted, green dash-dotted, and red dashed, respectively). INSET: Example weighted fit (blue line) at 29 T of the calculated bulk resistance data (black dots with error bars) on an Arrhenius plot. The raw resistance is also plotted (green squares) for reference.

energy is plotted for Zeeman splitting (Z) with a Landé g-factor of 0.6 [134–136], for a second-order Zeeman shift (Q) of 1.0 Hz/G^2 [137], and for the combination of these two effects (Q + Z), which might be expected for the quasiparticle transition between Sm^{2+} and Sm^{3+} states. The data does not fit any of these models particularly well, especially the combined model which predicts the full closure of the gap around 74 T. These models assume, however, that the Fermi energy itself does not shift with magnetic field, which is a possibility suggested by the MR measurements of a shift in the surface states' carrier densities in Section 4.4.2 [75]. Also, there may be an additional second-order Zeeman shift associated with the Sm^{3+} state, which unfortunately cannot be extracted from the linear splitting at the low fields used so far to determine g. Meanwhile, the relation of the gap closure to that observed with increasing pressure [32] is unknown; however, there is no sign in existing MR data of a sudden collapse of the bandgap, as is reported for pressures around 50 kbar.

4.5.4 Summary and Outlook

In this section, the temperature-dependent MR in the crossover regime has been studied, and the behavior of the transport gap has been extracted for magnetic fields up to 60 T. The results are qualitatively consistent with prior studies of the gap closure and high-B transport, but provide a more detailed evolution of the gap closure with magnetic field. This may be useful in unraveling the mystery of the nature of the transport gap, with respect to the whole electronic structure, and the mechanisms responsible for it. The MR associated with the reduction of the gap is physically distinct from the negative MR of the surface states discussed in Section 4.4, though transport measurements at the crossover temperature can be influenced by both. Additionally, measurements were taken at 1.4 K up to 95 T, but these show no signs of SdH oscillations. Achieving higher-field measurements of the surface states is constrained by two factors. Firstly, the gap reduction makes it increasingly difficult to measure the surface states without bulk conduction as the magnetic field is raised; evading this requires measurements at lower temperatures, but a hard limit is imposed by the field value of the gap closure. Secondly, there are significant technological challenges to achieving higher field values and the lower temperatures required for these types of measurements. Very small samples are needed to fit inside a double-walled ^{3}He cryostat for sub-Kelvin temperatures, and the cooling power of liquid ^{3}He may not be sufficient against the increasingly large eddy-current heating at higher and higher $\mathrm{d}B/\mathrm{d}t$. The current state-of-the-art multi-shot magnet technology is also limited to just above 100 T and becomes prohibitively expensive to operate. For these reasons, any future observations of SdH oscillations must come from surfaces with improved carrier mobility.

CHAPTER V

SmB_6 Surface Morphology

5.1 Introduction

TIs have the singular distinction of being electronic insulators while harboring metallic, conductive surfaces. In ordinary materials, defects such as cracks and deformations impede electrical conduction, making the material more electrically resistive. Peculiarly, 3D TIs should become *better* conductors when they are cracked because the cracks themselves, which act as conductive topological surfaces, provide additional paths for the electrical current. Significantly, for a TI material, *any* surface or extended defect [138] harbors such conduction. In this chapter (available as a preprint elsewhere [139]), it is shown that small subsurface cracks formed within SmB_6 via systematic scratching or sanding result in such an increase in the electrical conduction. In fact, the results indicate that such conduction can be the dominant transport. SmB_6 is in a unique position among TIs to exhibit this effect because its single-crystals are thick enough to harbor cracks, and because it remarkably does not appear to suffer from conduction through bulk impurities [72, 77]. This is in contrast to the known weakly correlated TIs, which are grown as ultra-thin films in an effort to minimize bulk impurity conduction. The results of this study not only strengthen the building case [29, 72, 77, 96–98, 110, 140–142] for SmB_6's topological nature, but are relevant to all TIs with cracks, including TI films with grain boundaries.

These results also have serious implications for researchers working on surface transport studies of SmB_6 [72, 75, 77, 99–101, 143, 144]. In fact, this work was motivated by some of the puzzling results of such studies. For example, several transport studies, including the one in Section 4.2 [72], obtained carrier densities beyond the limit of 5.85×10^{14} cm^{-2} imposed on a single-band 2D system by the BZ size calculated for the lattice constant of SmB_6 [1]. Reinterpretation of some historical transport studies [16, 32] in a 2D context also results in carrier densities which exceed this k_F limit.

As discussed in Section 4.3, this discrepancy is due in part to measurement difficulties unique to 3D TI bulk crystals, notably the possibility of conduction along unprepared side surfaces of a thinned sample with polished top and bottom surfaces. This problem was evaded using a Corbino disk geometry [75], which is sensitive only to conduction along a single prepared surface. The polished surfaces on which the disks were fabricated yielded conductivities that were an order of magnitude smaller than indicated by a conventional Hall bar sample. While the corresponding carrier densities in our and others' [99] Corbino disks were thereby rendered more physically reasonable, the surprising trend that was observed across our samples was that better polishing counterintuitively acted to diminish the surface conductivity. This result is not completely new; this trend had been observed in "pre-TI" transport [34], though the trend evaded understanding at the time. More recently, a similar trend has been observed on ion-damaged surfaces, for which the conductivity increases linearly with the depth of ion damage [145].

The motivating hypothesis for the current study is that the increase in conductivity with lower surface quality is due to cracks along the surface of the material. Surface roughening alone is not necessarily expected to change the 2D "sheet" carrier density (though it might decrease the carrier mobility), but any additional surfaces due to cracks along the visible top surface would contribute to the measured conduc-

tivity, as is the case with any 3D TI with no bulk conduction. Because such cracks would reside below the surface, they would not ordinarily be visible, but they would contribute to the total transport as an apparent increase in the sheet carrier density and as a corresponding reduction of the measured Hall coefficient.

5.2 Scratch Experiment

To test the hypothesis of increased conductivity due to cracks near the surface, the low-temperature resistance plateau was studied over a series of measurements on two Corbino disks fabricated on a single surface of SmB_6, shown in Figure 5.1 (a). The sample used in this study was the same sample used for (011) MR measurements in Chapter IV. The Corbino disks' resistances were measured in a variable-temperature cryostat between 1.5 K and 4 K using standard lock-in techniques with an AC current of 5 µA at a frequency of 17.72 Hz. After the temperature dependence of the resistances was obtained, the Corbino disks were brought to room temperature, and one was scratched between the inner and outer contacts in a radial direction using a diamond-tip scriber (Figure 5.1 (b)). The disks were cooled and measured again, warmed and scratched a second time (Figure 5.1 (c)), then cooled and measured a final time. The additional silver paint surrounding the disk in Figure 5.1 (c) was added to ensure electrical continuity with the outer Ti/Au contact pad. SEM images taken after the second scratch are shown in Figure 5.1 (d – f). Resistance curves obtained after each scratch are plotted together for both Corbino disks in Figure 5.1 (g).

The plateau below 3 K, which corresponds to the resistance of the surface, decreases substantially after each successive scratch. Meanwhile, the second unscratched Corbino disk nearby on the same surface exhibits no change in each successive measurement. A portion of the outer disk contact near the scratch was accidentally removed during the scratching, as seen in Figure 5.1 (b). Nevertheless, the resistance decrease in the Corbino disk is opposite the change expected due to this damage, but

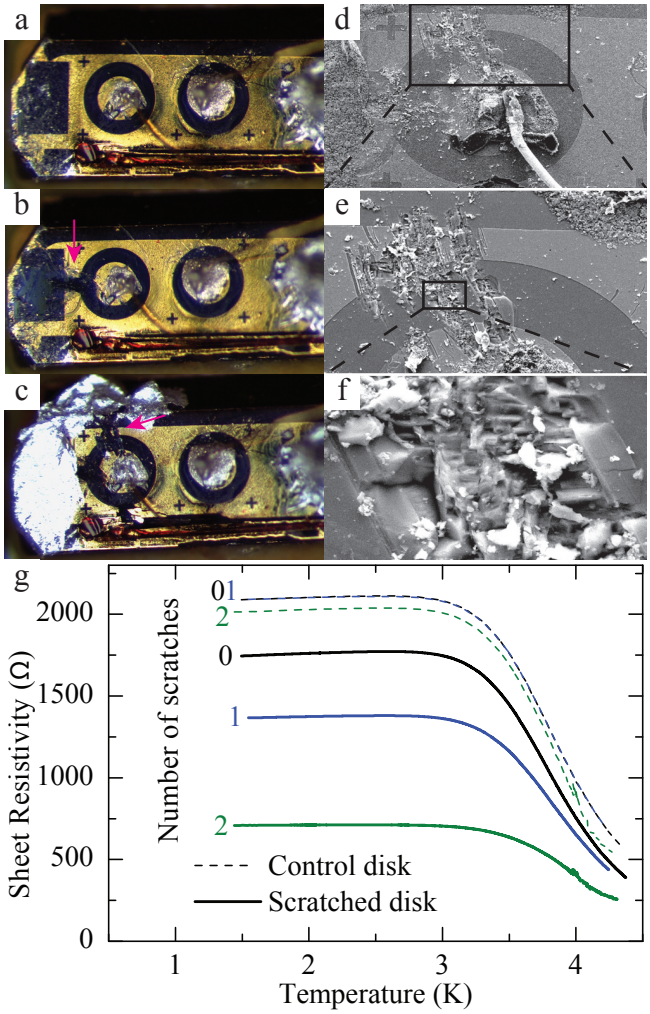

Figure 5.1: Scratched Corbino disk measurements. (a – c) Optical images of the two Corbino disks before scratching and after each scratch. The scratches are indicated with magenta arrows. (d – f) SEM images of the second scratch shown in (c) at increasing magnification. (g) Resistance versus temperature curves of both disks before scratching and after each scratch. Thick solid lines indicate the scratched disk, while thin dotted lines indicate the unscratched (control) disk.

is consistent with the hypothesis that additional surface cracks could contribute to the total conduction. The magnitude of the change is also much larger than what is expected due to surface roughening, given that the scratched area is only a very small portion of the entire disk; such a large change suggests the presence of additional unseen conduction paths below the visible surface.

Motivated by this result, ion-beam milling was performed on the scratched Corbino disk surface to reveal cross sections of the scratch profile. Indeed, subsurface cracks are apparent below scratched portions of the disk, as shown in Figure 5.2 (a – f). For example, the groove shown in Figure 5.2 (a) is about 3 µm wide and less than 0.5 µm deep, but harbors subsurface cracks several µm long in the transverse direction and up to 100 nm wide. Cracks shown in Figure 5.2 (e) are visible both on and below the surface. Because the bulk transport behavior is unchanged by the scratches, and because the increased surface area due to surface roughening is not sufficient to explain the magnitude of the change in resistance observed, the natural conclusion is that these cracks must be responsible for the additional conduction. Whether these cracks are oxidized when exposed to ambient air, as occurs for the outer surfaces [113, 114], is presently unknown; nevertheless, it is expected that the transport properties of the cracks can be very different from those of the outer surface.

Subsurface cracks were also observed on a separate SmB_6 crystal prepared by rough-polishing (P1200 grit, which produces $\sim$1 µm surface roughness), as shown in Figure 5.2 (g – h). The cracks visible in Figure 5.2 (h) are up to 1 µm long in the transverse or vertical direction, though they are much narrower than those seen in Figure 5.2 (b) and (d), approaching the focal resolution limit of the SEM. Although cracks produced at finer polishing levels are below the resolution of the SEM images, it is not unreasonable to hypothesize their existence and contribution to the total surface conduction. Such cracks are expected to form whenever the maximum contact stress, which actually does occur a few µm below the surface [146], exceeds the tensile

strength of the material.

5.3 Implications of Subsurface Cracks

The most important implication of this observation is that any transport study on surface conductors such as 3D TIs with an insulating bulk must account for the possibility of cracks such as these, especially since such cracks may have different transport parameter values than the outer surface. In particular, this result provides a way to account for the reduced conductivity in SmB_6 as surface quality is improved, as well as the extraordinarily high apparent conductivity and unphysically large carrier density (small Hall coefficient) in the Hall bar measurements. This situation might be exacerbated if such cracks make electrical contact with hidden Al inclusions in flux-grown samples that would otherwise be insulated from the surface transport. However, the complications presented by the possibility of cracks extends also to crystals grown via the floating-zone melting process.

This result also has ramifications for pressure-dependent studies, during which the samples are known to fracture [91]. In this scenario, the conductance of the sample will increase if the sample fractures under pressure, which would lead to a lowering of the plateau value in both resistivity and Hall measurements. It is not clear whether this is a significant effect in previous pressure studies of SmB_6 [32], especially since the shift in transport values appears to happen smoothly, rather than discontinuously, as might be expected from fracturing, and since Cooley *et al.*'s data is similar to subsequent pressure-dependent studies [147, 148].

It is possible that the transport parameters reported in Chapter IV and elsewhere [75] are also affected by subsurface conduction. Since current might flow along cracks that are not orthogonal with the z direction, it is possible that the estimates of the mobility based on the $\cos\theta$ fits are too low, resulting in an overestimation of the carrier density. The latter is also likely due to the real conductive surface area being

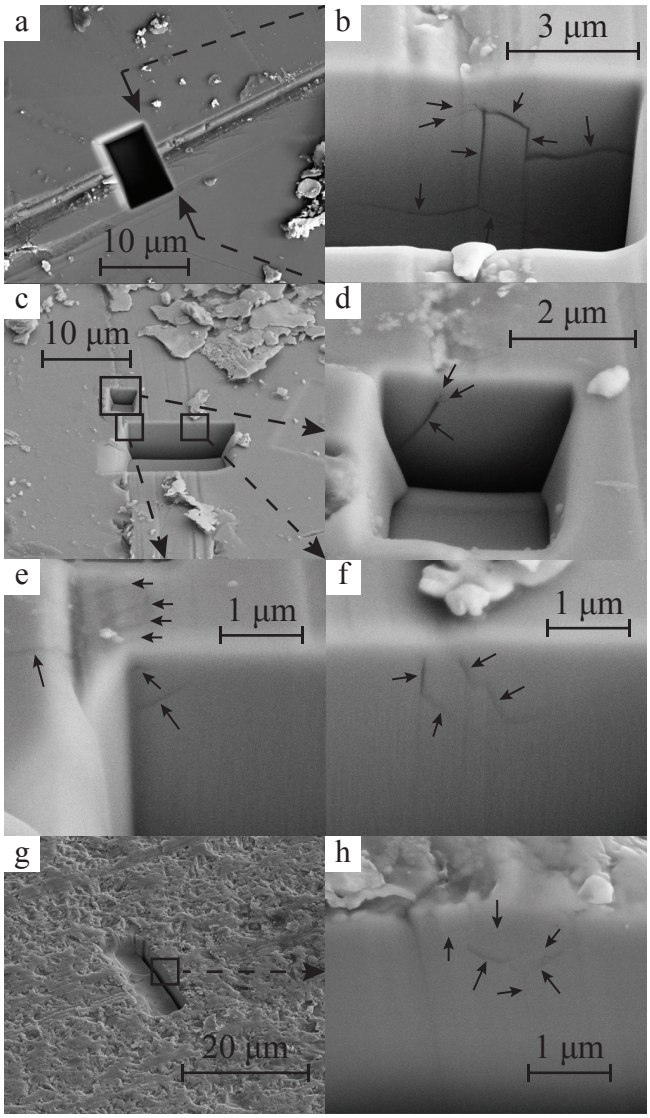

Figure 5.2: Ion-milled cross sections of scratches. (a) Ion-milled cross section across a scratch. (b) Subsurface cracks visible below the scratch in (a). (c) Ion-milled cross sections across another scratch. (d – f) Subsurface cracks visible below the scratch in (c). (g) Ion-milled cross section on a rough-polished surface. (h) Subsurface cracks visible below the rough surface in (g). In all panels, small black arrows indicate cracks.

larger than the "ideal" area used in the Corbino disk calculations.

Finally, a big-picture observation from this result is that the increased conductance is evidence for the topological nature of SmB_6. Indeed, 3D TIs are the only known class of material that demand metallic surface conduction. It follows naturally that an increase in conductance resulting from the additional surfaces provided by surface roughening and surface/subsurface cracks points to the existence of such special metallic surfaces, whose origin is the topology of the 3D bulk material. Although surface conduction via other exotic mechanisms cannot technically be completely ruled out, the TI nature of SmB_6 is the most probable and logical origin of this effect.

CHAPTER VI

Summary and Outlook

6.1 Introduction

In this chapter, Section 6.2 provides a summary of the work presented in this thesis, Section 6.3 provides a listing of other types of work done on SmB_6, and Section 6.4 provides an evaluation of the current problems most relevant to SmB_6 transport properties, including an outlook for device engineering. Section 6.5 discusses some possible directions for future transport work on SmB_6.

6.2 Summary of the Thesis Work

In this work, SmB_6 has been studied in the context of TI theory, primarily via transport measurements. In Chapter I, the puzzle regarding the physical origin of the resistivity plateau at temperatures below around 4 K was presented. The metallic nature and the magnitude of the resistivity plateau defied explanation by known bulk conduction mechanisms, including impurity conduction (which, in SmB_6, would typically violate the Mott impurity limit), and intrinsic bulk conduction (which would violate the unitarity scattering limit in SmB_6). Some experiments showed that the value of the plateau depended on surface treatments, but it was difficult to explain the robustness of the plateau against all attempts to remove it. The plateau was also

linked to bulk stoichiometry, so the mystery was how a feature intrinsically dependent on the bulk could also be a robust surface effect. A theoretical explanation [70] for the plateau was then discussed in Chapter II, in which the plateau arises from surface conduction due to topologically protected surface states characteristic of time-reversal-invariant TIs. This scenario nicely accounts for the robustness of the surface states and their connection with the bulk, while still allowing for variations in the resistivity with surface quality.

In Chapter III, the plateau was shown to be due entirely to surface conduction, with a fully insulating bulk at temperatures below the shoulder of the plateau. This was accomplished by using a novel contact geometry with contacts in the middle of the flat faces of a thinned piece of single-crystal SmB_6. Variations in the measured four-terminal resistance across different current/voltage contact configurations revealed a dramatic change in the current path from bulk-dominated to surface-dominated conduction as the temperature was lowered into the range of the plateau. The size of the shift indicates that below this crossover temperature, the bulk conduction becomes a negligible portion of the transport. This result was also confirmed independently by other researchers using a wedge-shaped sample [77]. It is remarkable in that SmB_6 was the first known 3D TI to have a fully insulating bulk, which is an important property for transport studies of or device engineering involving TI surface states.

The MR of SmB_6 was studied in Chapter IV. A number of concerns regarding the transport geometry of non-local measurements on TI surface states were addressed by utilizing a Corbino disk structure fabricated on single surfaces of SmB_6. The samples studied exhibited negative MR in the surface states. Angle-dependent measurements up to 35 T yielded surface mobilities around 120 $cm^2/(V \cdot s)$ and carrier densities around 10^{14} cm^{-2}. They also revealed that the MR was primarily due to changes in the carrier density of the surface, but were accompanied by smaller changes in the carrier mobility that are consistent with Kondo scattering. At lower fields, a dynamic

hysteretic behavior that depends on the field sweep rate and the temperature can be seen in two distinct field regimes. All of the samples studied exhibit a hysteretic dip in the resistivity below 0.1 T, while some exhibit an additional dip that extends up to several T. The origin of these dips is unknown, but extrinsic effects such as a glassy spin texture of Sm_2O_3 on the surface or the magnetocaloric effect from an unidentified source are likely responsible.

The MR of the bulk conduction near the crossover temperature was also addressed using measurements from the NHMFL pulsed magnet facility up to 60 T. These measurements show a very strong negative MR consistent with previous studies [73], but also detail the evolution of the negative MR across the entire crossover range from a bulk MR to a distinct surface MR independent of the bulk MR. The temperature dependence of the bulk MR allows the activation energy (transport bandgap) of the bulk carriers to be extracted as a function of the magnetic field, and reveals a closure of the gap between the Fermi energy and the conduction band. The closure is stronger than that expected from the Zeeman splitting of the Sm^{3+} state or the Zeeman shift of the Sm^{2+} state, but weaker than the two combined. Meanwhile, the surface conduction, which was probed up to 92 T in the NHMFL pulsed 100 T magnet, shows no hints of SdH oscillations.

In Chapter V, an additional geometric complication for transport measurements was addressed. In any robust surface conductor, current should flow not only on the exterior crystal surface, but also along interior surfaces and channels resulting from cracks and other crystal dislocations. Mechanically abrasive surface treatments such as polishing [34] or ion damaging [145] lead to higher conductances in SmB_6. An experiment in which a Corbino disk structure is scratched also reveals a dramatic increase in conductance. Ion-milled cross sections of the scratched region reveal sub-surface cracks, which not only provide additional "surfaces" for the current to flow, but may also vary in quality from the exterior surface. Similar cracks were found

below a rough-polished surface, indicating that this additional conduction may be present on any surface treated using such abrasive techniques.

6.3 Summary of other work on SmB_6

SmB_6 has been the subject of too many studies to list each one, but include Mössbauer spectroscopy [4–6]; transport [2, 9, 11, 16, 32–34, 72, 73, 75, 77, 99–101, 131–133, 139, 143, 144, 149, 150], dHvA [96, 151], and magnetic susceptibility measurements [2, 152]; nuclear magnetic resonance (NMR) [152–161], electron paramagnetic resonance [27, 162, 163], and electron spin resonance [28, 164, 165]; point-contact tunneling spectroscopy [20, 21, 166, 167] and STS [140, 168, 169]; PES [170–172], ARPES [29, 36–39, 97, 98, 106–109, 173], SARPES [110], and X-ray absorption spectroscopy [174] (including HAXPES [113, 114]); X-ray scattering [1] and neutron scattering [1, 142]; optical spectroscopy [11, 19, 35, 175]; high-pressure measurements [32, 147–149, 159, 160, 176, 177]; surface ion-scattering [178], ion-damage [145], and radiation-damage [20] studies; and mechanical studies [3]. Some studies have made use of intentional rare-earth dopants [141, 156, 161, 179] or vacancies [12] for comparison. Many of these experiments have been discussed in more detail in Chapter I, particularly the Mössbauer spectroscopy, pre-2010 transport, and early high-pressure transport. As discussed in Section 4.5.1, the results from a large number of the spectroscopy studies can be consistently encapsulated by positing the existence of a $\sim$15 – 20 meV gap that arises from hybridized f and d states, along with a $\sim$15 – 20 meV activation energy between E_{F} and the conduction band edge, the latter of which is corroborated by the transport studies. The pre-2010 transport studies themselves share a large number of consistent features, but the behavior of the resistivity below 5 K has to be reanalyzed, reinterpreted, or perhaps performed again with surface conduction in mind, as discussed in Sections 4.2 and 5.3.

Since 2011, the majority of studies have been focused on understanding the SmB_6

surface state(s). This has been done primarily by means of transport and dHvA measurements, and of ARPES and STS, largely due to their sensitivity to the surface properties of materials. The conclusions drawn from these studies answer some of the questions surrounding the surface states (*e. g.*, their 2D nature), but give disparate or even contradictory results regarding basic properties of these states (*e. g.*, effective mass, topological nature, *etc.*). These studies and the issues that arise from them are discussed in Section 6.4.

6.4 Current Issues

Although the TKI theory for SmB_6 and the verification that the plateau was fully due to surface states resolved the most outstanding mystery surrounding SmB_6 before 2010, these breakthroughs have led to a number of additional puzzles that must be solved before basic properties of the system can be understood. One of the key experimental questions that has not been resolved is the topological nature of SmB_6 and the fundamental origin of its surface states.

As discussed in Section 2.2, the topological nature of conventional semiconducting TI systems has been confirmed primarily with ARPES. In these systems, a band inversion can be calculated from a single-particle theory and compared to the band structure measured by ARPES. The surface states are also directly observed by ARPES, which clearly shows the surfaces' Dirac-like structure. Additional measurements using spin-resolved techniques (SARPES) reveal the helical spin structure of the surface Dirac cones. These measurements, taken together with the observation of SdH oscillations of the 2D surface states, are sufficient evidence for the topological nature of these materials. Unfortunately, the dispersive structure of some of the in-gap states seen in SmB_6 has been very difficult to observe via ARPES (and especially SARPES) because the bandgap is so tiny. Large electron pockets have been measured at the X point by many studies, and the k_z dependence of these pockets

confirms their 2D surface nature [29, 97, 98, 107, 173]. However, some studies claim to see a Dirac-like dispersion at the Γ point, indicative of the TI surface state [97, 98, 107], while others claim to see parabolic dispersion with Rashba splitting at the Γ point [173], which excludes a topological origin for the surface states. One study attempts to resolve the spin structure indirectly using circular dichroism [98]; the data shows chirality of the orbital angular momentum of the in-gap states, suggesting (but not confirming) a helical spin structure. Another SARPES study claims to observe a spin-polarized signal originating from the helical spin dispersion [110]. The limited resolution of ARPES and the disagreement among the studies conducted so far regarding the Γ point has presented a need for alternative methods for confirming the topological nature of SmB_6. Meanwhile, other crystallographic surfaces, such as the (011) and (111) families, have yet to be studied.

Another way of probing the nature of the Fermi surface is through dHvA measurements. In one 2014 study [96], quantum oscillations were measured from 5 to 45 T. Several oscillation frequencies were observed, corresponding to multiple carrier pockets. The angle dependence of these frequencies indicated that they were 2D pockets, with two aligned with the (001) surface family (presumably associated with the X and Γ points), and one aligned with the (011) surface family. A Landau index plot of the oscillation maxima and minima indicate a Dirac-like structure with no spin-degeneracy—a TI surface state. While this makes a strong case for the topological nature of SmB_6, the mystery remains how the oscillation signal is so clear, but completely absent in transport measurements (SdH oscillations) up to at least 92 T. Conversely, the absence of the SdH signal is not surprising, given the carrier mobility values of 0.012 T^{-1}; the question is then, how can these surfaces yield such a clean dHvA signal? One might speculate about the existence of inclusion surfaces, which are isolated from the exterior surface and may be much cleaner with higher mobilities. However, the situation became more complicated by a more recent dHvA study [151],

which observed oscillation frequencies with a bulk-like angular dependence (but not 2D surface pockets). This suggests the presence of bulk carriers, but paradoxically, transport measurements indicate a bulk insulator with surface conduction. How bulk Fermi-surface electrons can yield quantum oscillations while not contributing to non-local transport is not understood. How these two disparate dHvA measurements and the transport measurements can be reconciled is still a mystery, and may require appealing to more exotic models of the electronic structure.

Surface-transport measurements themselves are also somewhat dissimilar, which makes a consistent picture of the surface states difficult to realize. There is some variation in the MR reported across various samples. Some reports [100, 101] claim to observe WAL (expected in a TI surface state), while others [75] (including the present work) exclude it; limits on the WAL amplitude of the latter constrain the carrier effective mass to several times the bare electron mass, in contrast to the light mass extracted from dHvA measurements [96]. There has been some consensus on the carrier mobilities and densities, which are also consistent with values obtained from ARPES (though quite different from those obtained from dHvA oscillations), and no transport measurement has yet observed SdH oscillations. The low-field behavior of the MR shows a wide range of variation among the available reports, including ferromagnetic domain ordering [100], glassy spin ordering (present work) [75], and Kondo scattering (present work) [75].

A number of the factors that may play a role in these variations, which have been discussed in Chapters IV and V, include current flowing on multiple sample surfaces, surface and subsurface cracks, variations in surface treatments such as polishing and etching, and notably the presence of Sm_2O_3 on samples exposed to air. Variations in the surface morphology and the density of surface magnetic impurities have been largely uncontrolled, and may account for the wide range of behaviors exhibited by the material. Variations in crystal-growth methods, types of impurities, and stoichiom-

etry may also contribute to the disparity of the observed behaviors. A number of proposed types of trivial surface states have been proposed in place of, or in addition to, the topological state, including polarity-driven states [109] ((001)-family surfaces only) and inversion-layer states [173] originating from band bending or surface reconstruction. However, the delicate surface chemistry required to support these types of states is not likely preserved where Sm_2O_3 is present and where the morphology may be quite poor. Thus, *a priori*, there is no reason to expect measurements done on cleaved surfaces in ultra-high vacuum to correspond to measurements done on samples prepared in ambient conditions. A more systematic method of sample growth and preparation will be necessary both for understanding the nature of the surface state(s) and for device fabrication.

Another problem arises when one attempts to associate the bulk transport gap with features seen in spectroscopic measurements. The bulk transport gap is inferred from the activated behavior of R versus T measurements, and is typically associated with the activation energy between E_F and the conduction band. However, the spectroscopic evidence for this picture is not clear; there are two issues at this point. First, multiple studies [29, 106] show the conduction band minimum around 9 meV above E_F (at 25 K), rather than the 3 meV above E_F seen by transport. Denlinger *et al.* [29] argue that theoretical predictions of the band dispersion around the X point might allow for it to dip to 3.5 meV away from the X point at the lowest temperatures; however, direct observation of this has not been possible at the relevant energy scale and temperature. Second, even if the 3.5 meV conduction band minimum is taken as a given, what is responsible for the pinning of E_F so close to the conduction band minimum? Such pinning so far from the middle of the gap is nearly impossible without the presence of some bulk in-gap states or impurity states. The valence band maximum, located at a BZ point that Denlinger *et al.* call "H," is around 14 meV below E_F. However, the bulk in-gap donor states required to pin E_F so far from the

middle of the gap are not observed in ARPES, and there is some disagreement about their presence in optical data [35, 175]. Meanwhile, in-gap surface states cannot pin E_{F}, and they simply cannot contribute enough electrons to the activated behavior.

An additional issue concerning the bandgap arises when comparing transport data with NMR data. In contrast to the behavior of the transport gap described in Section 4.5, NMR [158] indicates in-gap magnetic states (absent in ARPES) $\sim$30 K below the conduction band edge at zero magnetic field, but which shift up into the conduction band under a field of only 14 T, leaving the field-independent hybridization gap to determine the low-temperature dynamics of the system. If these states are responsible for the pinning of E_{F}, the single-particle picture for transport measurements should instead exhibit a collapse of the thermal activation energy under similar field values. This suggests that the physics of the E_{F} pinning and any associated in-gap states is determined rather by exotic many-particle interactions. A similar conclusion was reached by researchers comparing La-doped and undoped SmB_6 [161], based on the low-temperature magnetic field dependence of each.

While SmB_6 appears to be a ripe test bed for exotic many-body interactions within or without the context of TIs, the outlook for device engineering is challenged by a significant number of obstacles. First, although the bulk becomes truly insulating below 2.5 – 3 K, any device interfacing with the surface states will need to operate at these low temperatures. Second, the morphology of the surface is not suited to device fabrication. Bulk crystals do not cleave well in any direction. Although patches of single termination planes in the (001) family can be found in such a cleave, they are not large enough for fabricated structures [168, 169]. Pristine patches of (011) and (111) surfaces have not been achieved. Efforts in thin-film synthesis have achieved resistivity behavior similar to the bulk crystals, but the crystal quality is still quite poor [144]. Third, the formation of Sm_2O_3 magnetic impurities can disrupt the spin behavior of the TI surface electrons via spin-flip scattering; this is a challenge that

will need to be addressed with engineering controls such as *in-situ* device fabrication, surface passivation, or preparation in inert environments.

6.5 Future Transport Studies

From a transport perspective, it is desirable to achieve geometrically-controlled experiments on pristine SmB_6 surfaces. As discussed in Section 6.4, the majority of transport studies are done on surfaces which harbor Sm_2O_3 on the surface. Performing experiments on oxide-free surfaces is important for minimizing spin-flip scattering and achieving spin currents with higher mobilities. There are at least three approaches that can be taken to mitigate the formation of Sm_2O_3:

1. *In-situ* device measurement would eliminate all chances for exposure to oxygen. For bulk-growth crystals, this involves cleaving and measuring the crystal in the same vacuum system. For film-grown crystals, the growth and measurements would be performed in the same system. In both cases, fabrication of contacts for a particular measurement geometry would also need to be accomplished *in situ*. One possibility would be a four-contact probe with contacts spaced very close together, provided the working surface of the sample is much larger than the contact spacing. Another possibility is to evaporate a Corbino disk structure using a shadow mask, using probe contacts for electrical access. Of course, the entire structure would need to fit within the magnet bore for magnetic field measurements. Both of these methods would be subject to morphological problems arising from cleaving or the growth quality of the thin-film crystals.

2. Preparation in an inert environment could also prevent the formation of Sm_2O_3. This has the promise of greater flexibility in surface preparation, since the procedures can be performed at ambient pressure. For example, chemical etching or surface polishing could be performed in a glove box with a dry nitrogen or

noble gas environment. In principle, this would allow for better surface uniformity than can be achieved in vacuum systems, although it is unlikely that mechanical preparation would yield surfaces free from morphological defects such as cracks or dislocations. A way to transfer the samples to vacuum systems such as evaporators for device patterning or cryogenic magnet systems for measurements would need to be constructed in order to accomplish this.

3. The difficulties associated with transferring a sample among different vacuum systems might be relieved if the surface can be passivated, *e. g.*, with Al_2O_3. A significant challenge here would be designing electrical contacts that are able to access the passivated surface.

Transport measurements may also provide the evidence needed to confirm the helical spin structure of the surface states. The direct detection of spin currents via transport measurements would be compelling evidence for the topological nature of SmB_6. Detection of a spin current with the use of metal ferromagnetic tunnel-barrier potentiometers has been employed in spin–orbit-induced spin-current systems [180], and the ideas have been extended to spin detection in TI systems [57]. Such measurements have already been performed on the known TI Bi_2Se_3 [56]. In this experiment, a slab of Bi_2Se_3 was prepared with metal ferromagnetic tunnel-barrier contacts fabricated on top of the slab. When current is passed along the slab (using ordinary contacts), the spin–momentum locking results in a spin current with spin oriented in-plane, perpendicular to the current direction. The voltage on the ferromagnetic tunnel-barrier contacts is then determined by the projection of the spin on the ferromagnet's magnetization axis. This provides a way for the spin current to be distinguished from ordinary charge current by independently changing the current direction and the magnetization of the ferromagnetic elements. Specifically, the spin contribution to the voltage should flip sign when the current direction is reversed, and should follow the hysteresis loop of the ferromagnet as its magnetization is reversed.

Additionally, if the ferromagnetic elements are magnetized parallel to the charge current (perpendicular to the expected spin projection), the spin contribution to the voltage should be zero. The direction of the voltage also distinguishes the topological spin configuration from that of a Rashba-splitting effect.

It is reasonable to expect this method to work on SmB_6 because the surface states are easily accessible, and because there is no bulk contribution as there is in Bi_2Se_3. The biggest technical challenge will likely be the successful fabrication of the thin tunnel barrier (a few nm) on a clean, flat portion of SmB_6, especially one unpolluted by native oxides. Efforts to produce a similar thin Al_2O_3 barrier for gated Corbino structures on polished surfaces have so far been unsuccessful. Nevertheless, if this challenge can be overcome without significant pollution from magnetic oxides, it is the author's opinion that this measurement could settle the debate over the nature of the SmB_6 surface states.

APPENDICES

APPENDIX A

Analysis of the (001) Surface Conductivity

As discussed in Section 4.4.2, the angle-dependent MR of the (001) surface states at 0.3 K and below ∼25 T does not exhibit the $\cos^2\theta$ behavior expected from the Corbino disk geometry. Figure A.1 (a – c) shows the (001) MR as a function of θ for constant magnetic field at 5, 12, and 25 T, respectively. At 5 T, the amplitude of the cosine fit is small compared to the variance in the data; thus, the uncertainty in the fitting parameters is dominated by noise, a problem which becomes worse as $B^2 \to 0$. At ∼25 T and above, the $\cos^2\theta$ fit is quite good (the residuals are quite small), and the uncertainty in the fitting parameters is very small. However, at 12 T, the data deviates somewhat from the $\cos^2\theta$ fit, suggesting that some other angle-dependent mechanism is influencing the conductivity. This behavior is seen from ∼7 T to ∼25 T in the (001) surface only. The $\cos^2\theta$ fits are very good for all field values for the (011) surface, except near where $B^2 \to 0$, as expected. Figure A.1 (d – f) shows the $\cos^2\theta$ fits for the (011) surface at the same B values for comparison.

A summary of the fits for $n(B)$ and $\mu(B)$ for the (001) surface are shown in Figure A.2. The distinct regimes of behavior discussed are evident in the plot. Above ∼25 T, $\mu(B)$ is relatively constant, and has a fit uncertainty (shaded region in Figure A.2) comparable to that of the (011) surface. In this regime, $n(B)$ also increases,

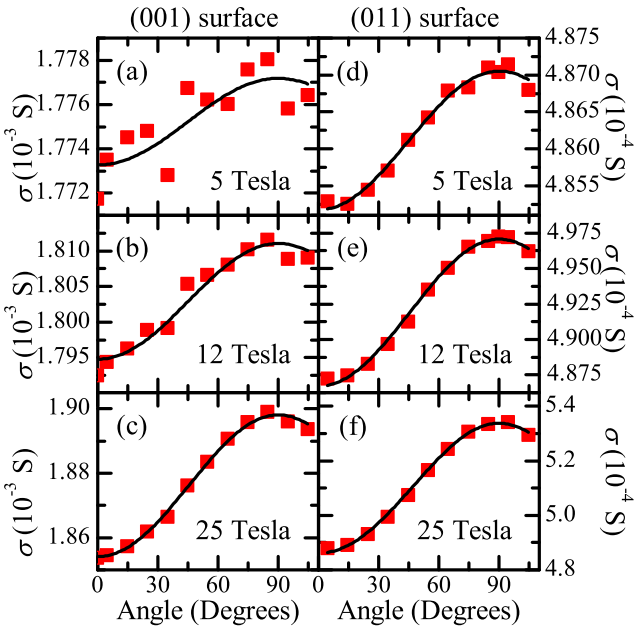

Figure A.1: Cosine fits (solid curves) of angle-dependent magnetoresistance data (red squares) at magnetic fields of 5, 12, and 25 T, respectively, for the (001) surface (a – c) and the (011) surface (d – f).

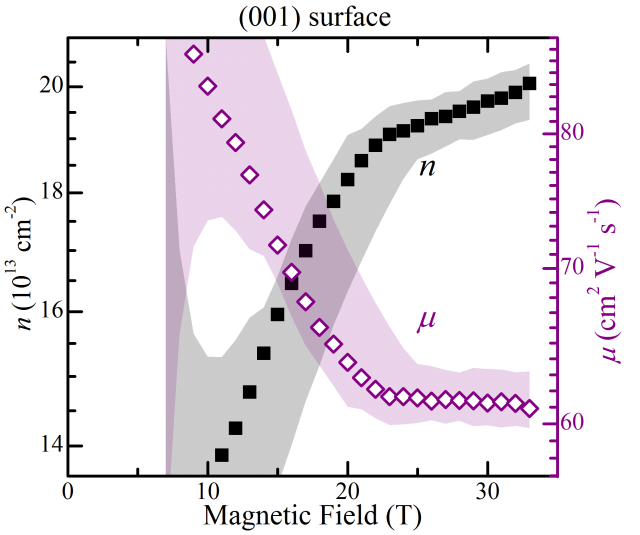

Figure A.2: (001) surface carrier density (filled squares) and mobility (open diamonds) obtained from angle-dependent fits of the data. Shaded areas represent uncertainty in the parameters of the angle-dependent fits. The vertical log scale allows direct comparison of the relative magnitudes of changes in n and μ, and is proportional to Figure 4.7 in Section 4.4.2. The reader is warned that these values are not reliable, as discussed in the text.

similarly to the (011) surface carrier density. Below ∼25 T, the calculated values for $n(B)$ and $\mu(B)$ change dramatically, and the residuals of the fits (and the corresponding fit uncertainties) become quite large. Below ∼7 T, the fits become completely unreliable, as indicated by the diverging uncertainties in $n(B)$ and $\mu(B)$.

It is likely that the (001) surface has at least two carrier types, but this possibility does not really answer why the middle regime differs a bit from both the $\cos^2\theta$ behavior and the B^2 behavior while the high-field regime follows both behaviors quite well. If the effect responsible for this difference is limited to below ∼25 T, then the values and trends obtained for $n(B)$ and $\mu(B)$ above ∼25 T may still be useful. In any case, there is no way to distinguish single carrier conduction from multi-carrier conduction with carriers of similar mobilities, either on the (001) surface or the (011) surface.

APPENDIX B

Kondo Scattering as the Origin of the Magnetoresistance

The logarithmic increase in the surface resistivity as temperature drops is an indication for Kondo scattering due to magnetic impurities near the surface of the crystal. This is the most likely origin of the logarithmic increase, since the logarithmic coefficient is not near e^2/h, as would be expected for quantum interference effects. This was initially investigated as a candidate for negative MR, since a magnetic field suppresses the formation of Kondo singlets, thereby reducing the scattering rate due to magnetic impurities. However, the maximum reduction of the scattering rate corresponds to zero contribution from the Kondo mechanism—turning Kondo scattering off. The contribution of Kondo scattering to the increase in resistivity at 0.3 K can be estimated from the difference between the actual resistivity and the background resistivity. If the magnetic field "turns off" the Kondo scattering, the resistivity should drop to the background level. However, the magnetic field reduces the resistivity well beyond this limit. This is easily seen in Figure B.1, which shows the MR data alongside simulations of the Kondo scattering predicted by the temperature dependence. The Kondo temperature T_{K} is an adjustable parameter, so plots for two values are given, which respectively under- and over-estimate the low-field MR.

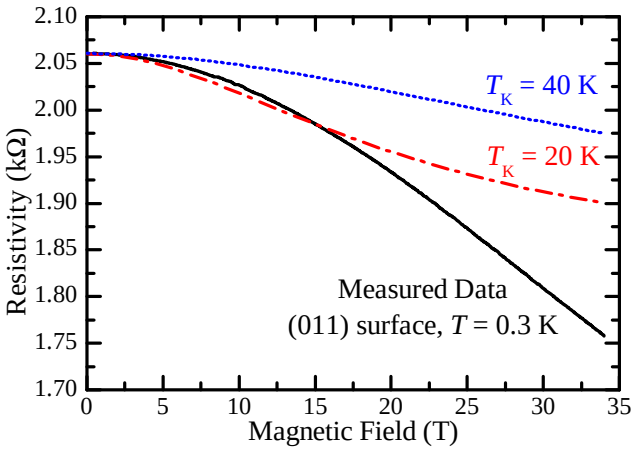

Figure B.1: Simulated magnetoresistance of the (011) surface due to Kondo scattering alone, based on the values obtained from the logarithmic temperature dependence. Simulations for Kondo temperatures of 20 K (red dash-dot curve) and 40 K (blue dotted curve) are shown alongside the actual magnetoresistance obtained from measurements (solid black curve).

However, neither value correctly captures the high-field MR observed—the magnitude of the effect at high field is smaller than the magnitude of the observed MR. Thus, the Kondo scattering mechanism alone cannot explain the magnitude of the MR observed.

APPENDIX C

Pulsed-Field Measurement Details

The data taken in pulsed magnetic fields at the NHMFL in Los Alamos were taken at 274.5 kHz due to the short 30 ms duration of the pulse. Consequently, the contribution to the signal from lead capacitance in the experimental setup is not negligible. The AC excitation current was generated as a digitally synthesized voltage at MHz frequencies, which is then applied across a bias resistor and stepped up using a transformer with a 1:10 winding ratio. A 10 Ω resistor embedded in the transformer permits the direct measurement of the excitation current applied to the sample cables. The cables to the probe were shielded Twinax. The probe leads were twisted-pair phosphor bronze with a one-way resistance of ∼24 Ω and a conductor-to-conductor capacitance between ∼250 – 350 pF. A second pair of twisted-pair leads used to measure the sample voltage were connected to a Twinax cable and fed to a preamplifier. The output of both this preamplifier and the voltage across the 10 Ω resistor were each amplified by model SR560 preamplifiers with band-pass filters between 10 kH and 1 MHz (6 db/oct), then digitized by an in-house NHMFL lock-in amplifier at a data acquisition rate of ∼20 MHz. The total circuit is depicted in Figure C.1. The output of the lock-in amplifiers was digitally smoothed with a simulated Butterworth filter.

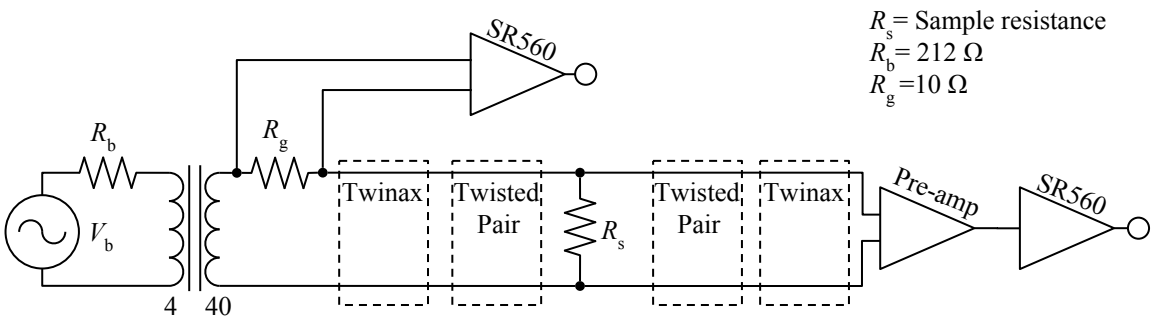

Figure C.1: Schematic diagram of the circuit used to measure resistance during the high-field magnetic pulses.

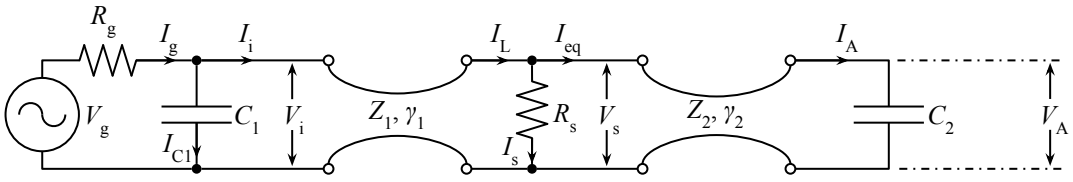

Figure C.2: Schematic diagram of the effective circuit used to model the influence of the signal cable impedance.

To model the contribution of the lead impedance, transmission line analysis is used to relate currents and voltages on each end of the leads in terms of the characteristic impedance and propagation constant of the lead wire. For this particular situation, the inductance and conductor-to-conductor leakage is negligible, so we can use a model that contains only conductor-to-conductor capacitance and in-line resistance. In addition, the Twinax lines have negligible in-line resistance, so their contribution to the circuit can be modeled as capacitors. This model is depicted in the schematic in Figure C.2.

For a single transmission line circuit, the voltage and current along any point at distance z measured from the load end can be expressed as

$$V(z) = I_{\mathrm{L}} \left(Z_{\mathrm{L}} \cosh(\gamma z) + Z_0 \sinh(\gamma z) \right) \tag{C.1}$$

$$I(z) = \frac{I_{\mathrm{L}}}{Z_0}\left(Z_{\mathrm{L}}\sinh(\gamma z) + Z_0\cosh(\gamma z)\right), \tag{C.2}$$

where I_{L} is the load current, Z_{L} is the load impedance, $Z_0 = \sqrt{R/i\omega C}$ is the characteristic impedance of the transmission line, and $\gamma = \sqrt{i\omega RC}$ is the propagation constant of the transmission line (R and C are defined per unit length here). The effective input impedance of the transmission line at z looking toward the load end is given by [181]

$$Z(z) = Z_0\frac{Z_{\mathrm{L}} + Z_0\tanh(\gamma z)}{Z_0 + Z_{\mathrm{L}}\tanh(\gamma z)}.$$

In the model presented in Figure C.2, there are two transmission lines. It is helpful to define the effective input impedance of the second line as seen by the sample,

$$Z_{\mathrm{eq}} \equiv \frac{V_{\mathrm{s}}}{I_{\mathrm{eq}}}.$$

Because the load seen by the second transmission line is just the impedance of capacitor 2 ($Z_{\mathrm{C2}} = -\frac{i}{\omega C_2}$), Z_{eq} can be expressed in terms of this and the transmission line characteristics as [181]

$$Z_{\mathrm{eq}} = Z_2\frac{Z_{\mathrm{C2}} + Z_2\tanh(\gamma_2 l_2)}{Z_2 + Z_{\mathrm{C2}}\tanh(\gamma_2 l_2)}.$$

Now, the effective load seen by the first transmission line can be expressed in terms of Z_{eq} and the sample resistance R_{s} as

$$Z_{\mathrm{L}} = \frac{R_{\mathrm{s}}Z_{\mathrm{eq}}}{R_{\mathrm{s}} + Z_{\mathrm{eq}}}.$$

The input voltage and current V_{i} and I_{i} of the first transmission line can be expressed, using Equations C.1 and C.2, as

$$V_{\mathrm{i}} = V(z = l_1) = I_{\mathrm{L}}\left(Z_{\mathrm{L}}\cosh(\gamma_1 l_1) + Z_1\sinh(\gamma_1 l_1)\right)$$

$$I_{\mathrm{i}} = I(z = l_1) = \frac{I_{\mathrm{L}}}{Z_1} \left(Z_{\mathrm{L}} \sinh(\gamma_1 l_1) + Z_1 \cosh(\gamma_1 l_1) \right).$$

I_{g} is directly measured, and is given by $I_{\mathrm{g}} = I_{\mathrm{i}} + I_{\mathrm{C1}} = I_{\mathrm{i}} + \frac{V_{\mathrm{i}}}{Z_{\mathrm{C1}}}$, where Z_{C1} is the impedance of capacitor 1, equal to $-\frac{i}{\omega C_1}$. The measured current then simplifies to

$$I_{\mathrm{g}} = V_{\mathrm{s}} \left((\frac{1}{Z_{\mathrm{L}}} + \frac{1}{Z_{\mathrm{C1}}}) \cosh(\gamma_1 l_1) + (\frac{1}{Z_1} + \frac{Z_1}{Z_{\mathrm{C1}} Z_{\mathrm{L}}}) \sinh(\gamma_1 l_1) \right), \tag{C.3}$$

which expresses the measured current I_{g} in terms of the voltage at the sample V_{s}.

Meanwhile, Equation C.1 can also be used to express the voltage across the sample V_{s} in terms of the measured voltage at the amplifier V_{A},

$$V_{\mathrm{s}} = V(z = l_2) = I_{\mathrm{A}} \left(Z_{\mathrm{C2}} \cosh(\gamma_2 l_2) + Z_2 \sinh(\gamma_2 l_2) \right),$$

which, since $I_{\mathrm{A}} = \frac{V_{\mathrm{A}}}{Z_{\mathrm{C2}}}$, simplifies to

$$V_{\mathrm{s}} = V_{\mathrm{A}} \left(\cosh(\gamma_2 l_2) + \frac{Z_2}{Z_{\mathrm{C2}}} \sinh(\gamma_2 l_2) \right). \tag{C.4}$$

The quantity $V_{\mathrm{A}}/I_{\mathrm{g}}$ can be defined as a measured impedance Z_{M}, which, by combining Equations C.3 and C.4, can be expressed in terms of the capacitor impedances, the transmission line characteristic impedances, the sample impedance, and the transmission line lengths and propagation constants as

$$\begin{aligned} Z_{\mathrm{M}} = \Bigg[& \left(\cosh(\gamma_2 l_2) + \frac{Z_2}{Z_{\mathrm{C2}}} \sinh(\gamma_2 l_2) \right) \\ & \times \left((\frac{1}{Z_{\mathrm{L}}} + \frac{1}{Z_{\mathrm{C1}}}) \cosh(\gamma_1 l_1) + (\frac{1}{Z_1} + \frac{Z_1}{Z_{\mathrm{C1}} Z_{\mathrm{L}}}) \sinh(\gamma_1 l_1) \right) \Bigg]^{-1}. \end{aligned}$$

Because the Twinax cables have roughly the same length and physical characteristics, we can simplify this expression by substituting $Z_{\mathrm{C1}} = Z_{\mathrm{C2}} = Z_{\mathrm{C}}$. Also, since the twisted pair are the same length with similar transmission characteristics, we can

take $Z_1 = Z_2 = Z_0$, $\gamma_1 = \gamma_2 = \gamma$, and $l_1 = l_2 = l$. Z_M then simplifies to

$$Z_\mathrm{M} = \frac{R_\mathrm{s} Z_0 Z_\mathrm{C}^2}{Z_\mathrm{C}\cosh(\gamma l) + Z_0 \sinh(\gamma l)\left[Z_0(2R_\mathrm{s} + Z_\mathrm{C})\cosh(\gamma l) + (Z_0^2 + 2R_\mathrm{s}Z_\mathrm{C})\sinh(\gamma l)\right]}.$$

Solving for the sample resistance R_s,

$$R_\mathrm{s} = \frac{-Z_0 Z_\mathrm{M}\left(Z_\mathrm{C}\cosh(\gamma l) + Z_0\sinh(\gamma l)\right)^2}{-Z_0 Z_\mathrm{C}^2 + 2Z_0 Z_\mathrm{C} Z_\mathrm{M}\cosh(2\gamma l) + Z_0^2 Z_\mathrm{M}\sinh(2\gamma l) + Z_\mathrm{C}^2 Z_\mathrm{M}\sinh(2\gamma l)}.$$

Z_M undergoes a small attenuation and phase rotation $e^{i\theta - x}$ at the amplifiers, so this must be included in the data analysis. Measurements of the four-terminal impedances (at zero field) both at the data acquisition frequency of 274.5 kHz and the DC limit permit a best fit of the parameters Z_C, x, and θ to be obtained. Such a fit gives a small attenuation ($x = 0.0435$) and phase rotation ($\theta = -5°$), with a Twinax capacitance around 381 pF, a value comparable to the twisted pair capacitance. The conversion from Z_M to R_s is not very sensitive to uncertainty in the capacitances and attenuation, so long as they together provide a best-fit conversion between the 274.5 kHz data and the DC-limit data.

APPENDIX D

Carrier Density Fitting Source Code

In order to evaluate the B dependence of the carrier density n and mobility μ, the following algorithm was employed:

1. Calculate a rough average of B-independent μ from the angle dependence of the data.

2. Calculate a 6^{th}-order even polynomial fit of $n(B)$ using the value of μ and the raw conductivity of the perpendicular field data:

$$n_{\text{fit}}(B) = \sum_{i=0}^{6} n_i B^i$$

3. Treating the four coefficients of the polynomial fit n_{fit} as a 4-space vector,

$$\vec{n} = \begin{pmatrix} n_0 & n_2 & n_4 & n_6 \end{pmatrix},$$

take a step in every direction in the 4-space.

4. For each new value of $\vec{n}$ (including the original position), calculate $\mu(B)$ from the parallel field data and the polynomial $n_{\text{fit}}(B)$ represented by $\vec{n}$.

Coefficient	5° and 85°	25° and 85°
n_0	2.59709×10^{17}	2.43638×10^{17}
n_2	-4.55092×10^{12}	2.16432×10^{13}
n_4	4.15697×10^{10}	1.21876×10^{10}
n_6	-1.11826×10^{7}	6.76019×10^{5}

Table D.1: List of fitting parameters for $n(B)$.

5. Use the calculated $\mu(B)$ and $n_{\text{fit}}(B)$ to calculate the expected behavior of the perpendicular field data.

6. Compare the calculated perpendicular field data to the experimental perpendicular field data and calculate a residual.

7. Select the value of $\vec{n}$ that resulted in the smallest residual. If the residual at the original $\vec{n}$ is smallest, then reduce the step size and iterate back to step 3. Otherwise, set the $n_{\text{fit}}(B)$ polynomial coefficients to the $\vec{n}$ value that resulted in the smallest residual, keep the same step size, and iterate back to step 3.

This algorithm performs a 4-space search for the polynomial coefficients of $n_{\text{fit}}(B)$ that gives the best fit for both parallel and perpendicular field data. Starting from a given 4-space coordinate represented by $\vec{n}$, it checks nearby coordinates a given step size away for a better fit, moving to values that produce a better fit. If the current value is the best fit, the step size is reduced. This can be done an arbitrary number of times until the local minimum of the residual in 4-space is found to arbitrary precision. It uses two data sets as input, which is enough to fully constrain both $n(B)$ and $\mu(B)$. Because multiple angles of magnetic field data are available, these parameters were calculated for at least two different sets of data from different field angles. The resulting parameters are close, but do not agree completely, suggesting the presence of some subtle angle dependence of $n(B)$ and $\mu(B)$.

The best coefficients for two sets of angles are summarized in Table D.1. The fit and search algorithm was implemented in Wolfram Mathematica using the code that follows. The raw dataset for each magnetic field angle used was input as a 2D array composed of a 1D list of magnetic fields and a 1D list of corresponding conductivities. The output generated represents $\mu(B)$ and the fitting parameters of $n_{\text{fit}}(B)$.

The following code defines some constants and imports the data:

```
e=1.60217657*10^-19;Dropnum=1;
DataPar=Import["Sept24 Corbino MC Parallel.dat"];
DataPerp=Import["Sept24 Corbino MC Perp.dat"];
Data24=Import["Sept24 Corbino MC 24 degrees.dat"];
```

This code is for the 5° and 85° data sets.

```
iterations=10;dimension=3;Mins={};CenterTracks={};Φ=1.475;
    Θ=0.07854;
n={2.597089956169586`*^17,-4.550921031660455`*^12,
        4.156968817399798`*^10,-1.1182585923241468`*^7};
Centers=n;Ranges
    ={2.2208241576417218`*^11,2.9141614497713125`*^8,
        291416.1449771313`,169.3508780843028`}10000;
While[iterations>0,
end=0;
While[end==0,
cube=Table[0,{i,0,dimension-1},{j,0,dimension-1},{k,0,
    dimension-1},{l,0,dimension-1}];
For[n[[1]]=Centers[[1]]-Ranges[[1]];i=1,n[[1]]<=Centers[[1]]+
    Ranges[[1]],i++;n[[1]]=n[[1]]+Ranges[[1]],
For[n[[2]]=Centers[[2]]-Ranges[[2]];j=1,n[[2]]<=Centers[[2]]+
    Ranges[[2]],j++;n[[2]]=n[[2]]+Ranges[[2]],
```

```
For[n[[3]]=Centers[[3]]-Ranges[[3]];k=1,n[[3]]<=Centers[[3]]+
    Ranges[[3]],k++;n[[3]]=n[[3]]+Ranges[[3]],
For[n[[4]]=Centers[[4]]-Ranges[[4]];l=1,n[[4]]<=Centers[[4]]+
    Ranges[[4]],l++;n[[4]]=n[[4]]+Ranges[[4]],
μ={First[#],(e n.{1,First[#]^2,First[#]^4,First[#]^6}-Sqrt[(e
     n.{1,First[#]^2,First[#]^4,First[#]^6})^2-(2 Last[#]First
    [#]Cos[Φ])^2])/(2Last[#]First[#]^2 Cos[Φ]^2)}&/@ Drop[
    DataPar,Dropnum];
residual=(((n[[1]]+n[[2]] First[#]^2+n[[3]] First[#]^4+n[[4]]
    First[#]^6)e Last[#])/(1+Last[#]^2 First[#]^2 Cos[Θ]^2)&/@
    μ)-(Last[#]&/@Drop[DataPerp,Dropnum]);
cube[[i,j,k,l]]=Total[#^2&/@residual];]]]];
If[Centers==(Flatten[Position[cube,Min[cube]]]-2)Ranges+
    Centers,end=1];
Centers=(Flatten[Position[cube,Min[cube]]]-2)Ranges+Centers;
CenterTracks=Append[CenterTracks,Centers];
Mins = Append[Mins,Position[cube,Min[cube]]];];
Ranges=Ranges/3;iterations--;];
n=Centers;μ={First[#],(e n.{1,First[#]^2,First[#]^4,First
    [#]^6}-Sqrt[(e n.{1,First[#]^2,First[#]^4,First[#]^6})
    ^2-(2 Last[#]First[#]Cos[Φ])^2])/(2Last[#]First[#]^2 Cos[
    Φ]^2)}&/@ Drop[DataPar,Dropnum];
Export["UPerp.dat",μ];
```

This code is for the 25° and 85° data sets. It is identical to the previous code, except for the inputs and corresponding input variable names.

```
iterations=10;dimension=3;Mins={};CenterTracks={};Φ=1.475;
    Θ=0.427606;
```

```
n={2.4363755361042518`*^17,2.1643219699754734`*^13,
        1.218763277833064`*^10,676019.3831669716`};
Centers=n;Ranges
    ={2.2208241576417218`*^11,2.9141614497713125`*^8,
        291416.1449771313`,169.3508780843028`}10000;
While[iterations>0,
end=0;
While[end==0,
cube=Table[0,{i,0,dimension-1},{j,0,dimension-1},{k,0,
    dimension-1},{l,0,dimension-1}];
For[n[[1]]=Centers[[1]]-Ranges[[1]];i=1,n[[1]]<=Centers[[1]]+
    Ranges[[1]],i++;n[[1]]=n[[1]]+Ranges[[1]],
For[n[[2]]=Centers[[2]]-Ranges[[2]];j=1,n[[2]]<=Centers[[2]]+
    Ranges[[2]],j++;n[[2]]=n[[2]]+Ranges[[2]],
For[n[[3]]=Centers[[3]]-Ranges[[3]];k=1,n[[3]]<=Centers[[3]]+
    Ranges[[3]],k++;n[[3]]=n[[3]]+Ranges[[3]],
For[n[[4]]=Centers[[4]]-Ranges[[4]];l=1,n[[4]]<=Centers[[4]]+
    Ranges[[4]],l++;n[[4]]=n[[4]]+Ranges[[4]],
μ={First[#],(e n.{1,First[#]^2,First[#]^4,First[#]^6}-Sqrt[(e
     n.{1,First[#]^2,First[#]^4,First[#]^6})^2-(2 Last[#]First
    [#]Cos[Φ])^2])/(2Last[#]First[#]^2 Cos[Φ]^2)}&/@ Drop[
    DataPar,Dropnum];
residual=(((n[[1]]+n[[2]] First[#]^2+n[[3]] First[#]^4+n[[4]]
    First[#]^6)e Last[#])/(1+Last[#]^2 First[#]^2 Cos[Θ]^2)&/@
    μ)-(Last[#]&/@Drop[Data24,Dropnum]);
cube[[i,j,k,l]]=Total[#^2&/@residual];]]]];
```

```
If[Centers==(Flatten[Position[cube,Min[cube]]]-2)Ranges+
    Centers,end=1];
Centers=(Flatten[Position[cube,Min[cube]]]-2)Ranges+Centers;
CenterTracks=Append[CenterTracks,Centers];
Mins = Append[Mins,Position[cube,Min[cube]]];];
Ranges=Ranges/3;iterations--;];
n=Centers;μ={First[#],(e n.{1,First[#]^2,First[#]^4,First
    [#]^6}-Sqrt[(e n.{1,First[#]^2,First[#]^4,First[#]^6})
    ^2-(2 Last[#]First[#]Cos[Φ])^2])/(2Last[#]First[#]^2 Cos[
    Φ]^2)}&/@ Drop[DataPar,Dropnum];
Export["U24.dat",μ];
```

APPENDIX E

CS4-10V Magnet Sweeper Program

To simplify the operation of the superconducting magnet, this LabView VI program interfaces with the Cryomagnetics, Inc. CS4-10V Magnet Power Supply and uses this interface to sweep the magnet current between two user-specified values at a user-specified sweep rate repeatedly and continuously until stopped by the user. The program provides updated information about the magnet-current value, its sweep status, the number of elapsed sweep cycles, and any errors that arise with the interface or from the supply.

The basic features of the program can be seen in the user interface in Figure E.1. Before the program is run, the user must specify the interface address of the power supply in the "CS-4 Address" field, the lower and upper current limits in the "Lower Limit" and "Upper Limit" fields, respectively, the limit tolerance in the "Limit Tolerance" field, and the sweep rate in the "Sweep Rate (Range 1)" field. When the user then starts the program, the "Lower Limit," "Upper Limit," and "Limit Tolerance" fields are disabled from further input. Any invalid values that lie outside the power supply's capabilities are coerced to within the allowed range, and the limit values are reported in the fields next to the corresponding input fields. To change these values, the program must be stopped by the user with the "Stop" button, which re-enables

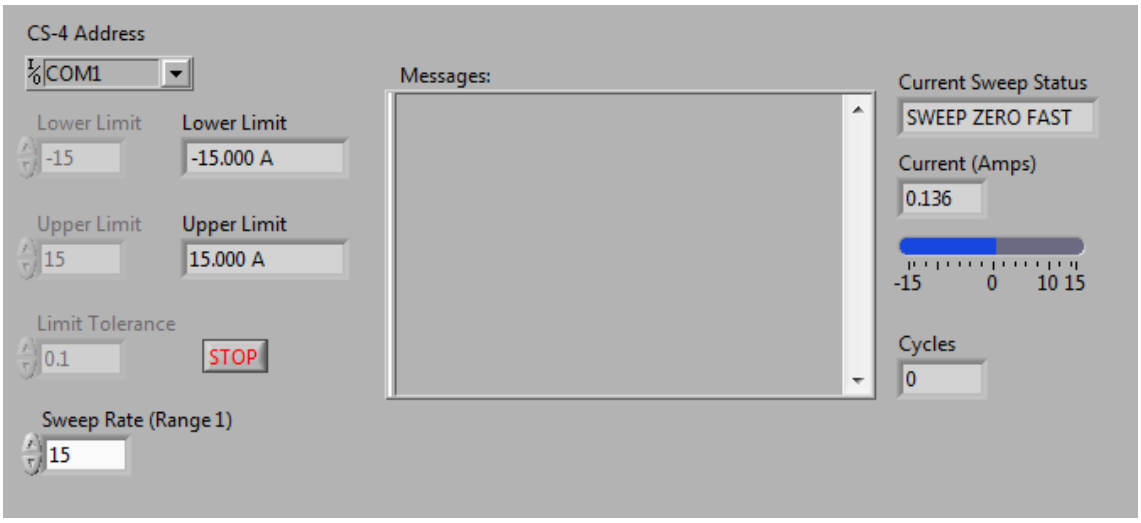

Figure E.1: CS4-10V Sweeper Program user interface.

the input fields, begins sweeping the current to zero, and stops the program. The "Limit Tolerance" is useful for faster sweep direction switching. The CS4-10V gradually slows the sweep as it approaches a set limit. This program will switch the sweep direction when the current reported by the CS4-10V is within the Limit Tolerance of the set limit, thus avoiding the careful, gradual process of reaching the limit.

Status indicators are located on the right side of the panel. The "Message" box reports any error messages that occur. The "Current Sweep Status" will read "SWEEP UP," "SWEEP DOWN," or "SWEEP ZERO FAST," depending on the current direction or whether the program has been stopped. The "Current (Amps)" field will provide the continuously updated value of the current. This is also displayed graphically on the status bar, whose limits are automatically set according to the user-set current limits at the start of the program. The number of sweep cycles that have elapsed are reported in the "Cycles" field.

The implementation is contained entirely in the back panel of the VI (no custom sub-VI's are used), which is shown in Figure E.2. Because of the large graphical format of the code, sections of it are depicted in Figures E.5 – E.12. Additionally, a

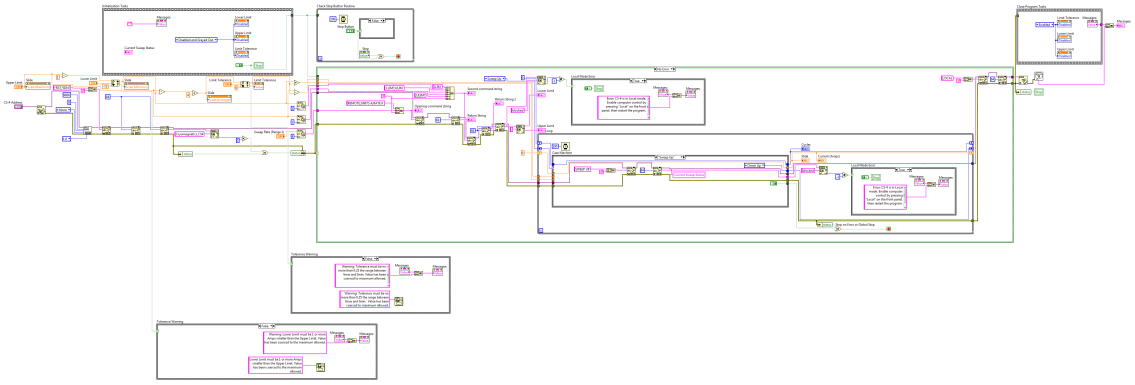

Figure E.2: Sweeper Program back panel

flowchart summarizes the operation of the program in Figures E.3 – E.4. The major sections of the code can be divided into the following sections:

- **User interface initialization** – This thread, depicted at the upper left of Figure E.3, disables the relevant inputs on the front panel and unlatches the "Stop" button. A second thread, depicted at the upper right of Figure E.3, coerces the input values to allowed values, generates a warning if a value is coerced, displays the limits on the front panel, and sets the status bar range to span the two limits.

- **CS4-10V initialization** – This thread, depicted at the upper center of Figure E.3, opens a Virtual Instrument Software Architecture (VISA) interface with the CS4-10V and queries its identity. It generates an error code if the instrument times out or is not a CS4-10V power supply. If there is an error, the Main program loop is skipped and the program closes.

- **CS4-10V configuration** – This section, summarized at the lower right of Figure E.3, programs the CS4-10V. It first sets the CS4-10V to "Remote" mode and the limit units to Amps, then programs the sweep rate and the limit values. The current implementation also queries the CS4-10V to verify the values were

correctly set, but these are reported to hidden indicators on the front panel, and not used later. If the instrument is in "Local" mode, an error is generated and the program is stopped.

- **Main program loop (case machine)** – The main program is set up as a case machine with five cases. One case switches the sweep direction up, while another case then monitors the current until it reaches the Upper Limit. A third case then switches the sweep direction down, and the fourth case monitors the current until it reaches the Lower Limit. A fifth case is triggered by the Check Stop Button Routine, sets the CS4-10V to sweep to zero, and terminates the case machine loop. Every case executes basic error detection and updates the indicators on the front panel. The basic flow of the case machine is summarized in Figure E.4.

- **Check Stop Button Routine** – This process, depicted in the lower left of Figure E.3, continuously monitors the "Stop" button and any error conditions. When one of these are triggered, it signals the Main loop (case machine) to execute the ending case.

- **Program closing** – This section, summarized at the bottom of Figure E.4, returns the CS4-10V to "Local" mode, closes the VISA interface, and re-enables the front panel controls, displaying any final error messages.

The initialization procedures can be seen in Figure E.5. The user interface initialization, located within a sequence structure, disables the front-panel inputs, clears the message box, and sets the "Stop" button to False. These are executed within the sequence structure before the Main program loop or Check Stop Button Routine begin. This order is enforced by an artificial data dependency of these two loops on the sequence structure. This ensures that the local "Stop" variable within the Check

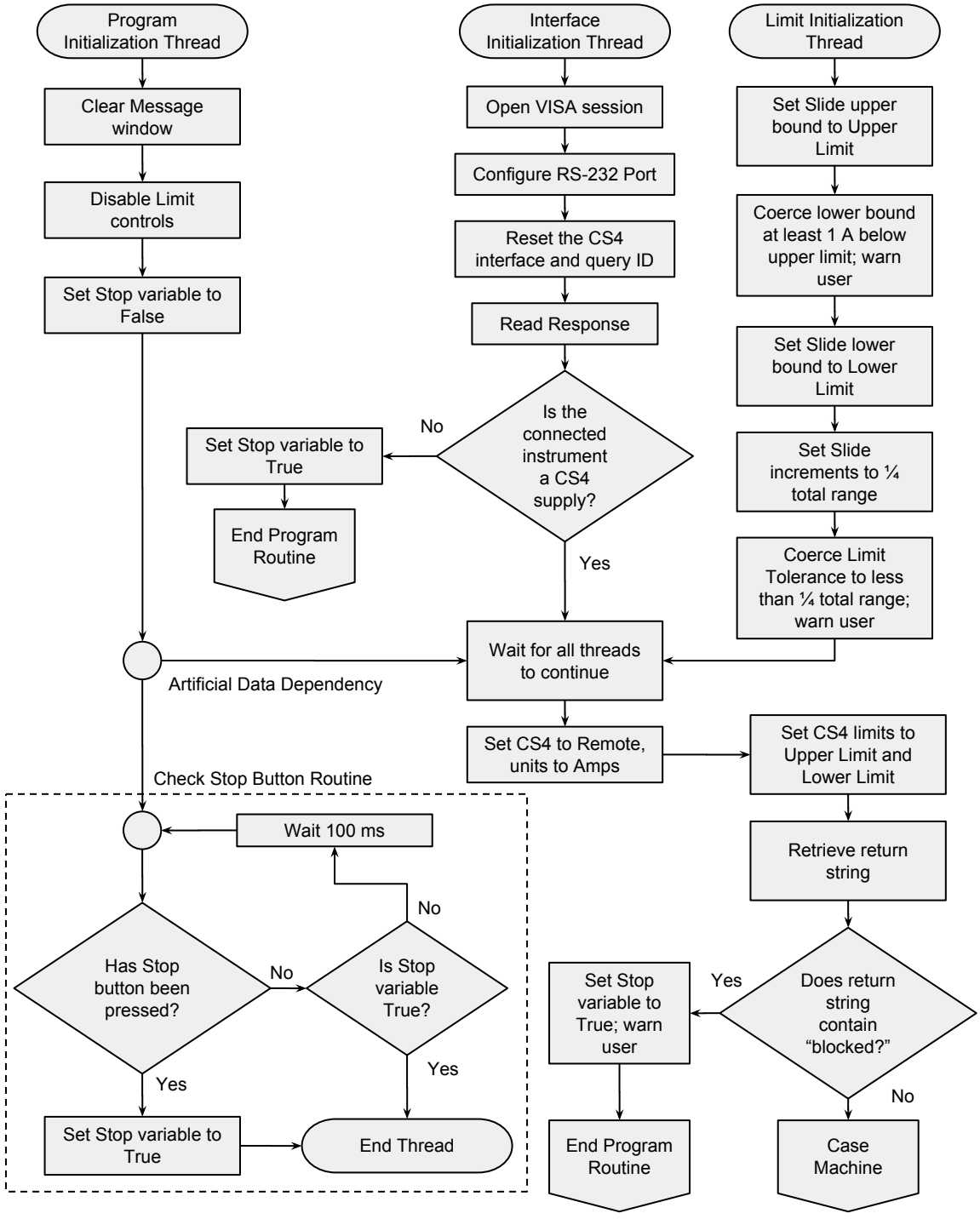

Figure E.3: Sweeper Program flowchart 1

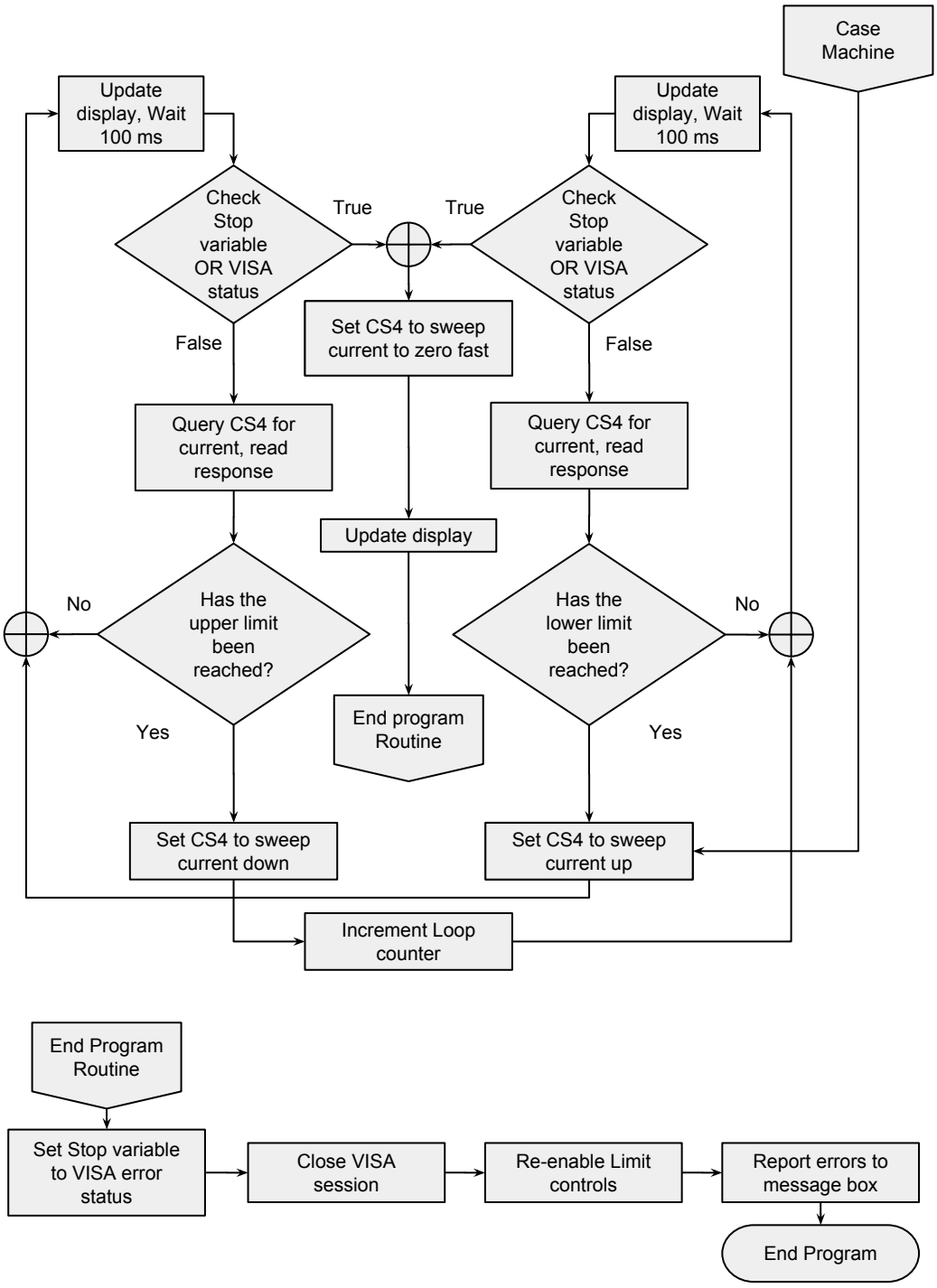

Figure E.4: Sweeper Program flowchart 2

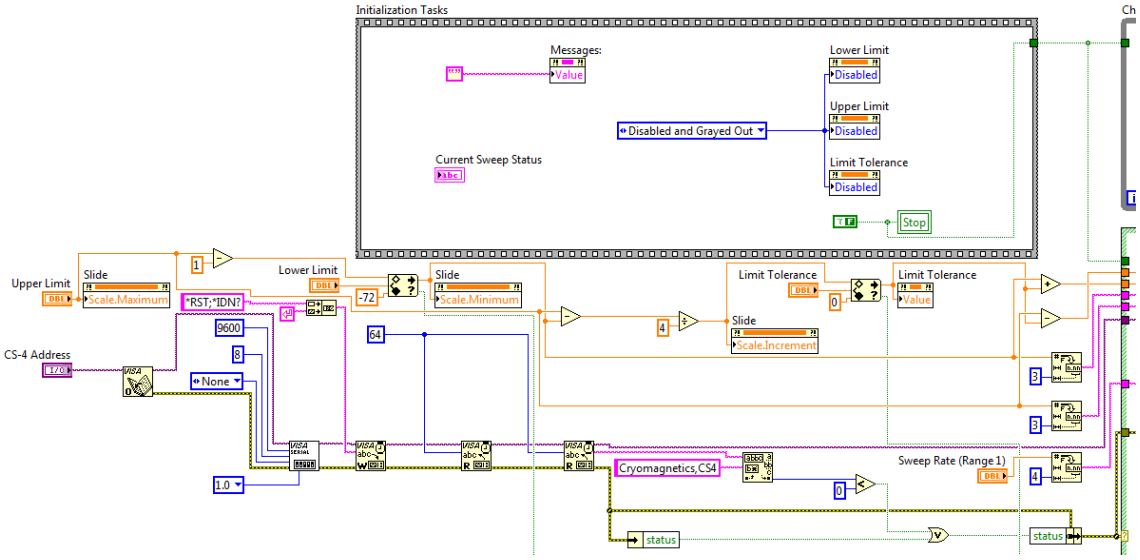

Figure E.5: Initialization routines

Stop Button routine is not set early before the program has a chance to ensure the "Stop" button is set to False.

The ranges of the Upper and Lower Limit inputs are restricted to allowed values in the control properties. Additionally, the Lower Limit is coerced to be at least 1 Amp below the Upper Limit. If this coercion occurs, the warning shown in the case structure in Figure E.6 is output both to the message box and as a popup window. The True case is empty. Each limit is used to program the respective limits of the status bar. The difference of the two limits is divided by 4, and this value is used to program the scale on the status bar so that it displays five numeric values. The Limit Tolerance is also coerced to a value between 0 Amps and a quarter of the full range. If this coercion occurs, the warning shown in the case structure in Figure E.7 is appended to the message box and generates a popup window. The True case is empty. Finally, the Limit Tolerance is added to the Lower Limit and subtracted from the Upper Limit, and these are input to the Main loop as reference values to trigger the change in sweep direction.

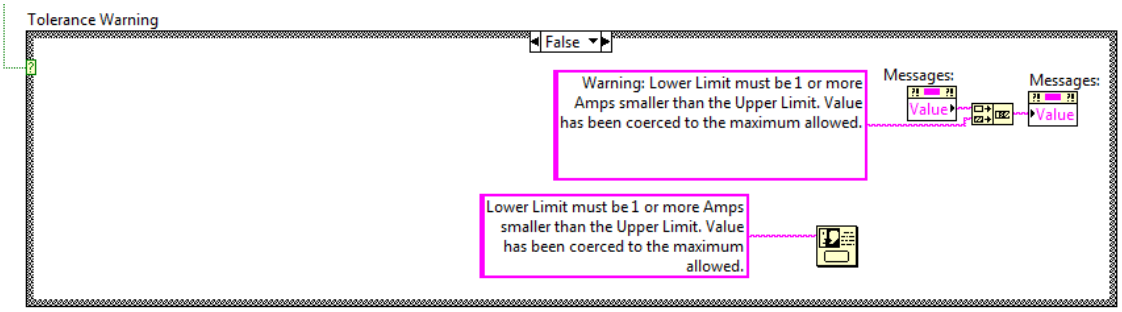

Figure E.6: Coercion warning for minimum range

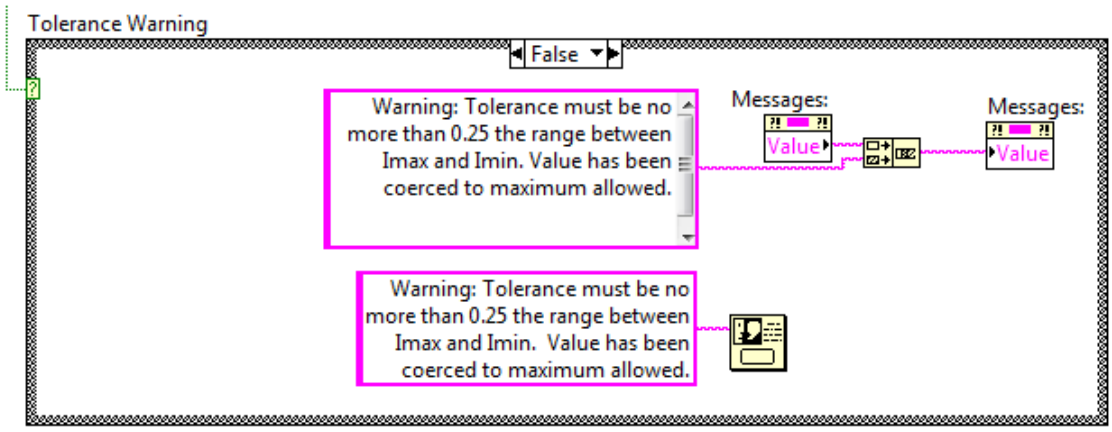

Figure E.7: Coercion warning for Limit Tolerance

The CS4-10V initialization uses the user-input VISA address to open a VISA session and configure it for the RS-232 port as required by the CS4-10V. A *RST reset and *IDN? identification query are sent to the instrument. The read buffer must be cleared once before the query response can be read. The return string is searched for "Cryomagnetics,CS4" to verify that the instrument is indeed a CS4-10V. If this is not found, or if any of the read/write commands generates an error, the Main loop is skipped (the "Error" case is empty), and the program proceeds directly to the VISA close routines after the Main loop.

Once all the preceding steps are complete, the instrument setup can start (Figure E.8). The "Remote" command, "Unit" command, and "Sweep Rate" command (concatenated with a string version of the Sweep Rate input value) are sent as a single string; the read buffer is then read to clear it. A second concatenated string of commands programs, then queries both the Lower Limit and the Upper Limit. The read buffer is again cleared, then read yet again. The output string from the CS4-10V is split into the Upper and Lower Limits, and these are displayed on the front panel to the user. If the CS4-10V string contains the warning "Blocked," the case structure above the Main loop in Figure E.9 will append an error message to the message box and trigger the local "Stop" variable to signal the Main loop to stop. This is necessary, since a command that is blocked by the CS4-10V "Local" mode will not generate an interface error; this must be checked explicitly.

The "Case" portion of the Main loop is seen in context in Figure E.9. The case machine is initialized to the "Sweep Up" case. Each case determines the following case via a feedback node on the loop. The contents of each case are depicted in Figure E.10. Each iteration of the loop (each case) is constrained to execute at most once per 100 ms.

The "Sweep Up" case begins by sending the "SWEEP UP" command to the CS4-10V, then reads the read buffer, placing the output to the local "Current Sweep

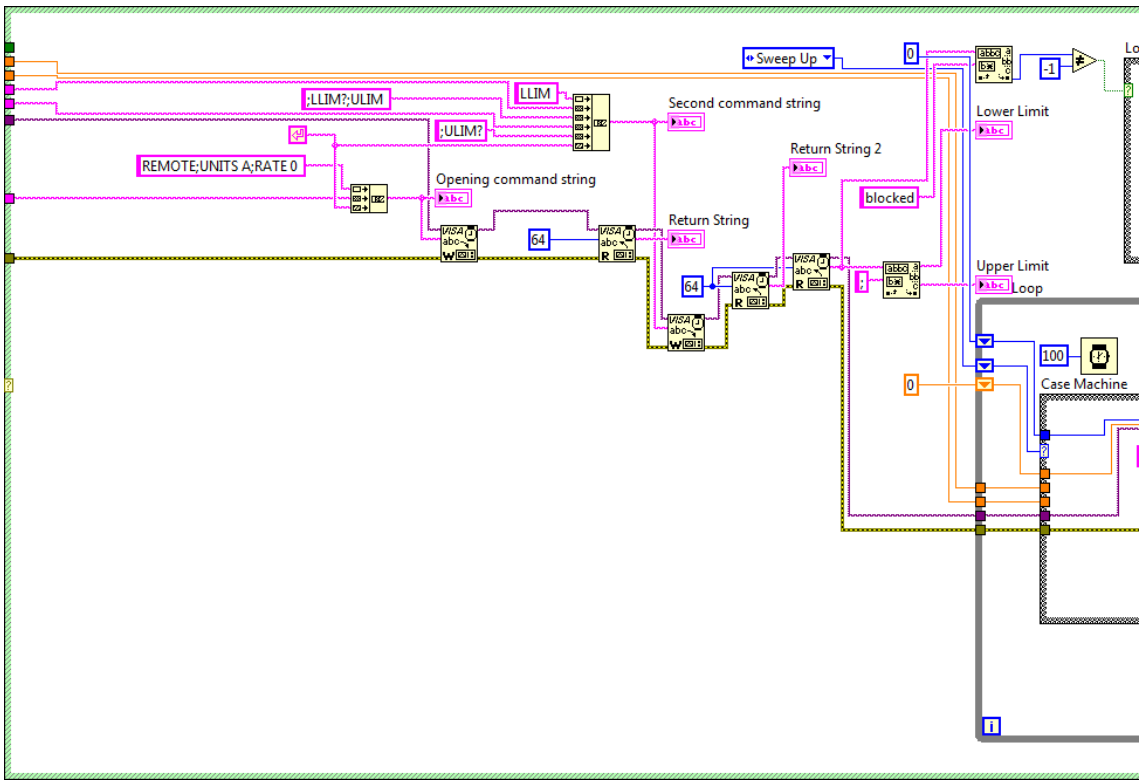

Figure E.8: Instrument setup routine

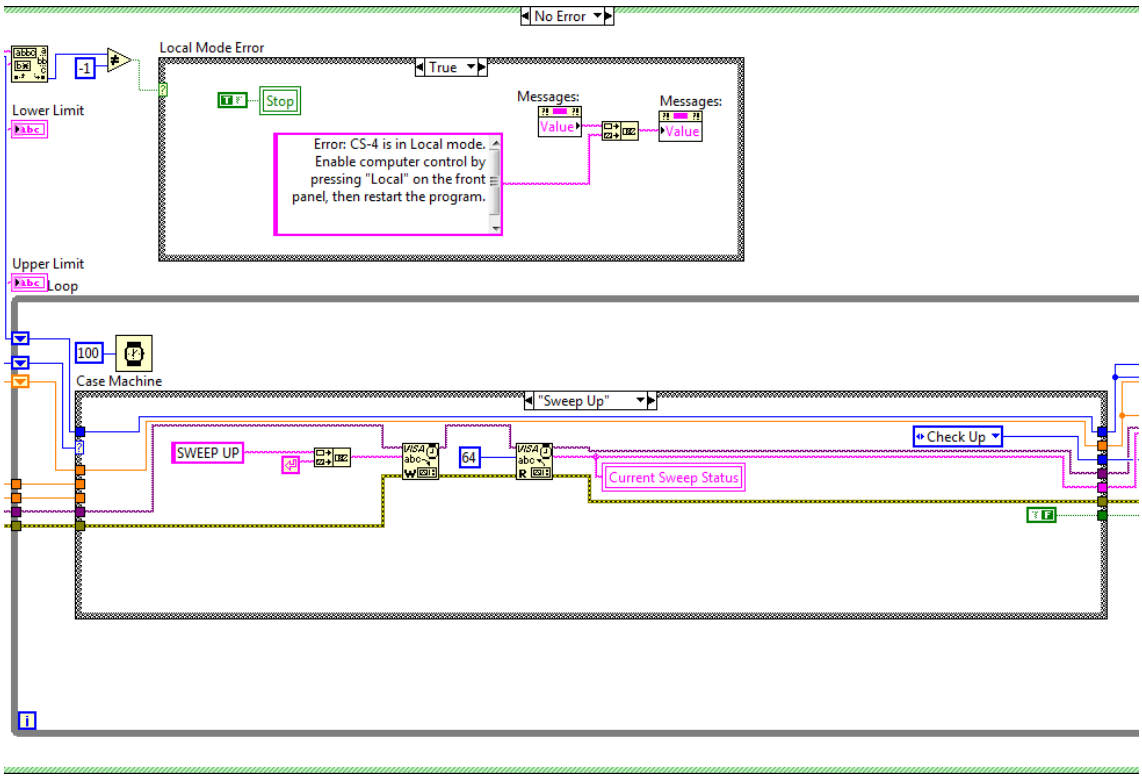

Figure E.9: Main program loop (left side)

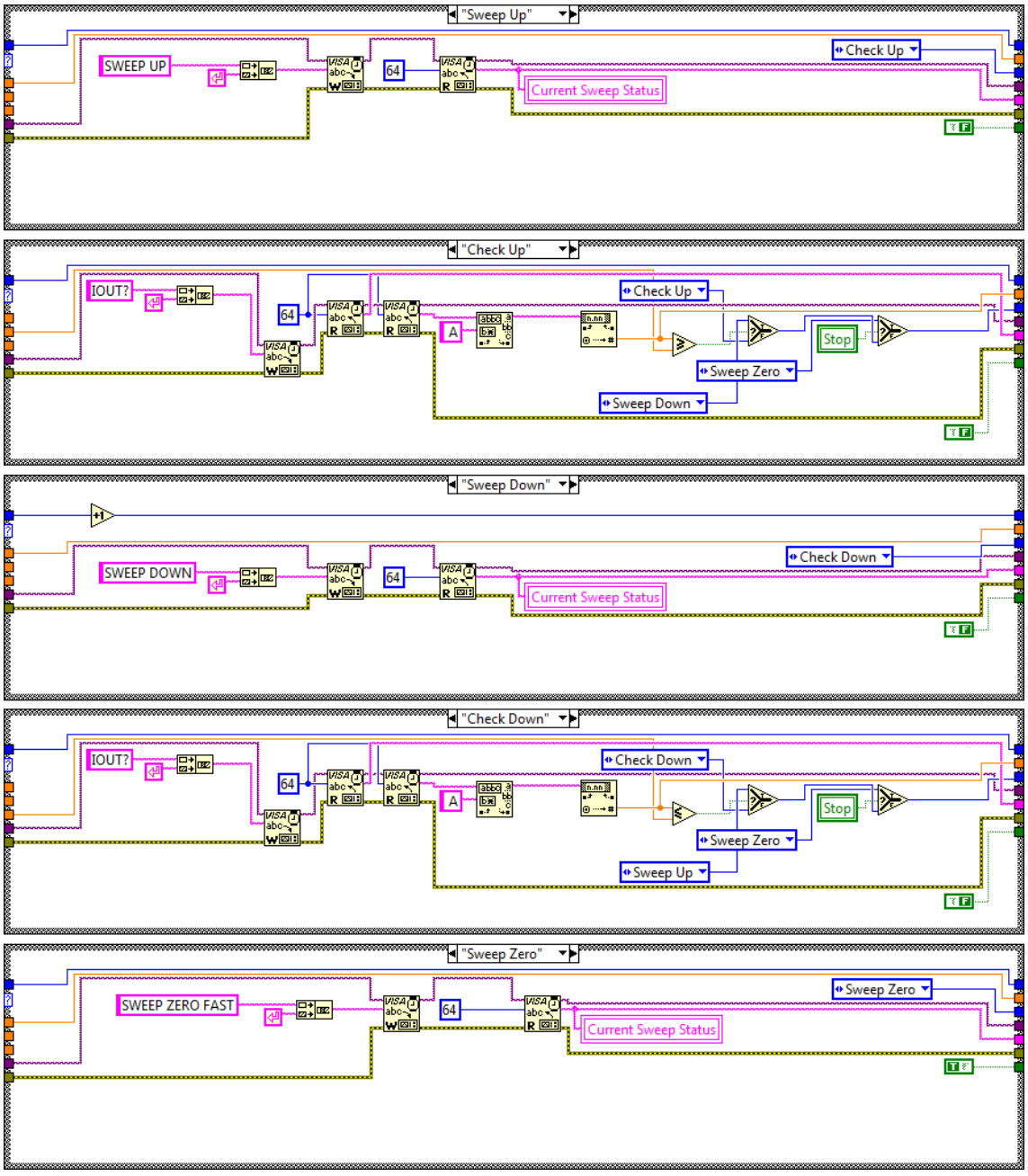

Figure E.10: Case machine cases

Status" variable. The output is also provided as a case structure output for error checking. The "Check Up" case is selected as the next case, and a False Boolean is provided for the loop stop routine.

The "Check Up" case queries the CS4-10V for the current value, clears the read buffer (this string is fed to the case structure output), and reads the response. The numeric value is extracted from the output string, converted to numeric representation, and compared to the Upper Limit (− tolerance). If the Upper Limit has been reached, the "Sweep Down" case is tentatively selected. Otherwise, the "Check Up" case is tentatively selected. The local "Stop" variable is then checked. If the Stop condition is True, then the "Sweep Zero" case is selected. Otherwise, the tentative "Sweep Down" or "Check Up" case is selected. Thus, the "Check Up" case will run continuously until either the Upper Limit is reached by the CS4-10V (in which case the "Sweep Down" case will execute next) or the Stop condition is True (in which case the "Sweep Zero" case will execute). A False Boolean is provided for the loop stop routine.

The "Sweep Down" and "Check Down" cases are almost identical to their "Up" counterparts, except that the "SWEEP DOWN" command is used and the current is compared to the Lower Limit (+ tolerance). However, the "Sweep Down" case contains one subtle difference. A numeric variable passed by a reference node is used to keep track of the number of sweep cycles. When, and only when, this case is executed, the sweep cycle number is incremented by one.

The "Sweep Zero" case is similar to the "Sweep Up" case, but it sends the command "SWEEP ZERO FAST" instead. A True Boolean is supplied to the loop stop routine to end the Main loop. The "Sweep Zero" case is selected as the next case, but the program will not execute the next case.

After each case is executed, the following occurs (Figure E.11): The number of elapsed cycles is updated, and the current value outputs (the numeric indicator

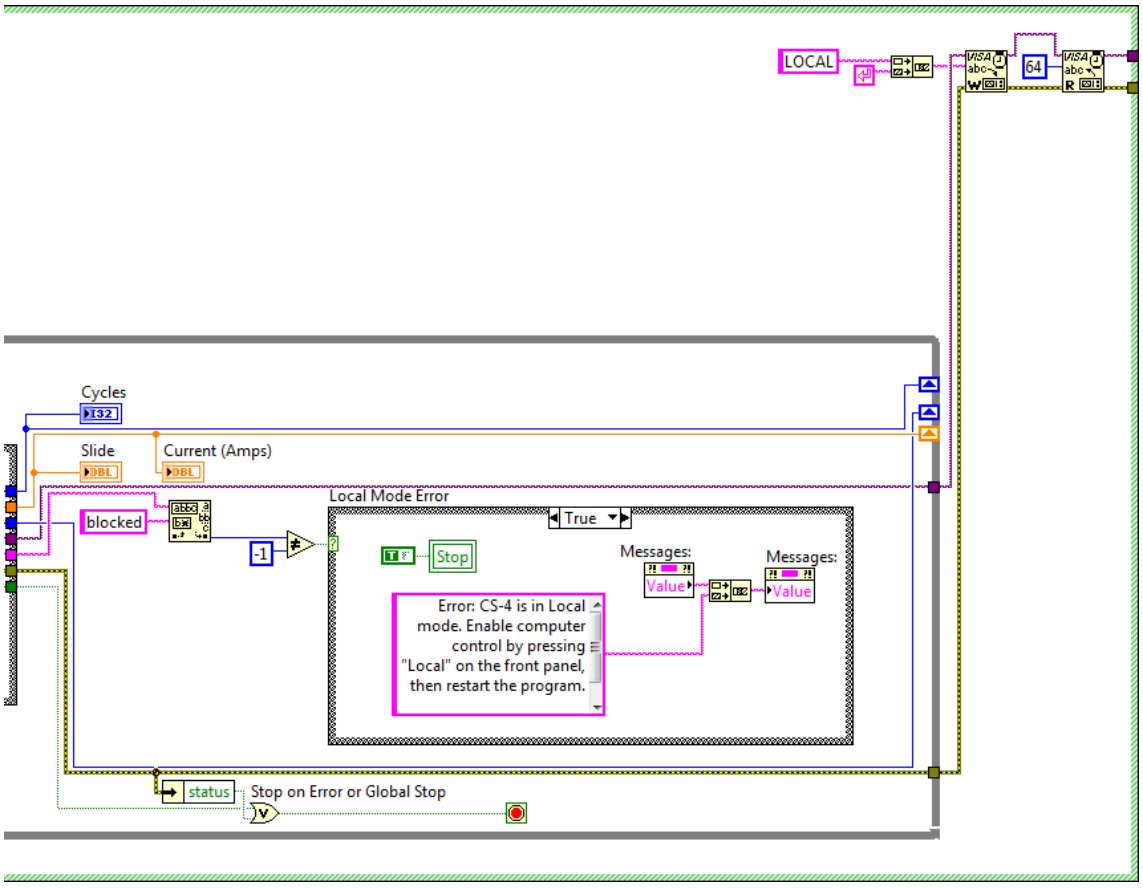

Figure E.11: Main program loop (right side)

and the status bar) are updated. The responses from the CS4-10V are checked for the term "Blocked," and warning messages are generated exactly as described in the instrument setup routine, using identical code. Finally, if either the VISA error status or the local "Stop" variable are True, the Main loop is terminated.

Once the Main loop has ended, a final "LOCAL" command is sent to the CS4-10V to re-enable the instrument's front-panel controls, and the read buffer is cleared. In Figure E.12, the VISA session is then closed, and any VISA errors are appended to the message box. Artificial data dependency is used to begin execution of the sequence structure after the Main loop ends. This sequence structure re-enables the controls on the VI front panel. The artificial data dependency is also used to ensure

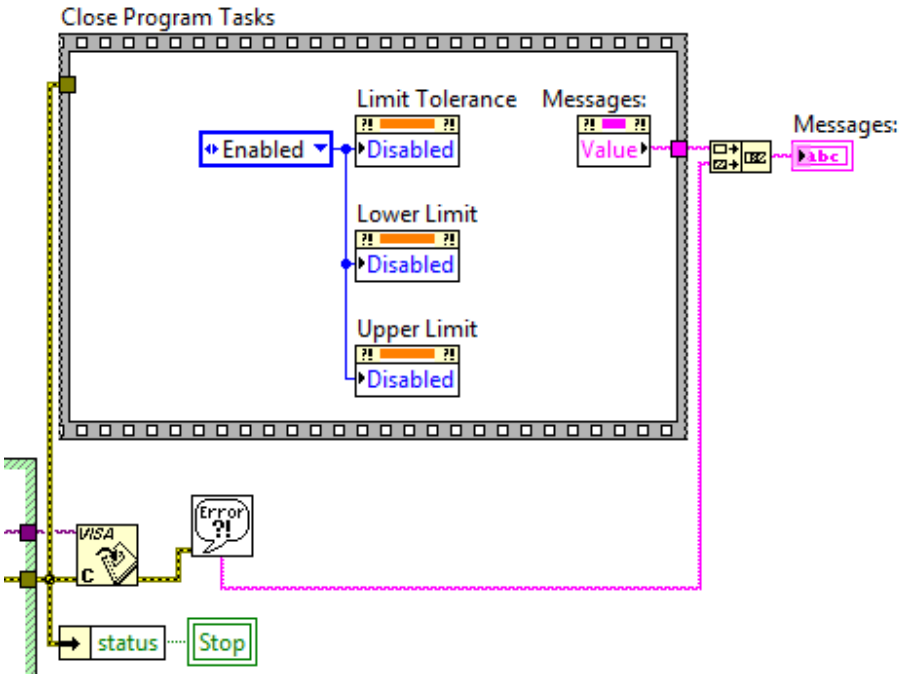

Figure E.12: Program-closing routine

that the VISA error messages are appended to the message box text as it appeared when the Main loop closed.

The Check Stop Button routine runs in parallel with the case machine, once the artificial data dependency on the initialization routines is satisfied. The loop, shown in Figure E.13, executes once every 100 ms, and simply monitors the status of the "Stop" button. If the "Stop" button is latched by the user, the case structure sets the local "Stop" variable to True (the False case is empty). The loop will terminate upon this condition, or if the local "Stop" variable is True (due to a generated error).

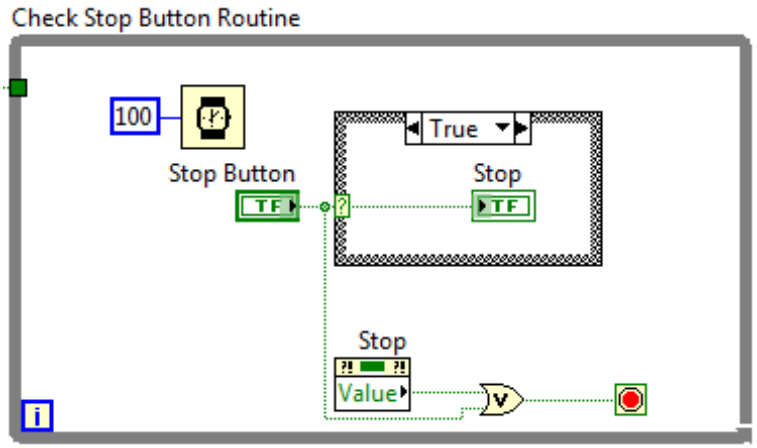

Figure E.13: Check Stop Button routine

BIBLIOGRAPHY

BIBLIOGRAPHY

[1] V. A. Trounov, A. L. Malyshev, D. Y. Chernyshov, M. M. Korsukova, V. N. Gurin, L. A. Aslanov, and V. V. Chernyshev, "Temperature dependences of the parameters of atoms in the crystal structure of the intermediate-valence semiconductor SmB_6: investigation by high-resolution powder neutron diffraction", Journal of Physics: Condensed Matter **5**, 2479 (1993).

[2] A. Menth, E. Buehler, and T. H. Geballe, "Magnetic and Semiconducting Properties of SmB_6", Phys. Rev. Lett. **22**, 295 (1969).

[3] S. Otani, H. Nakagawa, Y. Nishi, and N. Kieda, "Floating Zone Growth and High Temperature Hardness of Rare-Earth Hexaboride Crystals: LaB_6, CeB_6, PrB_6, NdB_6, and SmB_6", Journal of Solid State Chemistry **154**, 238 (2000).

[4] R. L. Cohen, M. Eibschütz, and K. W. West, "Electronic and Magnetic Structure of SmB_6", Phys. Rev. Lett. **24**, 383 (1970).

[5] R. L. Cohen, M. Eibschütz, K. W. West, and E. Buehler, "Electronic Configuration of SmB_6", Journal of Applied Physics **41**, 898 (1970).

[6] M. Eibschütz, R. L. Cohen, E. Buehler, and J. H. Wernick, "Mössbauer Isomer Shifts in Sm^{149} Compounds", Phys. Rev. B **6**, 18 (1972).

[7] C. M. Varma, "Mixed-valence compounds", Rev. Mod. Phys. **48**, 219 (1976).

[8] J. M. D. Coey, S. K. Ghatak, M. Avignon, and F. Holtzberg, "Electronic configuration of samarium sulphide and related compounds: Mössbauer-effect measurements and a model", Phys. Rev. B **14**, 3744 (1976).

[9] J. C. Nickerson, R. M. White, K. N. Lee, R. Bachmann, T. H. Geballe, and G. W. Hull, "Physical Properties of SmB_6", Phys. Rev. B **3**, 2030 (1971).

[10] D. K. Wohllenben and B. R. Coles, in *Magnetism*, Vol. V, edited by H. Suhl (Academic, New York, 1973), p. 47.

[11] J. W. Allen, R. M. Martin, B. Batlogg, and P. Wachter, "Mixed valent SmB_6 and gold-SmS: Metals or insulators?", Journal of Applied Physics **49** (1978).

[12] T. Kasuya, K. Kojima, and M. Kasaya, in *Valence Instabilities and Related Narrow Band Phenomena*, edited by R. D. Parks (Plenum, New York, 1977), p. 137.

[13] C. M. Varma, in *Valence Instabilities and Related Narrow Band Phenomena*, edited by R. D. Parks (Plenum, New York, 1977), p. 201.

[14] B. Coqblin and A. Blandin, "Stabilité des Moments Magnétiques Localisés dans les Métaux", Advances in Physics **17**, 281 (1968), eprint: http://dx.doi.org/10.1080/00018736800101306.

[15] N. F. Mott, "Rare-earth compounds with mixed valencies", Philosophical Magazine **30**, 403 (1974).

[16] J. W. Allen, B. Batlogg, and P. Wachter, "Large Low-Temperature Hall Effect and Resistivity in Mixed-Valent SmB_6", Phys. Rev. B **20**, 4807 (1979).

[17] J. Friedel, "Metallic alloys", English, Il Nuovo Cimento **7**, 287 (1958).

[18] T. Kasuya, "A Mechanism for the Metal Insulator Transition and Various Properties in Samarium Compounds", J. Phys. Colloques **37**, C4 (1976).

[19] G. Travaglini and P. Wachter, "Intermediate-valent SmB_6 and the hybridization model: An optical study", Phys. Rev. B **29**, 893 (1984).

[20] B. Batlogg, P. H. Schmidt, and J. M. Rowell, "Evidence for a small energy gap in SmB_6", in *Valence fluctuations in solids*, edited by L. M. Falicov, W. Hanke, and M. B. Maple (North-Holland, Amsterdam, 1981), p. 267.

[21] I. Frankowski and P. Wachter, "Point-contact spectroscopy on SmB_6, TmSe, LaB_6 and LaSe", Solid State Commun. **41**, 577 (1982).

[22] P. W. Anderson, in *Valence fluctuations in solids*, edited by L. M. Falicov, W. Hanke, and M. B. Maple (North-Holland, Amsterdam, 1981), p. 451.

[23] N. F. Mott, in *Valence instabilities*, edited by P. Wachter and H. Boppart (North-Holland, Amsterdam, 1982), p. 402.

[24] R. M. Martin and J. W. Allen, "Theory of mixed valence: Metals or small gap insulators (invited)", Journal of Applied Physics **50**, 7561 (1979).

[25] R. M. Martin and J. W. Allen, in *Valence fluctuations in solids*, edited by L. M. Falicov, W. Hanke, and M. B. Maple (North-Holland, Amsterdam, 1981), p. 85.

[26] G. Aeppli and Z. Fisk, Comments Cond. Mat. Phys. **16**, 155 (1992).

[27] T. S. Al'tshuler, V. N. Mironov, G. G. Khaliullin, and D. I. Khomskii, "Observation of the temperature dependence of the energy gap in SmB_6 by the EPR method", Pis'ma Zh. Eksp. Teor. Fiz. **40**, 28 (1984).

[28] T. S. Al'tshuler, G. G. Khaliullin, and D. I. Khomskii, "Investigation of the energy gap in SmB_6 by the ESR method", Zh. Eksp. Teor. Fiz. **90**, 2104 (1986).

[29] J. D. Denlinger, J. W. Allen, J.-S. Kang, K. Sun, B.-I. Min, D.-J. Kim, and Z. Fisk, *Temperature Dependence of Linked Gap and Surface State Evolution in the Mixed Valent Topological Insulator SmB_6*, 2013, arXiv:1312.6637 [cond-mat.str-el].

[30] N. F. Mott, *Metal-Insulator Transitions* (Taylor and Francis, London, 1974), p. 27.

[31] T. Kasuya, K. Takegahara, T. Fujita, T. Tanaka, and E. Bannai, "Valence Fluctuating State in SmB_6", J. Phys. Colloques **40**, C5 (1979).

[32] J. C. Cooley, M. C. Aronson, Z. Fisk, and P. C. Canfield, "SmB_6: Kondo Insulator or Exotic Metal?", Phys. Rev. Lett. **74**, 1629 (1995).

[33] A. Kebede, M. C. Aronson, C. M. Buford, P. C. Canfield, J. H. Cho, B. R. Coles, J. C. Cooley, J. Y. Coulter, Z. Fisk, J. D. Goettee, W. L. Hults, A. Lacerda, T. D. McLendon, P. Tiwari, and J. L. Smith, "Studies of the correlated electron system SmB_6", Physica B: Condensed Matter **223–224**, Proceedings of the International Conference on Strongly Correlated Electron Systems, 256 (1996).

[34] K. Flachbart, S. Gabáni, E. Konovalova, Y. Paderno, and V. Pavlík, "Ground state formation in intermediate valent SmB_6", Physica B: Condensed Matter **293**, 417 (2001).

[35] B. Gorshunov, N. Sluchanko, A. Volkov, M. Dressel, G. Knebel, A. Loidl, and S. Kunii, "Low-energy electrodynamics of SmB_6", Phys. Rev. B **59**, 1808 (1999).

[36] J. D. Denlinger, G.-H. Gweon, J. W. Allen, C. G. Olson, Y. Dalichaouch, B.-W. Lee, M. B. Maple, Z. Fisk, P. C. Canfield, and P. E. Armstrong, "Advances in photoemission spectroscopy of f-electron materials", Physica B: Condensed Matter **281–282**, 716 (2000).

[37] S.-K Mo, G.-H Gweon, J. D. Denlinger, H.-D. Kim, J. W. Allen, C. G. Olson, H. Höchst, J. L. Sarrao, and Z. Fisk, "ARPES study of X-point band overlaps in LaB_6 and SmB_6 – contrast to SrB_6 and EuB_6", Physica B: Condensed Matter **312–313**, The International Conference on Strongly Correlated Electron Systems, 668 (2002).

[38] S. Nozawa, T. Tsukamoto, K. Kanai, T. Haruna, S. Shin, and S. Kunii, "Ultrahigh-resolution and angle-resolved photoemission study of SmB_6", Journal of Physics and Chemistry of Solids **63**, Proceedings of the 8th ISSP International Symposium, 1223 (2002).

[39] S. Souma, H. Kumigashira, T. Ito, T. Takahashi, and S. Kunii, "Direct observation of pseudogap of SmB_6 using ultrahigh-resolution photoemission spectroscopy", Physica B: Condensed Matter **312–313**, The International Conference on Strongly Correlated Electron Systems, 329 (2002).

[40] L. Fu and C. L. Kane, "Superconducting Proximity Effect and Majorana Fermions at the Surface of a Topological Insulator", Phys. Rev. Lett. **100**, 096407 (2008).

[41] F. Wilczek, "Majorana Returns", Nat. Phys. **5**, 614 (2009).

[42] C. L. Kane and E. J. Mele, "Quantum Spin Hall Effect in Graphene", Phys. Rev. Lett. **95**, 226801 (2005).

[43] C. L. Kane and E. J. Mele, "Z_2 Topological Order and the Quantum Spin Hall Effect", Phys. Rev. Lett. **95**, 146802 (2005).

[44] B. A. Bernevig and S.-C. Zhang, "Quantum Spin Hall Effect", Phys. Rev. Lett. **96**, 106802 (2006).

[45] M. König, S. Wiedmann, C. Brüne, A. Roth, H. Buhmann, L. W. Molenkamp, X.-L. Qi, and S.-C. Zhang, "Quantum Spin Hall Insulator State in HgTe Quantum Wells", Science **318**, 766 (2007), eprint: `http://www.sciencemag.org/content/318/5851/766.full.pdf`.

[46] J. E. Moore and L. Balents, "Topological invariants of time-reversal-invariant band structures", Phys. Rev. B **75**, 121306 (2007).

[47] L. Fu, C. L. Kane, and E. J. Mele, "Topological Insulators in Three Dimensions", Phys. Rev. Lett. **98**, 106803 (2007).

[48] R. Roy, "Topological phases and the quantum spin Hall effect in three dimensions", Phys. Rev. B **79**, 195322 (2009).

[49] D. Hsieh, D. Qian, L. Wray, Y. Xia, Y. S. Hor, R. J. Cava, and M. Z. Hasan, "A topological Dirac insulator in a quantum spin Hall phase", Nature **452**, 970 (2008).

[50] A. A. Taskin and Y. Ando, "Quantum oscillations in a topological insulator $Bi_{1-x}Sb_x$", Phys. Rev. B **80**, 085303 (2009).

[51] P. Roushan, J. Seo, C. V. Parker, Y. S. Hor, D. Hsieh, D. Qian, A. Richardella, M. Z. Hasan, R. J. Cava, and A. Yazdani, "Topological surface states protected from backscattering by chiral spin texture", Nature **460**, 1106 (2009).

[52] Y. Ando, "Topological Insulator Materials", Journal of the Physical Society of Japan **82**, 102001 (2013), eprint: `http://dx.doi.org/10.7566/JPSJ.82.102001`.

[53] D. Hsieh, Y. Xia, L. Wray, D. Qian, A. Pal, J. H. Dil, J. Osterwalder, F. Meier, G. Bihlmayer, C. L. Kane, Y. S. Hor, R. J. Cava, and M. Z. Hasan, "Observation of Unconventional Quantum Spin Textures in Topological Insulators", Science **323**, 919 (2009), eprint: `http://www.sciencemag.org/content/323/5916/919.full.pdf`.

[54] A. Nishide, A. A. Taskin, Y. Takeichi, T. Okuda, A. Kakizaki, T. Hirahara, K. Nakatsuji, F. Komori, Y. Ando, and I. Matsuda, "Direct mapping of the spin-filtered surface bands of a three-dimensional quantum spin Hall insulator", Phys. Rev. B **81**, 041309 (2010).

[55] J. Chen, H. J. Qin, F. Yang, J. Liu, T. Guan, F. M. Qu, G. H. Zhang, J. R. Shi, X. C. Xie, C. L. Yang, K. H. Wu, Y. Q. Li, and L. Lu, "Gate-Voltage Control of Chemical Potential and Weak Antilocalization in Bi_2Se_3", Phys. Rev. Lett. **105**, 176602 (2010).

[56] C. H. Li, O. M. J. van 't Erve, J. T. Robinson, Y. Liu, L. Li, and B. T. Jonker, "Electrical detection of charge-current-induced spin polarization due to spin-momentum locking in Bi_2Se_3", Nature Nanotechnology **9**, 218 (2014).

[57] S. Hong, V. Diep, S. Datta, and Y. P. Chen, "Modeling potentiometric measurements in topological insulators including parallel channels", Phys. Rev. B **86**, 085131 (2012).

[58] T. Öztürk, R. L. Field III, Y. S. Eo, S. Wolgast, K. Sun, and Ç. Kurdak, *Influence of Helical Spin Structure on the Magnetoresistance of an Ideal Topological Insulator*, Dec. 2014, arXiv:1412.1007.

[59] Y. Xia, D. Qian, D. Hsieh, L. Wray, A. Pal, H. Lin, A. Bansil, D. Grauer, Y. S. Hor, R. J. Cava, and M. Z. Hasan, "Observation of a large-gap topological-insulator class with a single Dirac cone on the surface", Nature Physics **5**, 398 (2009).

[60] H. Cao, S. Xu, I. Miotkowski, J. Tian, D. Pandey, M. Z. Hasan, and Y. P. Chen, "Structural and electronic properties of highly doped topological insulator Bi_2Se_3 crystals", physica status solidi (RRL) – Rapid Research Letters **7**, 133 (2013).

[61] L. Fu and C. L. Kane, "Topological insulators with inversion symmetry", Phys. Rev. B **76**, 045302 (2007).

[62] H. Zhang, C.-X. Liu, X.-L. Qi, X. Dai, Z. Fang, and S.-C. Zhang, "Topological insulators in Bi_2Se_3, Bi_2Te_3 and Sb_2Te_3 with a single Dirac cone on the surface", Nature Physics **5**, 438 (2009).

[63] Y. L. Chen, J. G. Analytis, J.-H. Chu, Z. K. Liu, S.-K. Mo, X. L. Qi, H. J. Zhang, D. H. Lu, X. Dai, Z. Fang, S. C. Zhang, I. R. Fisher, Z. Hussain, and Z.-X. Shen, "Experimental Realization of a Three-Dimensional Topological Insulator, Bi_2Te_3", Science **325**, 178 (2009), eprint: http://www.sciencemag.org/content/325/5937/178.full.pdf.

[64] D. Hsieh, Y. Xia, D. Qian, L. Wray, F. Meier, J. H. Dil, J. Osterwalder, L. Patthey, A. V. Fedorov, H. Lin, A. Bansil, D. Grauer, Y. S. Hor, R. J. Cava, and M. Z. Hasan, "Observation of Time-Reversal-Protected Single-Dirac-Cone Topological-Insulator States in Bi_2Te_3 and Sb_2Te_3", Phys. Rev. Lett. **103**, 146401 (2009).

[65] D.-X. Qu, Y. S. Hor, J. Xiong, R. J. Cava, and N. P. Ong, "Quantum Oscillations and Hall Anomaly of Surface States in the Topological Insulator Bi_2Te_3", Science **329**, 821 (2010), eprint: http://www.sciencemag.org/content/329/5993/821.full.pdf.

[66] S.-Y. Xu, L. A. Wray, Y. Xia, R. Shankar, A. Petersen, A. Fedorov, H. Lin, A. Bansil, Y. S. Hor, D. Grauer, R. J. Cava, and M. Z. Hasan, *Discovery of several large families of Topological Insulator classes with backscattering-suppressed spin-polarized single-Dirac-cone on the surface*, 2010, arXiv:1007.5111 [cond-mat.mes-hall].

[67] Z. Ren, A. A. Taskin, S. Sasaki, K. Segawa, and Y. Ando, "Large bulk resistivity and surface quantum oscillations in the topological insulator Bi_2Te_2Se", Phys. Rev. B **82**, 241306 (2010).

[68] Z. Ren, A. A. Taskin, S. Sasaki, K. Segawa, and Y. Ando, "Optimizing $Bi_{2-x}Sb_x$-$Te_{3-y}Se_y$ solid solutions to approach the intrinsic topological insulator regime", Phys. Rev. B **84**, 165311 (2011).

[69] A. A. Taskin, Z. Ren, S. Sasaki, K. Segawa, and Y. Ando, "Observation of Dirac Holes and Electrons in a Topological Insulator", Phys. Rev. Lett. **107**, 016801 (2011).

[70] M. Dzero, K. Sun, V. Galitski, and P. Coleman, "Topological Kondo Insulators", Phys. Rev. Lett. **104**, 106408 (2010).

[71] T. Takimoto, "SmB_6: A Promising Candidate for a Topological Insulator", J. Phys. Soc. Jap. **80**, 123710 (2011).

[72] S. Wolgast, Ç. Kurdak, K. Sun, J. W. Allen, D.-J. Kim, and Z. Fisk, "Low-Temperature Surface Conduction in the Kondo Insulator SmB_6", Phys. Rev. B (R) **88**, 180405 (2013).

[73] J. C. Cooley, C. H. Mielke, W. L. Hults, J. D. Goettee, M. M. Honold, R. M. Modler, A. Lacerda, D. G. Rickel, and J. L. Smith, "High Field Gap Closure in the Kondo Insulator SmB_6", Journal of Superconductivity **12**, 171 (1999).

[74] K. Furuya, "Nanofabrication by advanced electron microscopy using intense and focused beam", Sci. Technol. Adv. Mater. **9**, 014110 (2008).

[75] S. Wolgast, Y. S. Eo, T. Öztürk, G. Li, Z. Xiang, C. Tinsman, T. Asaba, B. Lawson, F. Yu, J. W. Allen, K. Sun, L. Li, Ç. Kurdak, D.-J. Kim, and Z. Fisk, "Magnetotransport measurements of the surface states of samarium hexaboride using corbino structures", Phys. Rev. B **92**, 115110 (2015).

[76] L. J. van der Pauw, Philips Res. Rep. **13**, 1 (1958).

[77] D. J. Kim, S. Thomas, T. Grant, J. Botimer, Z. Fisk, and J. Xia, "Surface Hall Effect and Nonlocal Transport in SmB_6: Evidence for Surface Conduction", Sci. Rep. -UK **3**, 3150 (2013).

[78] R. H. Harrell, J. H. Thompson, D. A. Ritchie, M. Y. Simmons, G. A. C. Jones, and M. Pepper, "Very high quality 2DEGS formed without dopant in GaAs/AlGaAs heterostructures", Journal of Crystal Growth **201–202**, 159 (1999).

[79] V. Umansky, M. Heiblum, Y. Levinson, J. Smet, J. Nübler, and M. Dolev, "MBE growth of ultra-low disorder 2DEG with mobility exceeding 35×10^6 cm^2/V s", Journal of Crystal Growth **311**, The 15th International Conference on Molecular Beam Epitaxy (MBE-XV), 1658 (2009).

[80] K. Das Gupta, A. F. Croxall, W. Y. Mak, H. E. Beere, C. A. Nicoll, I. Farrer, F. Sfigakis, and D. A. Ritchie, Semicond. Sci. Technol. **27**, 115006 (2012).

[81] M. J. Manfra, K. W. Baldwin, A. M. Sergent, K. W. West, R. J. Molnar, and J. Caissie, "Electron mobility exceeding 160000 cm^2/V s in AlGaN/GaN heterostructures grown by molecular-beam epitaxy", Applied Physics Letters **85** (2004).

[82] S. Schmult, M. J. Manfra, A. M. Sergent, A. Punnoose, H. T. Chou, D. Goldhaber-Gordon, and R. J. Molnar, Physica Status Solidi **243**, 1706 (2006).

[83] H. Cheng, Ç. Kurdak, J. H. Leach, M. Wu, and H. Morkoç, "Two-subband conduction in a gated high density InAlN/AlN/GaN heterostructure", Applied Physics Letters **97**, 112113 (2010) http://dx.doi.org/10.1063/1.3490248.

[84] E. Yamaguchi, "Electron subbands and transport properties in inversion layers of InAs and InP", Phys. Rev. B **32**, 5280 (1985).

[85] K. I. Bolotin, K. J. Sikes, Z. Jiang, M. Klima, G. Fudenberg, J. Hone, P. Kim, and H. L. Stormer, Solid St. Comm. **146**, 351 (2008).

[86] T. M. Lu, W. Pan, D. C. Tsui, C.-H. Lee, and C. W. Liu, "Fractional quantum Hall effect of two-dimensional electrons in high-mobility Si/SiGe field-effect transistors", Phys. Rev. B **85**, 121307 (2012).

[87] T. M. Kott, B. Hu, S. H. Brown, and B. E. Kane, "Valley-degenerate two-dimensional electrons in the lowest Landau level", Phys. Rev. B **89**, 041107 (2014).

[88] P. Moetakef, D. G. Ouellette, J. R. Williams, S. James Allen, L. Balents, D. Goldhaber-Gordon, and S. Stemmer, "Quantum oscillations from a two-dimensional electron gas at a Mott/band insulator interface", Applied Physics Letters **101**, 151604 (2012) http://dx.doi.org/10.1063/1.4758989.

[89] Y. Iye, "Mobility of electrons in the surface state of liquid helium", English, Journal of Low Temperature Physics **40**, 441 (1980).

[90] K. Shirahama, S. Ito, H. Suto, and K. Kono, "Surface study of liquid ^{3}He using surface state electrons", English, Journal of Low Temperature Physics **101**, 439 (1995).

[91] J. Cooley, personal communication, May 8, 2013.

[92] F. Lu, J. Z. Zhao, H. Weng, Z. Fang, and X. Dai, "Correlated Topological Insulators with Mixed Valence", Phys. Rev. Lett. **110**, 096401 (2013).

[93] L. E. Boltzmann, "On some experiments relating to Hall's phenomenon", Philosophical Magazine and Journal of Science **22**.

[94] O. M. Corbino, "Bahn der lonen in Metallen", Physikalische Zeitschrift **12**, 561 (1911).

[95] E. P. Adams, "The Hall and Corbino Effects", Proceedings of the American Philosophical Society **54**, 47 (1915).

[96] G. Li, Z. Xiang, F. Yu, T. Asaba, B. Lawson, P. Cai, C. Tinsman, A. Berkley, S. Wolgast, Y. S. Eo, D.-J. Kim, Ç. Kurdak, J. W. Allen, K. Sun, X. H. Chen, Y. Y. Wang, Z. Fisk, and L. Li, "Two-dimensional Fermi surfaces in Kondo insulator SmB_6", Science **346**, 1208 (2014), eprint: http://www.sciencemag.org/content/346/6214/1208.full.pdf.

[97] M. Neupane, N. Alidoust, S.-Y. Xu, T. Kondo, Y. Ishida, D. J. Kim, C. Liu, I. Belopolski, Y. J. Jo, T.-R. Chang, H.-T. Jeng, T. Durakiewicz, L. Balicas, H. Lin, A. Bansil, S. Shin, Z. Fisk, and M. Z. Hasan, "Surface Electronic Structure of the Topological Kondo-Insulator Candidate Correlated Electron System SmB_6", Nat. Commun. **4**, 2991 (2013).

[98] J. Jiang, S. Li, T. Zhang, Z. Sun, F. Chen, Z. R. Ye, M. Xu, Q. Q. Ge, S. Y. Tan, X. H. Niu, M. Xia, B. P. Xie, Y. F. Li, X. H. Chen, H. H. Wen, and D. L. Feng, "Observation of Possible Topological In-Gap Surface States in the Kondo insulator SmB_6 by Photoemission", Nat. Commun. **4**, 3010 (2013).

[99] P. Syers, D. Kim, M. S. Fuhrer, and J. Paglione, "Tuning Bulk and Surface Conduction in the Proposed Topological Kondo Insulator SmB_6", Phys. Rev. Lett. **114**, 096601 (2015).

[100] Y. Nakajima, P. S. Syers, X. Wang, R. Wang, and J. Paglione, *One-Dimensional Edge State Transport in a Topological Kondo Insulator*, Dec. 2013, arXiv:1312.6132 [cond-mat.str-el].

[101] S. Thomas, D. J. Kim, S. B. Chung, T. Grant, Z. Fisk, and J. Xia, *Weak Antilocalization and Linear Magnetoresistance in the Surface State of SmB_6*, July 2013, arXiv:1307.4133 [cond-mat.str-el].

[102] S. Hikami, A. I Larkin, and Y. Nagaoka, "Spin-Orbit Interaction and Magnetoresistance in the Two Dimensional Random System", Prog. Theor. Phys. **63**, 707 (1980).

[103] P. W. Anderson, E. Abrahams, and T. V. Ramakrishnan, "Possible Explanation of Nonlinear Conductivity in Thin-Film Metal Wires", Phys. Rev. Lett. **43**, 718 (1979).

[104] B. L. Altshuler, A. G. Aronov, and D. E. Khmelnitsky, "Effects of electron-electron collisions with small energy transfers on quantum localisation", Journal of Physics C: Solid State Physics **15**, 7367 (1982).

[105] H. Fukuyama and E. Abrahams, "Inelastic scattering time in two-dimensional disordered metals", Phys. Rev. B **27**, 5976 (1983).

[106] H. Miyazaki, T. Hajiri, T. Ito, S. Kunii, and S. I. Kimura, "Momentum-Dependent Hybridization Gap and Dispersive In-Gap State of the Kondo Semiconductor SmB_6", Phys. Rev. B **86**, 075105 (2012).

[107] N. Xu, X. Shi, P. K. Biswas, C. E. Matt, R. S. Dhaka, Y. Huang, N. C. Plumb, M. Radović, J. H. Dil, E. Pomjakushina, K. Conder, A. Amato, Z. Salman, D. M. Paul, J. Mesot, H. Ding, and M. Shi, "Surface and Bulk Electronic Structure of the Strongly Correlated System SmB_6 and Implications for a Topological Kondo Insulator", Phys. Rev. B(R) **88**, 121102 (2013).

[108] J. D. Denlinger, J. W. Allen, J.-S. Kang, K. Sun, B.-I. Min, D.-J. Kim, and Z. Fisk, *SmB_6 Photoemission: Past and Present*, 2013, arXiv:1312.6636.

[109] Z.-H. Zhu, A. Nicolaou, G. Levy, N. P. Butch, P. Syers, X. F. Wang, J. Paglione, G. A. Sawatzky, I. S. Elfimov, and A. Damascelli, "Polarity-Driven Surface Metallicity in SmB_6", Phys. Rev. Lett. **111**, 216402 (2013).

[110] N. Xu, P. K. Biswas, J. H. Dil, R. S. Dhaka, G. Landolt, S. Muff, C. E. Matt, X. Shi, N. C. Plumb, M. Radović, E. Pomjakushina, K. Conder, A. Amato, S. V. Borisenko, R. Yu, H.-M. Weng, Z. Fang, X. Dai, J. Mesot, H. Ding, and M. Shi, "Direct Observation of the Spin Texture in SmB_6 as Evidence of the Topological Kondo Insulator", Nat. Commun. **5**, 4566 (2014).

[111] N. Andrei, K. Furuya, and J. H. Lowenstein, "Solution of the Kondo problem", Rev. Mod. Phys. **55**, 331 (1983).

[112] X. Xin and M.-C. Yeh, "The Kondo effect in three-dimensional topological insulators", Journal of Physics: Condensed Matter **25**, 286001 (2013).

[113] W. A. Phelan, S. M. Koohpayeh, P. Cottingham, J. W. Freeland, J. C. Leiner, C. L. Broholm, and T. M. McQueen, "Correlation Between Bulk Thermodynamic Measurements and the Low-Temperature-Resistance Plateau in SmB_6", Phys. Rev. X **4**, 031012 (2014).

[114] *Brainstorm Session: SmB_6 and Related Problems*, Hao Tjeng, L., Hard X-ray Photoelectron Spectroscopy on In-situ Cleaved and Ex-situ Polished SmB_6 samples; Bulk vs. Surface Electronic Structure, UBC Quantum Matter Institute and Max Planck Institute (May 2014).

[115] P. Coleman, *Heavy fermions: Electrons at the Edge of Magnetism* (Wiley Online Library, 2007).

[116] P. Scoboria, J. E. Crow, and T. Mihalisin, "Resistive Behavior and Intermediate Valence Effects in $La_{1-x}Ce_xPd_3$ and $CePd_{3-x}Rh_x$", J. Appl. Phys. **50**, 1895 (1979).

[117] Y. Amakai, S. Murayama, Y. Obi, H. Takano, and K. Takanashi, "Evidence of a Heavy Fermion State in the Disordered Ce-Alloy System Without Translation Symmetry", Phys. Rev. B **79**, 245126 (2009).

[118] T. Ando, A. B. Fowler, and F. Stern, "Electronic properties of two-dimensional systems", Rev. Mod. Phys. **54**, 437 (1982).

[119] M. J. Manfra, L. N. Pfeiffer, K. W. West, H. L. Stormer, K. W. Baldwin, J. W. P. Hsu, D. V. Lang, and R. J. Molnar, "High-mobility AlGaN/GaN heterostructures grown by molecular-beam epitaxy on GaN templates prepared by hydride vapor phase epitaxy", Applied Physics Letters **77** (2000).

[120] G. Bergmann, "Weak localization in thin films: a time-of-flight experiment with conduction electrons", Physics Reports **107**, 1 (1984).

[121] H.-Z. Lu, J. Shi, and S.-Q. Shen, "Competition between Weak Localization and Antilocalization in Topological Surface States", Phys. Rev. Lett. **107**, 076801 (2011).

[122] A. A. Taskin, S. Sasaki, K. Segawa, and Y. Ando, "Manifestation of Topological Protection in Transport Properties of Epitaxial Bi_2Se_3 Thin Films", Phys. Rev. Lett. **109**, 066803 (2012).

[123] A. Roy, S. Guchhait, S. Sonde, R. Dey, T. Pramanik, A. Rai, H. C. P. Movva, L. Colombo, and S. K. Banerjee, "Two-dimensional weak anti-localization in Bi_2Te_3 thin film grown on Si(111)-(7×7) surface by molecular beam epitaxy", Applied Physics Letters **102**, 163118 (2013) `http://dx.doi.org/10.1063/1.4803018`.

[124] L. Saminadayar, P. Mohanty, R. A. Webb, P. Degiovanni, and C. Bäuerle, "Electron coherence at low temperatures: The role of magnetic impurities", Physica E: Low-dimensional Systems and Nanostructures **40**, 12 (2007).

[125] C. Bäuerle, F. Mallet, F. Schopfer, D. Mailly, G. Eska, and L. Saminadayar, "Experimental Test of the Numerical Renormalization-Group Theory for Inelastic Scattering from Magnetic Impurities", Phys. Rev. Lett. **95**, 266805 (2005).

[126] A. Theumann, B. Coqblin, S. G. Magalhães, and A. A. Schmidt, "Spin-Glass Freezing in Kondo-Lattice Compounds", Phys. Rev. B **63**, 054409 (2001).

[127] S. G. Magalhães, F. M. Zimmer, and B Coqblin, "Spin-glass Freezing in Kondo-Lattice Compounds in the Presence of a Random and a Transverse Magnetic Field", J. of Magn. Magn. Mater. **339**, 30 (2013).

[128] K. Binder and A. P. Young, "Spin glasses: Experimental Facts, Theoretical Concepts, and Open Questions", Rev. Mod. Phys. **58**, 801 (1986).

[129] O. S. Sarıyer, A. Kabakçıoğlu, and A. N. Berker, "Deep Spin-Glass Hysteresis-Area Collapse and Scaling in the Three-Dimensional $\pm J$ Ising Model", Phys. Rev. E **86**, 041107 (2012).

[130] T. Yokoyama and S. Murakami, "Spintronics and Spincaloritronics in Topological Insulators", Physica E: Low-dimensional Systems and Nanostructures **55**, 1 (2014).

[131] K. Flachbart, M. Bartkowiak, S. Demishev, S. Gabani, V. Glushkov, T. Herrmannsdorfer, V. Moshchalkov, N. Shitsevalova, and N. Sluchanko, "Pulsed magnetic field study of the spin gap in intermediate valence compound SmB_6", Physica B: Condensed Matter **404**, Proceedings of the International Conference on Strongly Correlated Electron Systems, 2985 (2009).

[132] K. Sugiyama, F. Iga, M. Kasaya, T. Kasuya, and M. Date, "Field-Induced Metallic State in YbB_{12} under High Magnetic Field", Journal of the Physical Society of Japan **57**, 3946 (1988), eprint: `http://dx.doi.org/10.1143/JPSJ.57.3946`.

[133] F. Chen, C. Shang, Z. Jin, D. Zhao, Y. P. Wu, Z. J. Xiang, Z. C. Xia, A. F. Wang, X. G. Luo, T. Wu, and X. H. Chen, "Magnetoresistance evidence of a surface state and a field-dependent insulating state in the Kondo insulator SmB_6", Phys. Rev. B **91**, 205133 (2015).

[134] J.-P. R. Wells, "Laser spectroscopy of alkaline earth fluoride crystals doped with trivalent samarium and europium ions", PhD thesis (University of Canterbury, 1996).

[135] J.-P. R. Wells, M. Yamaga, T. P. J. Han, H. G. Gallagher, and M. Honda, "Polarized laser excitation, electron paramagnetic resonance, and crystal-field analyses of Sm^{3+}-doped $LiYF_4$", Phys. Rev. B **60**, 3849 (1999).

[136] M. Yamaga, M. Honda, J.-P. R. Wells, T. P. J. Han, and H. G. Gallagher, "An electron paramagnetic resonance study on Sm^{3+} and Yb^{3+} in KY_3F_{10} crystals", Journal of Physics: Condensed Matter **12**, 8727 (2000).

[137] R. M. Macfarlane and R. M. Shelby, "Photoionization hole burning and nonlinear Zeeman effect in CaF_2:Sm^{2+}", Opt. Lett. **9**, 533 (1984).

[138] Y. Ran, Y. Zhang, and A. Vishwanath, "One-dimensional topologically protected modes in topological insulators with lattice dislocations", Nature Physics **5**, 298 (2009).

[139] S. Wolgast, Y. S. Eo, Ç. Kurdak, D.-J. Kim, and Z. Fisk, *Conduction through subsurface cracks in bulk topological insulators*, 2015, arXiv:1506.08233.

[140] X. Zhang, N. P. Butch, P. Syers, S. Ziemak, R. L. Greene, and J. Paglione, "Hybridization, Inter-Ion Correlation, and Surface States in the Kondo Insulator SmB_6", Phys. Rev. X **3**, 011011 (2013).

[141] D. J. Kim, J. Xia, and Z. Fisk, "Topological surface state in the Kondo insulator samarium hexaboride", Nat. Materials **13**, 466 (2014).

[142] W. T. Fuhrman, J. Leiner, P. Nikolić, G. E. Granroth, M. B. Stone, M. D. Lumsden, L. DeBeer-Schmitt, P. A. Alekseev, J.-M. Mignot, S. M. Koohpayeh, P. Cottingham, W. A. Phelan, L. Schoop, T. M. McQueen, and C. Broholm, "Interaction Driven Subgap Spin Exciton in the Kondo Insulator SmB_6", Phys. Rev. Lett. **114**, 036401 (2015).

[143] Z. Yue, X. Wang, D. Wang, J. Wang, D. Culcer, and S. Dou, "Crossover of Magnetoresistance from Fourfold to Twofold Symmetry in SmB_6 Single Crystal, a Topological Kondo Insulator", Journal of the Physical Society of Japan **84**, 044717 (2015), eprint: http://dx.doi.org/10.7566/JPSJ.84.044717.

[144] J. Yong, Y. Jiang, X. Zhang, J. Shin, I. Takeuchi, and R. L. Greene, *Robust Surface States indicated by Magnetotransport in SmB_6 Thin Films*, 2015, arXiv:1502.00547 [cond-mat.str-el].

[145] N. Wakeham, Y. Q. Wang, Z. Fisk, F. Ronning, and J. D. Thompson, "Surface state reconstruction in ion-damaged SmB_6", Phys. Rev. B **91**, 085107 (2015).

[146] H. Hertz, "Ueber die Berührung fester elastischer Körper", Journal für die reine und angewandte Mathematik **92**, 156 (1882).

[147] S. Gabáni, E. Bauer, S. Berger, K. Flachbart, Y. Paderno, C. Paul, V. Pavlík, and N. Shitsevalova, "Pressure-induced Fermi-liquid behavior in the Kondo insulator SmB_6 : Possible transition through a quantum critical point", Phys. Rev. B **67**, 172406 (2003).

[148] J. Derr, G. Knebel, D. Braithwaite, B. Salce, J. Flouquet, K. Flachbart, S. Gabáni, and N. Shitsevalova, "From unconventional insulating behavior towards conventional magnetism in the intermediate-valence compound SmB_6", Phys. Rev. B **77**, 193107 (2008).

[149] J. C. Cooley, M. C. Aronson, A. Lacerda, Z. Fisk, P. C. Canfield, and R. P. Guertin, "High magnetic fields and the correlation gap in SmB_6", Phys. Rev. B **52**, 7322 (1995).

[150] *APS March Meeting 2014*, Vol. 59, 1, Abstract D43.00015, http://meetings.aps.org/link/BAPS.2014.MAR.D43.15, The American Physical Society (Denver, Colorado, Mar. 2014).

[151] B. S. Tan, Y.-T. Hsu, B. Zeng, M. C. Hatnean, N. Harrison, Z. Zhu, M. Hartstein, M. Kiourlappou, A. Srivastava, M. D. Johannes, T. P. Murphy, J.-H. Park, L. Balicas, G. G. Lonzarich, G. Balakrishnan, and S. E. Sebastian, "Unconventional Fermi surface in an insulating state", Science **349**, 287 (2015), eprint: `http://www.sciencemag.org/content/349/6245/287.full.pdf`.

[152] M. Takigawa, H. Yasuoka, Y. Kitaoka, T. Tanaka, H. Nozaki, and Y. Ishizawa, "NMR Study of a Valence Fluctuating Compound SmB_6", Journal of the Physical Society of Japan **50**, 2525 (1981), eprint: `http://dx.doi.org/10.1143/JPSJ.50.2525`.

[153] M. Bose, K. Roy, and A. Basu, "^{11}B NMR study of intermediate valent SmB_6", Journal of Physics C: Solid State Physics **13**, 3951 (1980).

[154] O. Peña, M. Lysak, D. E. MacLaughlin, and Z. Fisk, "Nuclear spin relaxation, hybridization, and low-temperature $4f$ spin fluctuations in intermediate-valent SmB_6", Solid State Communications **40**, 539 (1981).

[155] O. Peña, D. E. MacLaughlin, M. Lysak, and Z. Fisk, "NMR and spin/charge fluctuations in intermediate-valent SmB_6", Journal of Applied Physics **52**, 2152 (1981).

[156] M. Takigawa, H. Yasuoka, T. Tanaka, Y. Ishizawa, M. Kasaya, and T. Kasuya, "NMR study of mixed valent compounds SmB_6 with La and Yb substitution and CeB_6", Journal of Magnetism and Magnetic Materials **31–34, Part 1**, 391 (1983).

[157] T. Kasuya, M. Kasaya, K. Takegahara, T. Fujita, T. Goto, A. Tamaki, M. Takigawa, and H. Yasuoka, "Mechanisms for anomalous properties in SmB_6", Journal of Magnetism and Magnetic Materials **31–34, Part 1**, 447 (1983).

[158] T. Caldwell, A. P. Reyes, W. G. Moulton, P. L. Kuhns, M. J. R. Hoch, P. Schlottmann, and Z. Fisk, "High-field suppression of in-gap states in the Kondo insulator SmB_6", Phys. Rev. B **75**, 075106 (2007).

[159] G. Pristáš, T. Mito, T. Kohara, S. Gabáni, M. Reiffers, K. Flachbart, N. Takeshita, and N. Shitsevalova, "Pressure-Induced Suppression of Energy Gap in the Kondo Insulator SmB_6 Studied by ^{11}B-NMR", Journal of the Physical Society of Japan **80**, SA078 (2011), eprint: http://dx.doi.org/10.1143/JPSJS.80SA.SA078.

[160] K. Nishiyama, T. Mito, G. Pristáš, Y. Hara, T. Koyama, K. Ueda, T. Kohara, Y. Akahama, S. Gabáni, M. Reiffers, K. Flachbart, H. Fukazawa, Y. Kohori, N. Takeshita, and N. Shitsevalova, "Pressure-Induced Localization of $4f$ Electrons in the Intermediate Valence Compound SmB_6", Journal of the Physical Society of Japan **82**, 123707 (2013), eprint: http://dx.doi.org/10.7566/JPSJ.82.123707.

[161] T. Wu, A. Reyes, P. Kuhns, S. Yuan, and C. Coffman, *NMR Study on La-doped SmB_6 Single Crystals*, Research Report (National High Magnetic Field Laboratory, 2013).

[162] K. Kojima, M. Kasaya, and Y. Koi, "Electron Paramagnetic Resonance Study of Gd^{3+} and Eu^{2+} in the Mixed Valence Compound SmB_6", Journal of the Physical Society of Japan **44**, 1124 (1978).

[163] T. S. Altshuler, V. N. Mironov, and M. M. Zaripov, "EPR on the Eu^{2+} ions in SmB_6", Journal of Physics C: Solid State Physics **15**, 3785 (1982).

[164] H. Sturm, B. Elschner, and K. H. Höck, "ESR Spectra of Er^{3+} in SmB_6 Single Crystals: Dynamic Jahn-Teller Effect in a Mixed-Valence Compound", Phys. Rev. Lett. **54**, 1291 (1985).

[165] G. Wiese, H. Schäffer, and B. Elschner, "Possible $4f^7 5d^1$ Ground State of Gd Impurities in the Mixed-Valence Compound SmB_6, Observed with Electron Spin Resonance", EPL (Europhysics Letters) **11**, 791 (1990).

[166] B. Amsler, Z. Fisk, J. L. Sarrao, S. von Molnar, M. W. Meisel, and F. Sharifi, "Electron-tunneling studies of the hexaboride materials SmB_6, EuB_6, CeB_6, and SrB_6", Phys. Rev. B **57**, 8747 (1998).

[167] K. Flachbart, K. Gloos, E. Konovalova, Y. Paderno, M. Reiffers, P. Samuely, and P. Švec, "Energy gap of intermediate-valent SmB_6 studied by point-contact spectroscopy", Phys. Rev. B **64**, 085104 (2001).

[168] M. M. Yee, Y. He, A. Soumyanarayanan, D.-J. Kim, Z. Fisk, and J. E. Hoffman, *Imaging the Kondo Insulating Gap on SmB_6*, Aug. 2013, arXiv:1308.1085.

[169] S. Rößler, T.-H. Jang, D.-J. Kim, L. H. Tjeng, Z. Fisk, F. Steglich, and S. Wirth, "Hybridization gap and Fano resonance in SmB_6", Proceedings of the National Academy of Sciences **111**, 4798 (2014), eprint: http://www.pnas.org/content/111/13/4798.full.pdf.

[170] J. N. Chazalviel, M. Campagna, G. K. Wertheim, P. H. Schmidt, and Y. Yafet, "Electronic Structure and $4f$-Hole Lifetime in Rare-Earth Borides", Phys. Rev. Lett. **37**, 919 (1976).

[171] J. N. Chazalviel, M. Campagna, G. K. Wertheim, and P. H. Schmidt, "Study of valence mixing in SmB_6 by x-ray photoelectron spectroscopy", Phys. Rev. B **14**, 4586 (1976).

[172] J. W. Allen, L. I. Johansson, I. Lindau, and S. B. Hagstrom, "Surface mixed valence in Sm and SmB_6", Phys. Rev. B **21**, 1335 (1980).

[173] P. Hlawenka, K. Siemensmeyer, E. Weschke, A. Varykhalov, J. Sánchez-Barriga, N. Y. Shitsevalova, A. V. Dukhnenko, V. B. Filipov, S. Gabáni, K. Flachbart, O. Rader, and E. D. L. Rienks, *Samarium hexaboride: A trivial surface conductor*, 2015, arXiv:1502.01542 [cond-mat.str-el].

[174] M. Mizumaki, S. Tsutsui, and F. Iga, "Temperature dependence of Sm valence in SmB_6 studied by X-ray absorption spectroscopy", Journal of Physics: Conference Series **176**, 012034 (2009).

[175] *APS March Meeting 2015*, Vol. 60, 1, Abstract J10.00006, http://meetings.aps.org/Meeting/MAR15/Session/J10.6, The American Physical Society (San Antonio, Texas, Mar. 2015).

[176] J. Beille, M. B. Maple, J. Wittig, Z. Fisk, and L. E. DeLong, "Suppression of the energy gap in SmB_6 under pressure", Phys. Rev. B **28**, 7397 (1983).

[177] A. Barla, J. Derr, J. P. Sanchez, B. Salce, G. Lapertot, B. P. Doyle, R. Rüffer, R. Lengsdorf, M. M. Abd-Elmeguid, and J. Flouquet, "High-Pressure Ground State of SmB_6: Electronic Conduction and Long Range Magnetic Order", Phys. Rev. Lett. **94**, 166401 (2005).

[178] M. Aono, R. Nishitani, T. Tanaka, E. Bannai, and S. Kawai, "Azimuthal anisotropy in low-energy ion scattering from SmB_6 (001)", Solid State Commun. **28**, 409 (1978).

[179] *APS March Meeting 2014*, Vol. 59, 1, Abstract B42.00015, http://meetings.aps.org/link/BAPS.2014.MAR.B42.15, The American Physical Society (Denver, Colorado, Mar. 2014).

[180] R. H. Silsbee, "Spin-orbit induced coupling of charge current and spin polarization", Journal of Physics: Condensed Matter **16**, R179 (2004).

[181] D. K. Cheng, *Field and Wave Electromagnetics* (Addison-Wesley Publishing Company, Inc., Reading, MA, 1983), p. 392.